Physical Volcanology of Obsidian Dome, California: A Complex Record of Emplacement of a Youthful Lava Dome

By

Cole G. Kingsbury

A thesis submitted to the Faculty of Graduate and Postdoctoral Studies

in partial fulfillment of the requirements

for the degree of Masters of Science in Earth Science

Ottawa-Carleton Geoscience Centre

and

University of Ottawa

Abstract

Obsidian Dome is a 550-650 year old, 1.5 by 1.8 km extrusion of high silica rhyolite situated along the Inyo Craters in eastern California. Field, and observations of drill core, reveals discrete metre-scale thick zones of rhyolitic glass exposed along the margin of Obsidian Dome as well as within its interior. Millimetre-scale flow-banded obsidian, pumice and rhyolite range from planar to chaotically folded, the latter a product of ductile, compressive deformation. Fractures, some of which display en-echelon splitting patterns are a result of brittle failure. Taken together, these features along with others, result from flow during lava dome growth and suggest complex emplacement patterns signified by vesiculation, crystallization and repeated brittle-ductile deformation, owing to episodic crossing of the glass transition. Evidence further shows that gas loss from the system occurred due to explosions, pumice formation and also brecciation of the melt as it episodically crossed the glass transition. Loss of gas by these mechanisms along with the inherent high viscosity of rhyolite melt explains the large amount of glass found on and within Obsidian Dome and other similar rhyolite extrusions in comparison to less silica-rich systems.

Résumé

Obsidian Dome, situé le long des cratères d'Inyo en Californie, consiste en une extrusion de rhyolite riche en silice formée il y a 550-650 ans et mesurant 1,5 km par 1,8 km. Des observations de terrain et de forage révèlent l'existence de zones épaisses bien définies de verre rhyolitique à l'échelle métrique, lesquelles sont exposées en marge ainsi qu'à l'intérieur d'Obsidian Dome. Les obsidiennes, pumices et rhyolites rubanées (*flow-banded*) à l'échelle millimétrique peuvent être planaires ou montrer des plis chaotiques, ceux-ci résultant de déformation ductile compressive. Les fractures, dont certaines montrent des patrons de séparation en échelon, sont le résultat de déformation cassante. L'ensemble de ces caractéristiques ainsi que d'autres résultent d'écoulement lors de la croissance d'un dôme de lave et suggèrent des patrons d'emplacement complexes, comme le témoignent la vésiculation, la cristallisation et la répétition de déformation cassante-ductile en raison du franchissement épisodique de la transition du verre. Des évidences indiquent de surcroît que les gaz se sont échappés du système à cause d'explosions, de formation de pumice et aussi de bréchification du matériel en fusion lorsque celui-ci franchissait épisodiquement la transition du verre. L'échappement des gaz par ces mécanismes de même que la viscosité élevée inhérente à la lave rhyolitique expliquent la grande quantité de verre retrouvée à la surface et à l'intérieur d'Obsidian Dome et d'autres extrusions rhyolitiques similaires comparé à des systèmes moins riches en silice.

Dedication

I dedicate this work to my two lovely parental units, Steve and Diane. Because of their tremendous and unwavering love, support, and dedication coupled with the many sacrifices they have made since they watched *The Breakfast Club* on March 17th, 1985 always has gone above and beyond their call of duty in giving me every opportunity to flourish and – as a result – be who I am today.

I also dedicate this thesis to my grandparents Clement, Bertha, Florence and Maurice. The four of them did a marvelous job raising two fine parental units and all of whom must be smiling right about now.

Dear Mom and Dad:

Thank you for being there and supporting me as I work towards my life goals from a very early age. I will confess however, I was a tad on the premature side when I took that first "driving lesson" on Karyl Drive. Perhaps the idea of driving to an outcrop and starting a rock collection that early on was a bit much. ☺

Love and prosper!

~Cole K.

Acknowledgements

Following the traditions of post-graduate studies, this thesis administratively speaking, is a solitary affair. In reality however, this work is the product of many people who have graciously supported my research from conception to finality. First and foremost, I will forever hold a debt of gratitude to my colleague, mentor and advisor Prof. Anthony Fowler who, despite entering retirement, graciously accepted me as one of his final graduate students and subsequently supported my research every step of the way.

Laboratory support was graciously provided by many dedicated and hardworking people. Peter Jones at Carleton University helped me in obtaining geochemical data from the electron microprobe while introducing to me the internal mechanics of microprobing. Analysis of powder X-Ray Diffraction data was greatly improved though discussions on numerous occasions with Tara Kell, here at the University of Ottawa. I wish to also pay thanks to David Langton at the University of Utah in Salt Lake City who provided me access and great hospitality during my trip to SLC to observe and log cores taken during the 1984 Continental Scientific Drilling Program.

Field support during my field campaign was greatly enhanced by the assistance of and discussions with fellow graduate student Chris Clarke and honours student Danielle Denis.

Table of Contents

List of Figures

Note: If a figure cuts across two pages, the first page that it appears is the one listed here.

Chapter 1: Introduction to the Long Valley Region

A. Geographic and Tectonic Setting

In a regional context, Obsidian Dome, California is centrally situated within the Long Valley region, which is located ~ 220 km south-southeast of Reno Nevada, ~250 km southeast of Sacramento California, ~130 km NW of Fresno, California and ~370 km northwest of Las Vegas, Nevada, (Figure 1). For the purpose of this thesis , the "Long Valley Region" will collectively refer to the Long Valley Caldera and the associated Resurgent Dome and Moat rhyolites, Glass Mountain, Mono Craters, Inyo Craters and Mammoth Mountain, (all to be discussed herein). Obsidian Dome itself is located about 5 km southeast of June Lake California, north of Owens Valley , and is immediately east of the eastern front of the Sierra Nevada mountain range.

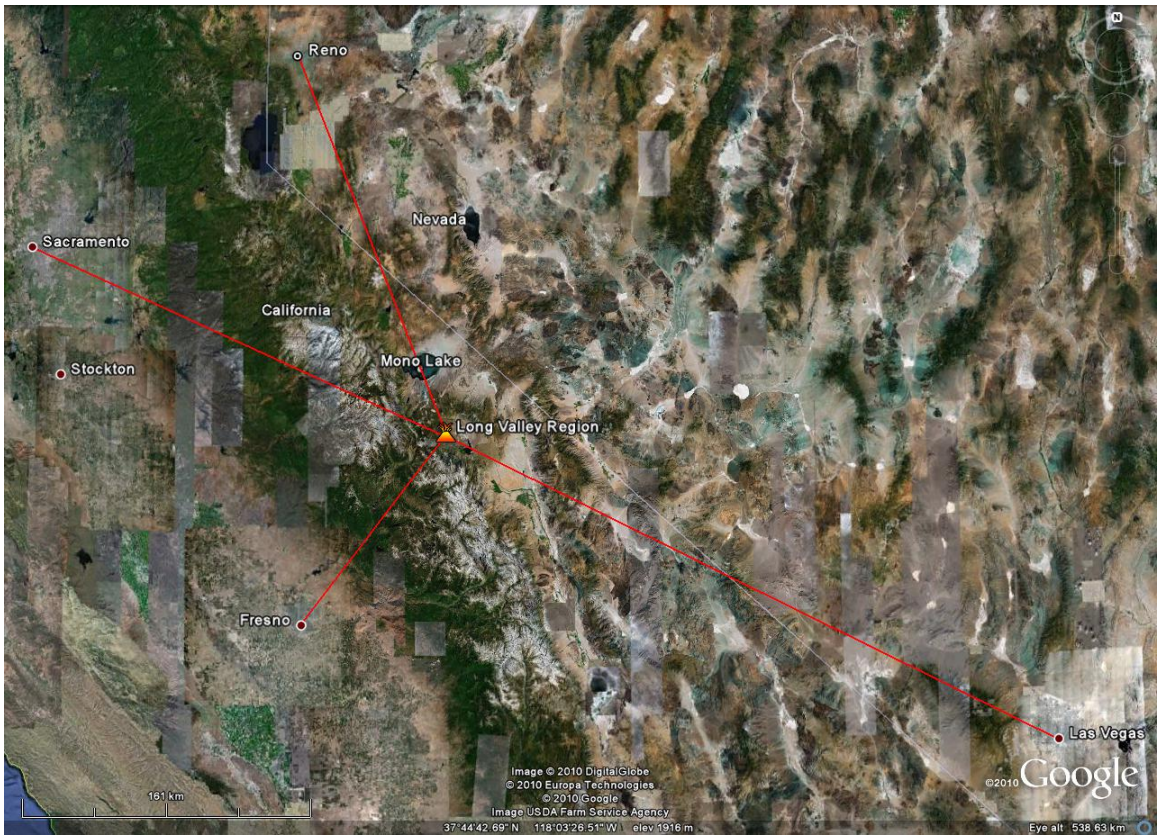

Figure 1: Regional map showing the location of Obsidian Dome with respect to significant regional population centres. Red lines indicate direction and relative distance from the Long Valley Region to cities mentioned in the above paragraph. Image from Google Earth.

Volcanism in the Long Valley Region is principally controlled by a trans-tensional tectonic regime dominated by significant right-lateral oblique faults having a normal vertical component, (Bursik, 2009). Bailey (1989) has mapped the Hilton Creek Fault (Fig. 2) as a north-northwest trending, down-to-the-east normal fault, located south of, and impinging into the southeast margin of the Long Valley Caldera in the vicinity of Tobacco Flat. The Hilton Creek Fault, and to a lesser extent the Casa Diablo Mountain Fault, a separate fault that is parallel to the former, collectively account for much of the strain that has built up in the southern Long Valley region (Bursik, 2009). On the north side of the Long Valley Caldera,

where Obsidian Dome lies, the tectonic regime is similar to that of the south side but more complex as the stress is taken up by the north-northeast trending Hartley Springs, Sagehen Peak and the Silver lake Faults, Figure 2 (Bursik, 2009). This ensemble of faults, and subsidiary faults, have been interpreted by Bursik, (2009) as forming a pull-apart basin within which magma of the ~760 ka Bishop Tuff eruption evolved.

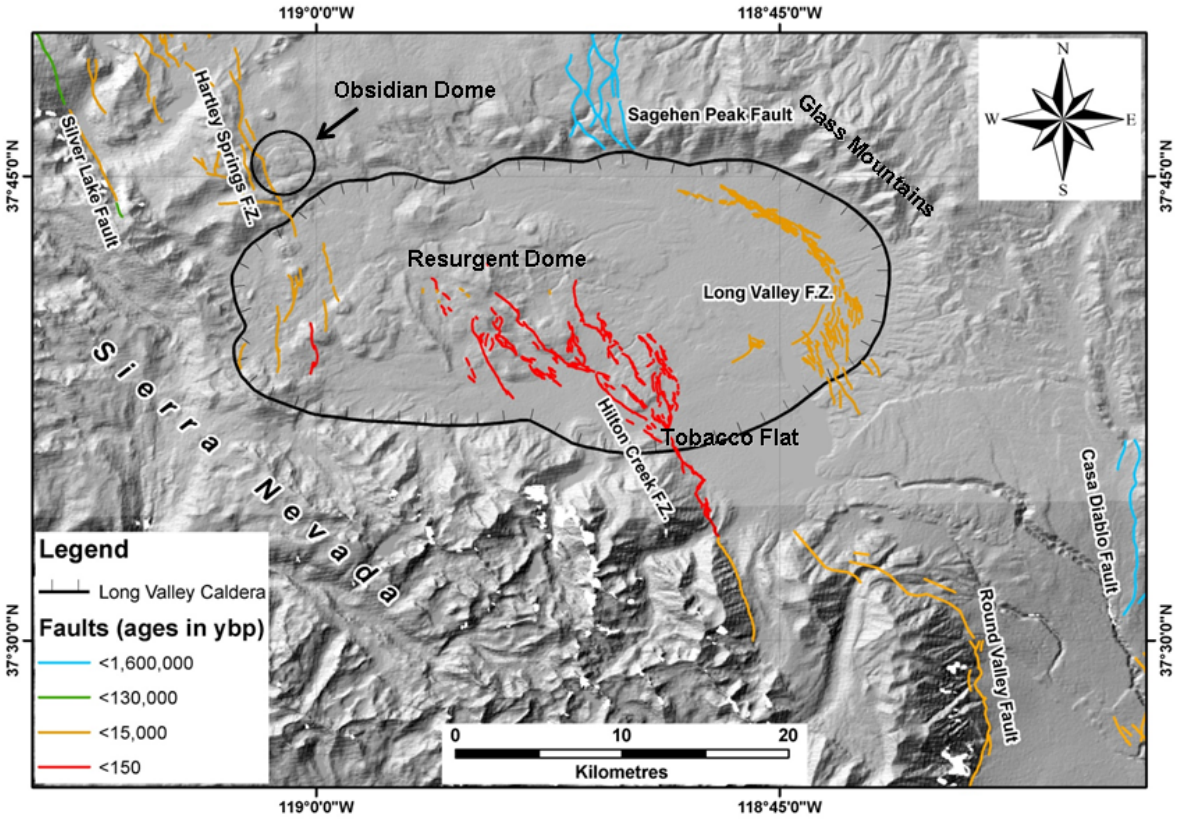

Figure 2: Simplified structural map of the Long Valley Region showing major faults and the Long Valley Caldera. Hatchers of the Long Valley Caldera are on the down-thrown block. Fault data are from the USGS Quaternary Faults and Folds Database, (2006) overlain onto a hillshade topographic image derived from a Digital Elevation Model of the Shuttle Radar Topographic Mission (SRTM) by the author. Obsidian Dome, northwest of the Long Valley Caldera, is circled.

B. Pre-Long Valley Volcanism

Volcanic activity prior to the Bishop Tuff eruption was characterized by a series of relatively small Pliocene basalt and dacite eruptive sequences which peaked in intensity between 3.8 and 2.5 Ma (Bailey, 2004). The loci of the alternating basalt and dacite sequence of eruptive activity were mainly around the northwest periphery of the future Long Valley Caldera. Near the eventual Long Valley Caldera, the composition of the pre-caldera eruptive units was a mélange of basalt and dacite, whereas further from the caldera site, dacite is conspicuously absent. The vents from which the subsequent pre-Bishop Tuff extrusions of dacite and high silica rhyolitic volcanic rock only occur in the vicinity of the future Long Valley Caldera (Glass Mountains), and Hildreth, (2004) attributes this event to be co-incident with a significant west-to-the-north offset of the Sierra Mountain rangefront, and thus promoted the development of the Bishop Tuff magma chamber.

The Bishop Tuff magma chamber, from which the 760 ka Bishop Tuff super-eruption was sourced, first fed a suite of chemically diverse rhyolite domes and flows (Halliday et al, 1989; Bindeman and Valley, 2002). The Glass Mountains (NE margin of the Long Valley Caldera, Figs. 2 & 3) comprise this suite of highly evolved domes and flows ranging in age from ~2.1 Ma to 0.79 Ma (Bindeman and Valley, 2002). Lavas of the older domes (2.1-1.2 Ma) are chemically and isotopically distinct from the later phase of erupted products (1.2-0.79 Ma; Bindeman and Valley, 2002). Major, minor and trace element analysis, coupled with isotopic data show that over time Glass Mountain rhyolites became increasingly similar to the eventual high-sillica rhyolites that erupted during the 760 ka Bishop Tuff super-eruption.

C. The 760 ka Bishop Tuff Super-Eruption

Volcanism in the Long Valley Region culminated at ~760 ka with the cataclysmic, caldera forming eruption, from which the Bishop Tuff issued. A model for the progression of this eruption is put forth by Hildreth and Mahood (1986), who postulated that the eruption commenced as a singular plinian eruption cloud sourced in the vicinity of the Hilton Creek Fault (Fig. 2) which, over time evolved into a multiple-vent, ignimbrite-producing, compositionally-zoned super eruption around a system of ring-fractures. The volumetric magnitude of magma evacuation from the chamber, coupled with a nearly continuous pulse of volatile-charged ash flow spanned up to an estimated 6 days in duration without any apparent long term pause, and promoted the subsequent collapse of the chamber roof (Wilson and Hildreth, 1997; Hildreth, 2004). The end result of this great eruption, was the formation of the ~15 x 20 km Long Valley Caldera, (Figs. 2 & 3).

D. Caldera-Related, Post-Bishop Tuff Eruptive History

From the conclusion of the ~760 ka Bishop Tuff super-eruption to approximately 100 ka, eruptive activity became predominately effusive with several flows and domes of post-caldera rhyolite. Based upon their chemical composition, Hildreth, (2004) attributes these as being extrusions sourced from a chemically reorganized Long Valley magma chamber. Following the convention set forth by Bailey (1989), post-caldera rhyolites are grouped into two domains that are spatially and temporally distinct: Early Rhyolites, and the later so-called Moat Rhyolites. Early Rhyolite constructed the central resurgent dome (Fig. 2 and 3), which is sparsely porphyritic (<3% phenocrysts) and erupted during the 100 ka interval following the Bishop Tuff super-eruption (760-652 ka, Mankinen et al., 1986; Bailey 1989). Moat Rhyolite erupted from three spatially-distinct clusters of vents north, southeast

and west of the resurgent dome at ~500, 300 and 100 ka, respectively (Bailey, 1989). In common with the Early Rhyolite the earliest Moat Rhyolites are distinctively phenocryst-poor, (<3% phenocrysts) whereas the later western moat rhyolite complex is almost exclusively phenocryst-rich (20-30% phenocryst content; Hildreth, 2004). The increase in phenocrysts over time, coupled with a marked decline of eruption rate from ~1 km^3/ka during the Early Rhyolite episode to as little as 0.01 km^3/ka after the Early Rhyolite time, as well as thermal data from the Long Valley Exploratory Well, (Sackett, et al., 1999) suggest that the magma chamber from which The Glass Mountains, Bishop Tuff, Early Rhyolite and Moat Rhyolites were derived has crystallized to an extent that it renders the Long Valley Caldera magmatic system essentially extinct (Hildreth, 2004).

E: Mammoth Mountain Dome Complex

Mammoth Mountain is an array of coalescing silicic lava domes which are clustered in the southwest margin of the Long Valley Caldera (Fig. 3). Despite its relatively imposing topographic prominence east of the Sierra Nevada crest, only ~4 km^3 of silicic lavas constructed the edifice of Mammoth Mountian, (Hildreth, 2004). Hildreth, (2004) attributes this mainly due to the locus of eruptive activity occurring on pre-existing high topography, just outboard of the down-dropped block of the Long Valley Caldera. Chemically, the lavas of Mammoth Mountain are trachydacites, dacites and alkalic rhyodacites (Bailey, 2004; Hildreth, 2004). The Mammoth Mountian array of vents are spatially and temporally distinct from both the moat and resurgent dome rhyolites and the subsequent Mono-Inyo chain (discussed next section), having erupted during the interval 111 – 57 ka (Mankinen, et al., 1986; Hildreth, 2004).

F. The Mono-Inyo Chain

The Mono-Inyo chain of silicic lava domes which Obsidian Dome is a member, are situated northwest of, and lie principally outside the topographic margin of the Long Valley caldera (Figure 3). Hildreth (2004) subdivides this chain into two sub-chains: the curvy-linear Mono Chain comprising the north part, and the linear Inyo chain to the south. While Hildreth identifies Wilson Butte (triangle WB in Figure 3) as being the northern limit of the Inyo chain, Hildreth further advocates that the entire Mono-Inyo chain be treated as a single, coherent system due to the contiguity of the Holocene eruptive centres.

A glaringly obvious feature of the Inyo chain is the northwest trending single-file alignment of vents. The orientation of this chain is parallel to the nearby Hartley Springs Fault (HSF on Figure 3). Bursik and others (2003) hypothesize that the dike which fed Obsidian, Glass Creek and Deadman Creek Domes encountered the Hartley Springs Fault as it propagated towards the surface, caused fault displacement which, in turn reduced confining pressure that allowed the dike to reach the surface locally. Though the dominant orientation of the Inyo chain is north-trending, Fink (1985) has mapped a series of north-northeast-trending grabens on Obsidian, Glass Creek and Deadman Creek domes (Figure 4). From these structural features, Fink (1985) concludes that the dominantly northwest-trending dike splintered and subsequently rotated into a series of northeast-trending, en echelon dike segments as the maximum principal stress direction shifted from a northwest orientation at depth to a northeast orientation close to the surface.

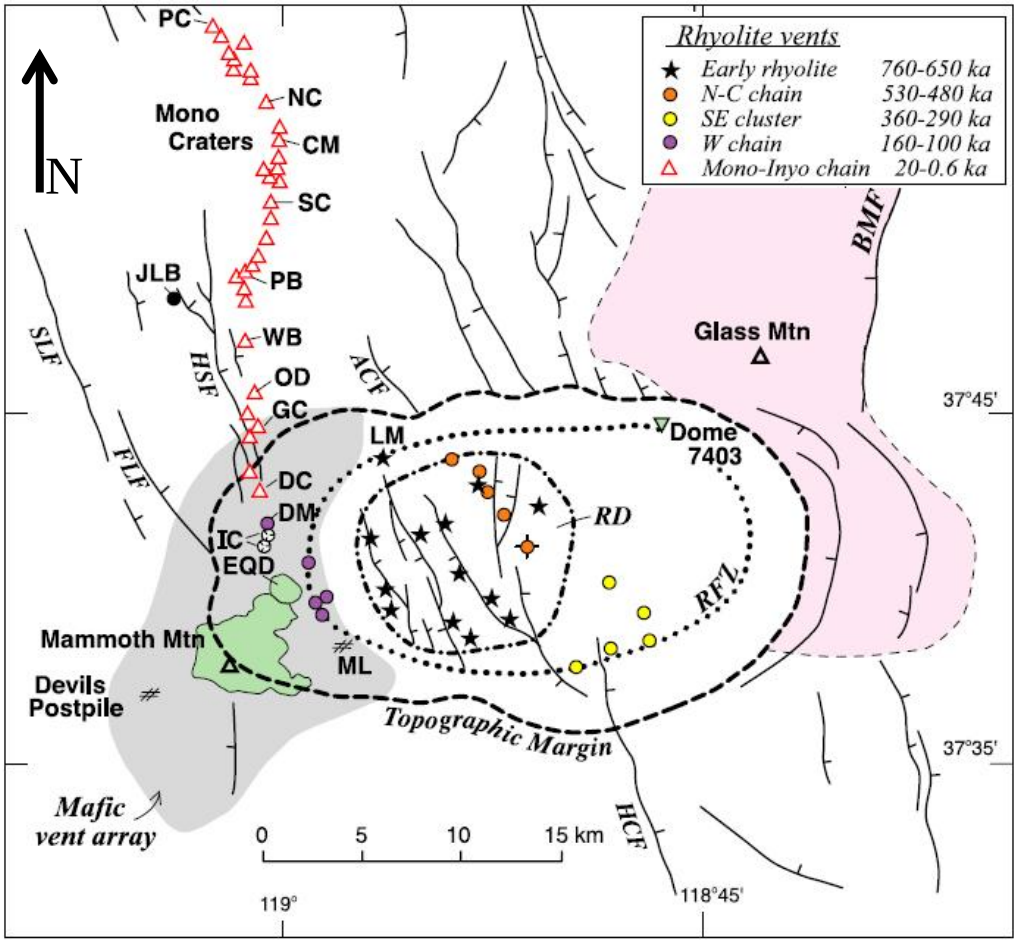

Figure 3: Structural and vent distribution map showing regionally important faults and alignments of select rhyolitic vent arrays. The Mono-Inyo chain are represented here as red triangles extending from the northwest topographic margin of the Long Valley Caldera for about 25 km north thereof. Key to vent names in this array: PC = Panum Crater, NC= North Coulee, CM = Crater Mountian, SC=South Coulee, PB=Punch Bowl, WB=Wilson Butte, OD=Obsidian Dome, GC=Glass Creek Dome, DC=Deadman Creek Dome, RD = resurgent dome, (dash-dot line). Key to fault zones: RFZ = Ring Fracture Zone, HCF = Hilton Creek fault, BMF = Black Mountain fault, ACF = Ayers Canyon fault, FLF = Fern Lake fault, SLF = Silver Lake fault. Around Mammoth Mountain: IC = Inyo Craters, EQD = Earthquake Dome and ML = Town of Mammoth Lakes. Modified from Hildreth (2004).

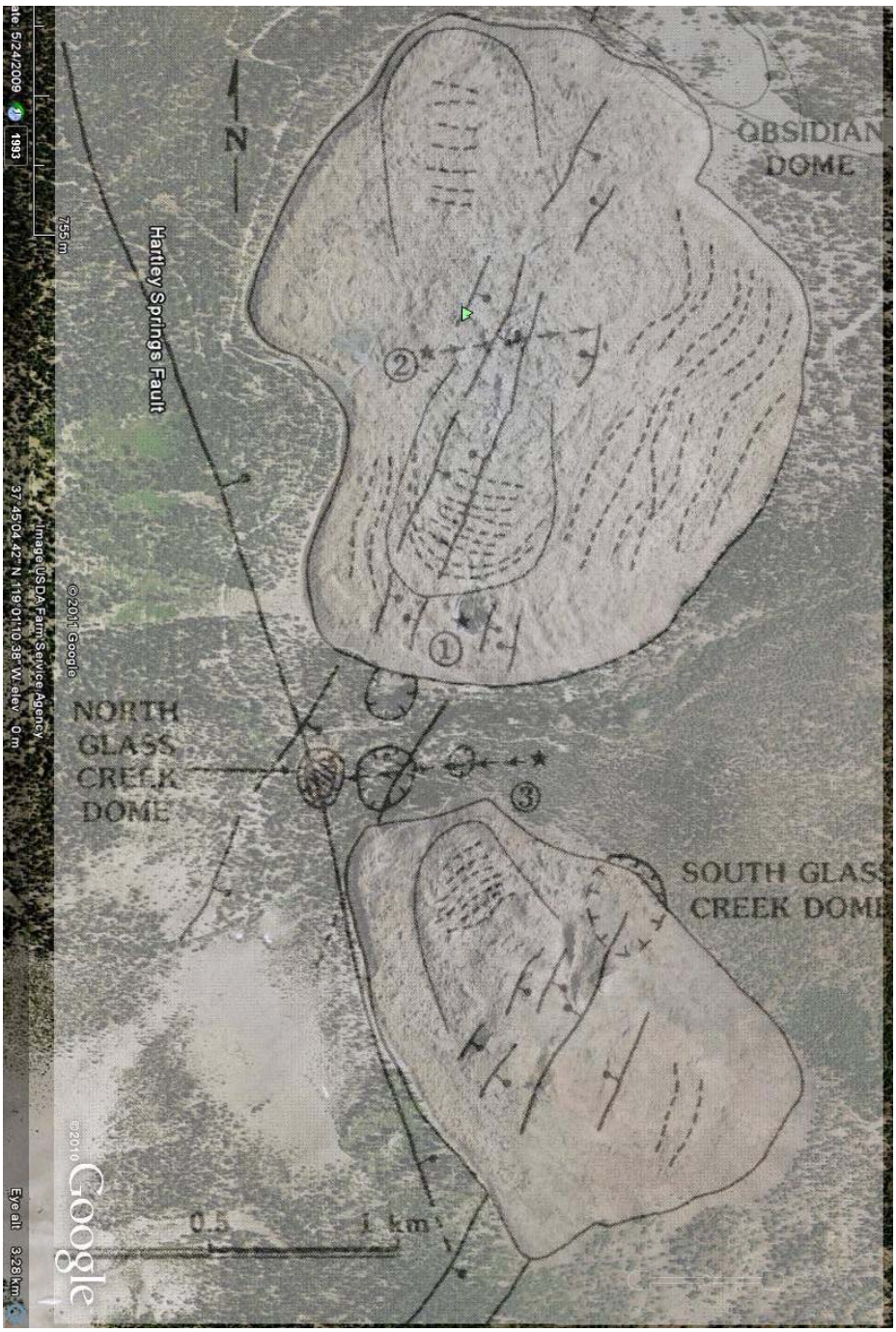

Figure 4: Structural map of the Obsidian and Glass Creek domes of Fink (1985) superimposed on Google Earth Imagery. Solid lines are faults with ball pointing towards the down-dropped block; hachures mark the location of explosion pits with tick-marks pointing towards the centre of each pit. Dashed-lines on the domes denote compression ridges while stars mark the three surface locations of Continental Scientific Drilling Program operations (Eichelberger et al., 1985). The north-northwest trending Hartley Springs Fault parallels the orientation of the Inyo chain to the west, while a series of north-northeast-trending grabens bisect the inferred vent areas of each dome.

G. Obsidian Dome

Obsidian Dome is the northern-most of the three high-silica rhyolite domes that together, comprise the Inyo Domes chain (Fig. 3). With the exception of a subdued topographic high in the centre of Obsidian Dome, likely marking the vent region, the ambient morphology of this 1.8 km x 1.5 km extrusion consists of a relatively flat carapace bounded by sharp and steep (40º – 65º) slope margins that are 10s of metres in height, (Figs. 5, 11 and 12A). From a distance of a few hundred metres it appears to be composed of black lustrous glass within variably undulating bands or zones zones of dull tan, light grey and light orange coloured rocks. It is surrounded by ubiquitous talus slopes composed of angular blocks ranging in size from a few decimeters to a few meters. The dome is easily accessed from U.S. Highway 395 by a forest service road and a trail that circumscribes it.

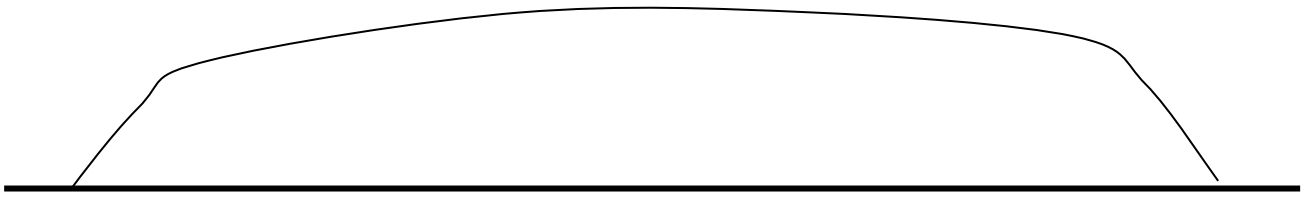

Figure 5: Cartoon topographic profile through a typical section of Obsidian Dome.

H. Objectives:

The overall objective of this thesis is to investigate the extrusion history of Obsidian Dome in light of field, laboratory and theoretical work that has been published (e.g. Dingwell and Webb, 1989; Tuffen et al., 2005) since models relating to the emplacement of Obsidian Dome and other high silica rhyolite domes were proposed (e.g.: Taylor et al., 1983; Eichelberger et al., 1986; Fink et al., 1992).

Domes composed of volcanic glass are somewhat enigmatic because volumes of glass on the order of 10s of metres in thickness are not expected to exist naturally. With the exception of material at the lava-air interface, lavas cool by thermal conduction – a relatively slow process – whereas glass is typically the product of quenching. The principal objective of my thesis is to address this problem and, more specifically to address models that have been proposed for the formation of glass on Obsidian Dome. Two models have been invoked to address the large volumes of glass found at Obsidian Dome and similar structures throughout the western United States: the "permeable foam" model of Eichelberger and others (1986) and "volatile stratification" invoked by Fink and others (1992). I describe both these models in Chapter 2 and discuss the implications of each in Chapter 5 after I present the data.

In addition, lithophysal and non-lythophysal spherulites (to which I define in Chapter 2) are widely believed to be devitrification structures. Indeed, Swanson and his colleagues (1989) termed them so in their work on Obsidian Dome. Previous work has shown that not all spherulites are due to devitrification, (e.g. Lofgren, 1971a; Lofgren, 1971b). In addition, lithophysal spherulites clearly are related to gas exsolution, which in itself is directly related to the mode of emplacement of rhyolite domes, including Obsidian Dome. Accordingly, another objective of this thesis is to document the timing of formation ofboth lithophysal and non-lithophysal spherulites.

Chapter 2: Physical Properties of Rhyolite Melts

A. Introduction:

Obsidian Dome displays a wide array of structural and textural patterns which signify a complex emplacement history. Many of the physical features observed on Obsidian Dome are governed by the viscosity and rheological properties of highly polymerized silicate melt. Phenocrysts, vesicles (indicating the former presence of magmatic volatiles) and to a lesser extent spherulites & lythophysae are common phases observed on Obsidian Dome and each component likely had a distinct effect on the rheology of the melt during the period of ascent and emplacement. Accordingly melt dynamics are reviewed below.

B. Polymer Model of silicate melt viscosity

With the exception of carbonatite melt, nearly all known volcanic eruptions issued lava that can be effectively modeled based on the silica $[SiO_4]^{-4}$ tetrahedron. Commonly each silica tetrahedron may connect to other tetrahedra at oxygen sites, thereby forming 3D Si-O-Si-O-polymerized networks (Mysen, 1983; Winter, 2001). In light of this arrangement, O is shared between $[SiO_4]^{-4}$ tetrahedra and can therefore be called "bridging oxygen." To express the degree to which a melt is polymerized, the formula

$$D_{poly} = \frac{NBO}{T}, \qquad (1)$$

may be used where NBO is the number of non-bridging oxygen and T is the number of tetrahedrally-coordinated cations (e.g. Mysen 1983). The result in solving for equation 1 is

that, if we overlook the divide-by-zero issue, 4 represents isolated, non polymerized silica tetrahedra while 0 represents complete framework polymerization.

Depending on multiple factors including temperature, tectonic setting, crustal assimilation and fractional crystallization, the abundance of silica varies widely and that variation has important implications for the style of eruption. High silica rhyolites including those of Obsidian Dome are obviously silica rich and consequently highly polymerized—having large 3D -Si-O-Si-O chains and Na_2O—Al_2O_3—SiO_2 linked networks. Such chain-like structural arrangements impede the ability of high silica lavas to flow freely and thus they flow like a sticky paste and, as a consenquence rarely extendmore than a few km from their source vents. In contrast, low-silica concentration lavas such as basalt contain short –Si-O-Si-O chains and thus have low viscosity and unlike their high-silica cousins are able to flow startlingly long distances from their sources (e.g. the Columbia River Basalts flowed 100s of km from their source area).

C. Network Modifiers

All known coherent eruptive products worldwide, including those of the Obsidian Dome flow, contain species which variably perturb the rheological properties from an “ideal” homogeneous silicate melt. Some phases work to bond silicate chains together (network formers) and thus increase the viscosity of silicate melt while other phases de-polymerize the system (network modifiers) causing melt viscosity to decrease. The different phases and their effects to overall melt viscosity are discussed below.

D. Volatiles

An ascending batch of magma commonly contains species of dissolved gasses (termed "volatiles"), the amount of which varies with depth (i.e. pressure). The concentration of volatiles in a rising batch of magma, along with other factors such as viscosity, places a powerful constraint on the style of eruption, and thus has important societal implications with respect to geological hazards. In light of the hazards involving explosive (volatile-charged) high-silica lavas, numerous studies have been undertaken to ascertain how volatiles behave, particularly water, as it has a profound effect on the viscosity of granitic magma and consequently rheological properties (e.g. Hess and Dingwell, 1996; Dingwell et al, 1998).

The extensive network of silicate chains that dominate high-silica melts may be broken by the addition of dissolved water. As a result, the viscosity of the newly hydrated batch of magma decreases in comparison to dry magma of the same temperature, pressure and composition. The mechanism attributed to this process is that ^{+}H reacts with and breaks the bridging oxygen bond of the highly polymerized 3-dimentional Al_2O_3—SiO_2 network and converts it into less polymerized chains (Mysen et al, 1980).

Hess and Dingwell (1996) mathematically modeled experimental data to arrive at the relationship between viscosity, water concentration and temperature of metaluminous leucogranite melt

$$\log \eta = \frac{\left[-3.545 + 0.833\ln(w)\right] + \left[9601 - 2368\ln(w)\right]}{\left\{T - \left[195.7 + 32.25\ln(w)\right]\right\}} \qquad (2)$$

where η is the viscosity of the melt in Pa-s, w is the wt% concentration of water and T is the temperature in Kelvin. In promulgating this model, Hess and Dingwell assume that the melt behaves as a non-Arrhenian fluid (1996).

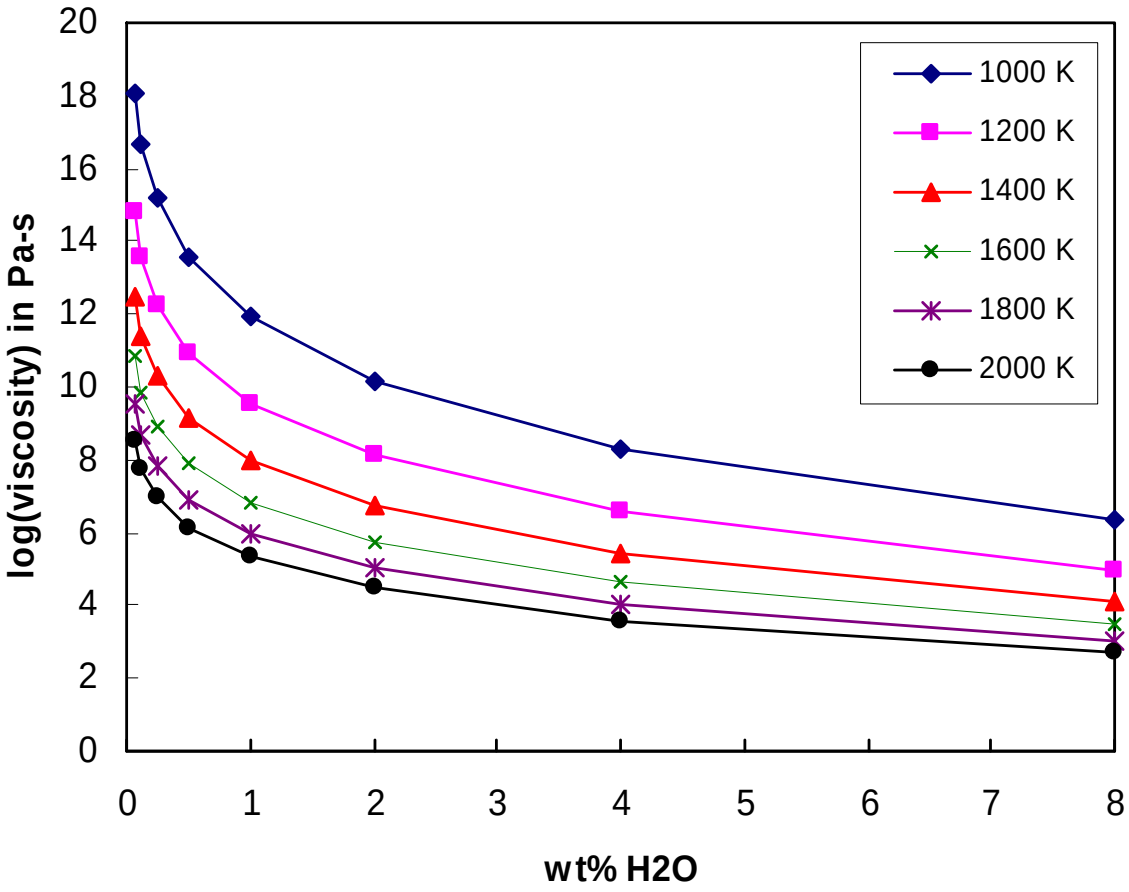

Figure 6: Plot showing the relationships between viscosity and water for rhyolite melts. Plot is based on solving for equation 2 for various temperatures (Hess and Dingwell, 1996). It should be noted that the shape of the curves using Eq. 2 are in broad agreement with those of the original model, however a mistake exists in the original publication. There is a consistent 2 to 3 log unit negative variance compared with the data reported by Hess and Dingwell (1996) curves for water contents less than ~4% when compared to my calculation. Nonetheless, the importance of the graph remains the fact that the viscosity of melt decreases significantly with water content.

Results based on this modeled relationship are plotted in Figure 6 and show that the change of the viscosity with the addition of even a trace amount of water (~<1 wt%) for metaluminous granitic melts is quite profound. This is in stark contrast to the addition of water in basaltic melts or previously hydrated rhyolite melts beyond 1 wt% H_2O because they are already de-polymerized. For example, at 1000 K, the viscosity difference between 0.0625 wt% and 1 wt% H_2O is approximately six log units downward, whereas the difference between 1 and 2 wt% H_2O is only two log steps downward.

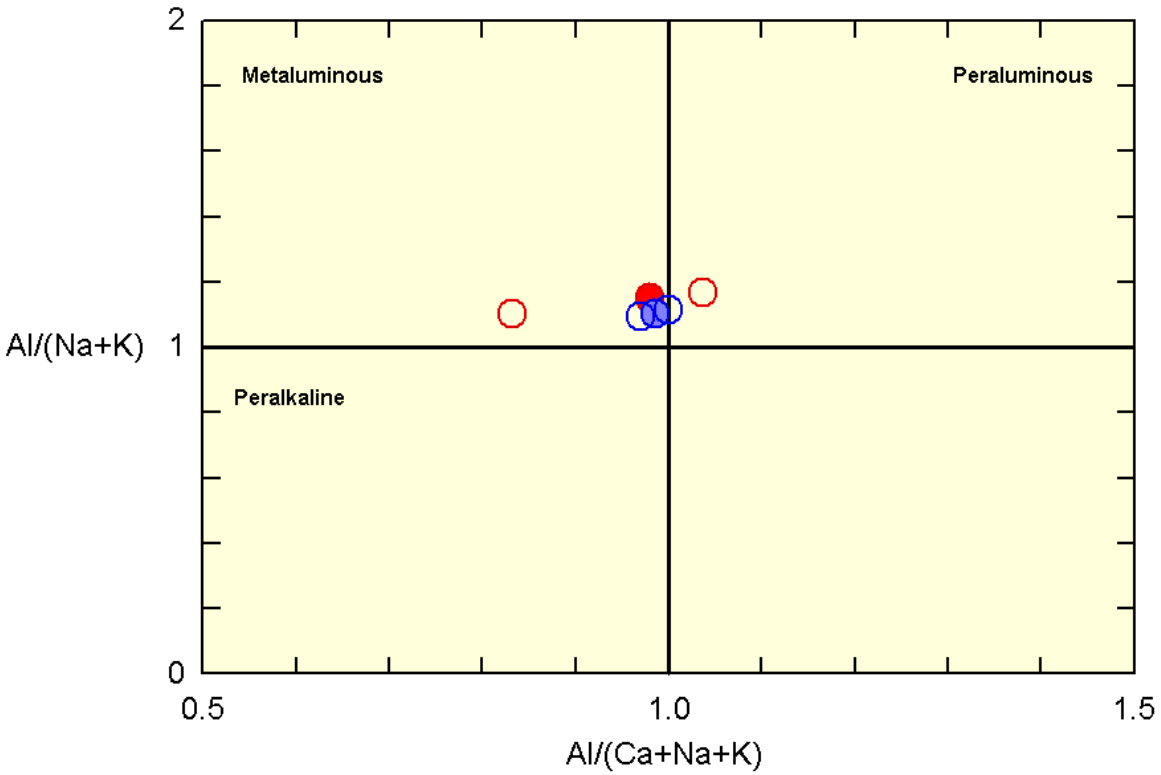

Figure 7: Alumina saturation index of Shand (1927) showing my calculations of the geochemical values of Obsidian Dome rhyolites reported by Vogel and others (1989) in their Table 1. Vogel and others (1989) define a high and low Ba rhyolite series. Red filled circle represents the average of 36 samples in the high Ba series whereas the blue filled circle represent the average of 41 samples in the low Ba series. The red and blue open circles represent the silica extremes in the high and low Ba series, respectively.

To place this in a specific context, Taylor and others (1993) obtained water content data from the Little Glass Mountain dome representing succession from initial explosion through dome extrusion. As reported in their Figure 1, Taylor and others (1993) note the progressive volatile depletion from ~2 wt% H_2O during initial explosion to as little as 0.1 wt% in the residual dome rocks. If we assume the temperature held fairly steady between explosion and initial dome extrusion at ~1200 K (~925ºC) then the Hess and Dingwell (1996) calculations reported in Figure 5 would show that viscosity increased by approximately 7 orders of magnitude.

Although the Hess and Dingwell model is for high-silica metaluminous melts, geochemical data from glasses obtained by Vogel and others (1985) reveal that some glasses penetrate into the peraluminous geochemical field (Figure 7). Given the high silica content of Obsidian Dome rhyolite, the viscosity model for metaluminous melts certainly serves as a reasonable model for hydrous high-silica peraluminous lavas (Dingwell et al., 1998), especially given the fact that some geochemical data plot in the metaluminous geochemical field. Hess and others (1995) ran experiments to determine the effect of the addition of alkalis to a granitic melt and have found that the addition of even a trace amount of alkali will drastically lower the viscosity of a haplogranitic melt. Because of the profound effect that alkalis place upon the physical properties of a high-silica melt, one expects that the depolymerizing effect of water to be somewhat larger for peraluminous melts

Other volatile species besides water (e.g. CO_2, SO_2, F) play a role in modulating the melt viscosity from the volatile-free ideal melt of the same composition. For example, It has been suggested by Wallace and Anderson (2000) that addition of dissolved CO_2, may lower the melt viscosity of a silica-rich batch of melt. However, since H_2O is clearly the dominant

volatile species in rhyolite melts, (Wallace and Anderson, 2000), it is considered to be the dominant network modifying species.

E. Spherulites

Spherulites are confocal assemblages of radiating crystal fibres that display wide varieties of shapes (spheres, bowties, blades among other forms; Lofgren, 1971a). A typical spherulite mineral assemblage includes quartz – or a high T polymorph – along with varying combinations of Na- or K-rich feldspars (Lofgren, 1971a; Lofgren, 1971b). Lithophysal spherulites describe a subset of spherulites that grow in expanding bubbles or vugs; the etymological origins of the suffix "-physe" in lithophyse according to Webster's Revised Unabridged Dictionary comes from Greek and means "flattus" or "air bubble." Both (non-lithophysal) spherulites and lithophysal spherulites exist on Obsidian Dome and will be described further in Chapter 3 and further discussed in Chapter 5.

F. Permeable Foam vs. Volatile Stratification Models

Research drilling in the summer of 1984 was conducted on Obsidian Dome in order to better understand the internal zonation and chemistry of the dome and to better elucidate the nature of the plutonic-volcanic transition (Eichelberger et al, 1985) (Figure 8A). This unique opportunity to view the internal structure of a youthful dome has lead to subsequent debates over the mode of emplacement upon the surface of the Earth (e.g Eichelberger et al., 1986; Freidman, 1989; Eichelberger, 1989; Fink, et al., 1992). One hypothesis, initially advanced prior to the 1984 drilling campaign, held that Obsidian Dome, along with other rhyolitic domes in the western United States effused onto the surface as "permeable foam"

with the resultant obsidian being a byproduct of bubble-wall coalescence and collapse (Taylor, et al, 1983).

Taylor and others (1983) in their figure 1, present hydrogen isotope data from Little Glass Mountain of the Medicine Lake Highlands in California which suggest that degassing of hydrous volatiles is largely an open-system process. Based on the isotopic data, Taylor and others (1983) hypothesize that an ascending batch of magma originally was water-rich and in the specific case of Obsidian Dome, had an initial water content of approximately 3 wt %, (Eichelberger et al., 1986). This water rich rhyolitic melt exsolved water as a hydrous gas during ascent to the surface, and then escaped via an interconnected network of bubbles to an unconsolidated "sandpile" of previously ejected pyroclasts. This gas escape into the "sandpile" then promoted subsequent collapse of bubble-walls by outward-flow (Eichelberger et al., 1986). Thus, according to the "permeable foam" model, the large quantities of obsidian present on Obsidian Dome formed secondarily (Eichelberger et al., 1986).

Alternative hypotheses regarding the emplacement of Obsidian Dome and the presence of obsidian as a *primary* feature were subsequently advanced in an attempt to explain the existence of high water content of the ascending batch of rhyolitic magma (Freidman, 1989; Fink et al., 1992). Obsidian is typically confined to discreet zones within Obsidian Dome which are: (1) not sufficiently thermally insulated as to promote crystallization, and (2) exist at conditions which resist vesiculation. Further discussion of the field relationships will be discussed in Chapter 3. Fink and others (1992) remark that volatile concentrations of Obsidian Dome lava were stratified originally in time-space and referred to this as the "volatile stratification" model. The result of volatile stratification is a succession of water rich to water poor magma being brought to the surface over the typical

eruptive sequence of initial explosive vent clearing to active dome extrusion, respectively (Fink et al., 1992).

Adding to the evidence which weighs towards a “volatile stratification” model for emplacement is field and laboratory evidence which suggests that some vesiculation occurs while the dome is being actively extruded (Fink and Manley, 1987). Finely-vesicular pumice (FVP) is typically restricted to the upper few metres of Obsidian Dome and forms as a result of effervescence of volatiles on the surface of the flow top (Fink and Manley, 1987). Coarsely-vesicular pumice (CVP), however, develops down-flow within the upper obsidian zone by the exsolution of volatiles from the crystallizing rhyolite interior. CVP then travels in the direction of the flow carapace via micro-fractures and expands within a zone stratigraphically above the underlying crystalline rhyolite (Figure 8B) (Fink and Manley, 1987).

In high silica rhyolite systems, near-surface conduit regions may preserve textures signifying repeat stick-slip events in similar fashion to tectonic fault gouge (Tuffen and Dingwell, 2005) owing to the viscosity of rhyolite melt. Based upon analyzing an ensemble of complex textures in high silica rhyolite conduits of Iceland, Tuffen and Dingwell, (2005) identify four phases in textural development: (1) the formation of initial fracture networks, (2) development of cataclasite zones from these initial fractures, (3) ductile deformation of the cataclasites and finally (4) the formation of microlite rich flow bands from annealed cataclasite. Metallic oxide microlite-rich bands in the Iceland case are taken to be relict clasts in fully annealed cataclasites (Tuffen and Dingwell, 2005).

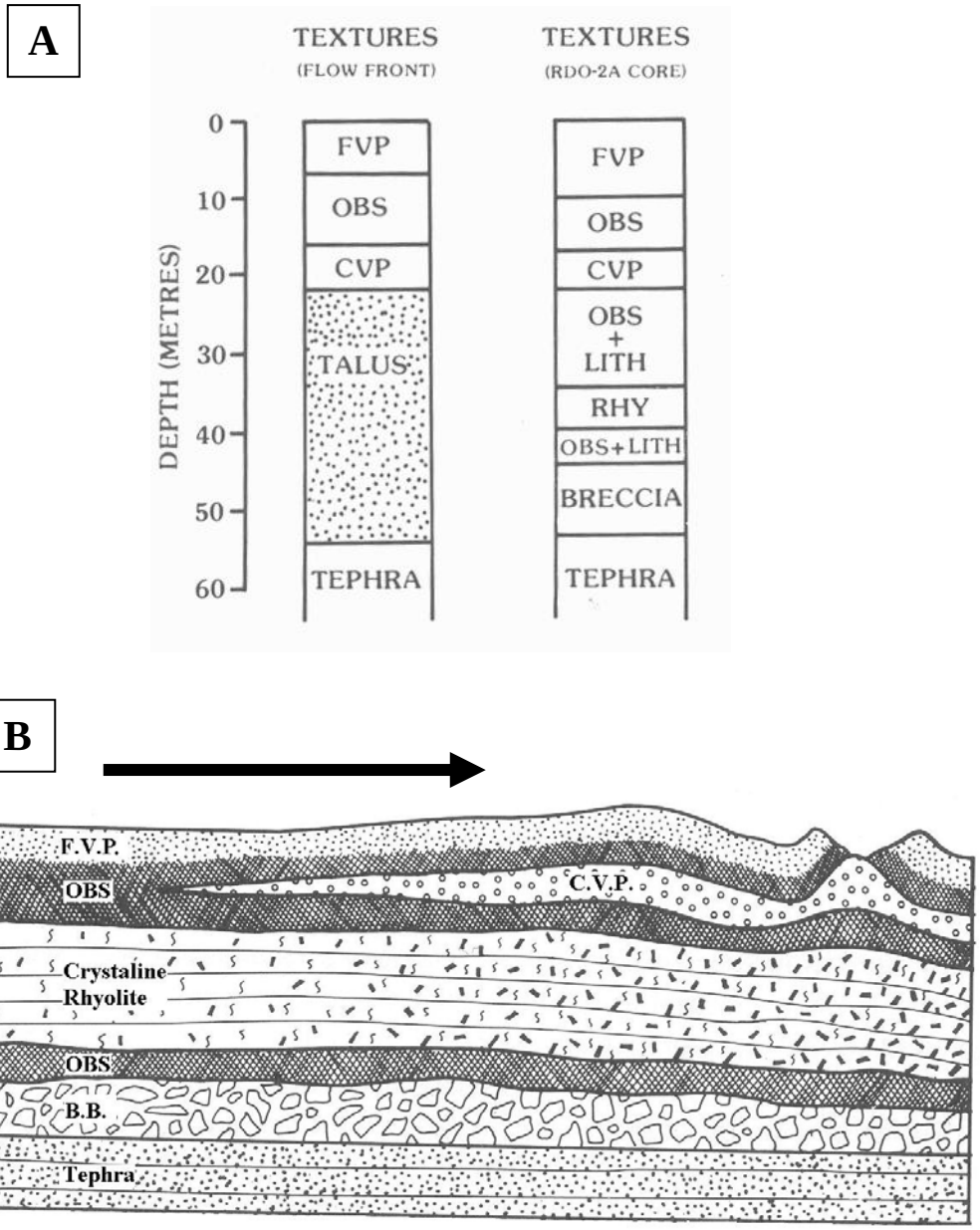

Figure 8: Internal zonation of Obsidian Dome. A: flow front and core log of Obsidian Dome. B: Idealistic cross section of Obsidian Dome showing zonation. Arrow points in the down-flow direction. Key to terms: F.V.P., finely vesicular pumice; C.V.P., coarsely-vesicular pumice; OBS, obsidian; B.B. basal breccia; LITH, lithophysae. Terminology and figure adapted and modified from Fink and Manley, 1987.

G. Glass transition and deformation of rhyolites.

Obsidian Dome rhyolites display a wide array of flow features and structures which may be divided into two broad families based on the mode of deformation: those arising from ductile deformation and those forming as a result of brittle failure. During active extrusion, Obsidian Dome lavas were subject to an ensemble of physical parameters (e.g. temperature, external stress, viscosity) which varied during the course of emplacement. A critical transition occurs when physical parameters favouring one mode of deformation (e.g. ductile) gives way to those which favour brittle deformation. This boundary condition is herein termed the "glass transition."

Dingwell and Webb (1989) observed that lavas have an intrinsic structural relaxation rate which varies directly with respect to temperature. If the external perturbation rate is less than the rate of structural relaxation (a function of viscosity) at a given temperature, an extruding batch of lava will flow as a paste and deform in a ductile manner (Dingwell and Webb, 1989). However if the external rate of perturbation exceeds the rate of structural relaxation, the lava will behave as a solid and be subject to brittle failure (Dingwell and Webb, 1989). Whether or not a material crosses the glass transition is dependant on many factors; an important parameter in this regard is time. Figure 9 graphically depicts the relationship between the glass transition on the one hand, and time-temperature space on the other. An important concept put forward by Dingwell and Webb (1990) as well as Tuffen and Dingwell (2005) is that given an isothermal system, large timescales of perturbation permit a polymer to flow and deform in a ductile fashion, while small timescales of deformation typically call for brittle failure, line A-B in Figure 9. If timescales of deformation of a polymer, however remain constant with decreasing temperature, then higher

temperatures tend to favour ductile shear whereas lower temperatures typically result in brittle fracture (Tuffen and Dingwell, 2005), line C-D in Figure 9.

The rate at which high silica rhyolites cool and its relationship to the glass transition can be quite profound. Gottsmann and others (2002) performed physical experiments on glasses from basaltic and tephrite basanite lavas to rhyolitic lavas. Based upon data they collected, fast cooling melts correspond to fast rheological equilibrium times, such as to avoid crossing the glass transition, whereas the opposite is true for slow-cooling systems and the differences thereof can be several orders of magnitude (Gottsmann et al., 2002). A global conclusion that can be made from these data among other independent analyses (e.g. Stevenson et al., 1995) is that high silica rhyolites, as well as more primitive melts, cross the glass transition at a higher temperature when cooling rates are fast. When the cooling rate is slow, the ductile-brittle transition occur at much lower temperatures (Gottsmann et al., 2002).

As a point of comparison of geologic interest, some pyroclastic surge deposits display rheomorphic features which indicate post-deposition ductile shear and flow *after* the magma fragmented as a result of the enormous stresses associated with volatile expansion. Andrews and Branney (2011), in their study of the welded Miocene Gray's Landing ignimbrite of southwest Idaho, document the presence of fiamme (flattened and stretched pumice) as well as doubly folded flow bands, the latter of which they cite as evidence of rheomorphic post-depositional flow. The end result is that welding and subsequent flow and folding of the rheomorphic Gray's Landing ignimbrite impart a competent "lava-like" appearance to an otherwise incompetent pyroclastic flow deposit and that timescales of deformation are a huge influence in the style of deformation (Andrews and Branney, 2011).

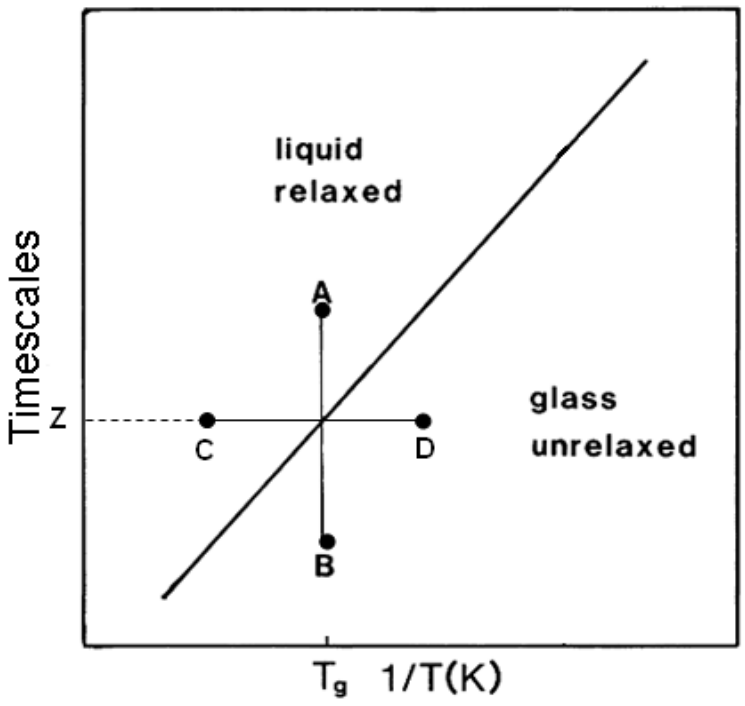

Figure 9: The time-temperature relationship of the glass transition. In an isothermal case, (line A-B) a polymer at condition A would be in the "relaxed" state and, thus would behave as a viscous fluid and deform in a ductile manner. That same polymer, when transitioning to condition B, continues to behave in a ductile manner until timescale Z is reached –the glass transition (T_g) at this particular temperature. Below timescale Z, the perturbation rates are too quick to permit ductile shear and the polymer then behaves in a brittle manner. Dingwell and Webb (1990) refer to polymers existing in conditions below the glass transition line as being "unrelaxed." If the timescales of deformation were to remain constant while temperature is permitted to change, however, then a polymer moving from condition C to condition D begins to behave in a brittle (unrelaxed) state when it crosses T_g . (Tuffen and Dingwell, 2005). Diagram modified from Dingwell and Webb (1990).

H. Deformation and shear flow:

During magma ascent to the surface, and subsequent extrusion, lavas are subject to an ensemble of deformational regimes in a continuum from 100% pure shear to 100% simple shear. In order to better constrain the physical parameters which influence lava emplacement, studies were undertaken to address the manner in which shear styles change over time and space and how strain indicators may be used to characterize these stress fields (e.g. Castro et al., 2002; Iezzi and Ventura, 2005; Manga, 2005; Rust and Cashman, 2007). Rust and Cashman (2007) in their Figure 3, present a series of photomicrographs which display stretched bubbles indicating they were strained. Bubbles whose semi-major axis runs parallel to the enclosing flow bands strained under pure shear conditions whereas in simple shear, the semi-major axis is angled from the flow bands (Rust and Cashman, 2007).

One aspect of lava flow fields is the systematic change from pure shear to simple shear stress fields down flow from the vent. Castro et al. (2002) analyzed rod-shaped microlite orientations in specimens sampled from the margins of Obsidian Dome and conclude that vent-proximal and near-surface obsidian record pure-shear deformation while the more distal domains are influenced by a component of simple shear. Iezzi and Ventura (2005) utilized enclaves from lavas of Porri Volcano in Italy as strain indicators and note the progressive change from pure shear to simple shear conditions as lava traveled further from the vent, (2005). In the case of vent-proximal lavas, the pure shear dominance is attributed to lateral extension of the flow away from the vent while gravity-driven flow in the distal portions impart to the flow field a simple shear overprint (Iezzi and Ventura, 2005).

I. Summary

The flow features and textural diversity displayed on Obsidian Dome (to be illustrated in the next chapter) are the direct result of the interplay between numerous physical properties of high-silica rhyolite as discussed above. As I have elucidated throughout this chapter, several parameters (viscosity, glass transition, volatile content) have a profound effect on the rheology of rhyolite, and the mode of volatile removal has ignited a debate over how Obsidian Dome – and by extension rhyolitic domes around the world – were originally emplaced.

Chapter 3: Field Observations

A. Introduction and Methodology:

Obsidian Dome is a 1.5 by 1.8 km kidney-shaped rhyolitic extrusion which erupted between 500-650 years ago, (Miller, 1985). Over a span of nine days during the summer of 2010, I documented several flow features and phases present that owe their distribution to a complex pattern of rhyolite effusion and explosion during cooling and solidification. In particular, field observations at the macroscopic scale, over several sites (Figure 10 and Appendix A) reveal that Obsidian Dome episodically flowed and fractured. Petrographic analysis of thin sections, (Chapter 4) further affirm that the complex emplacement of Obsidian Dome transcends into the microscopic realm.

Obsidian Dome shares many morphological characteristics with other high-silica rhyolite extrusions in the region. Firstly, a series of distinct troughs and ridges radiate concentrically away from a central vent area (Figure 11). Secondly, and perhaps one of the more striking features observed while conducting fieldwork is the presence of crease structures which Anderson and Fink (1992) attribute on other domes as forming by tensile stresses as the flow is forced to spread laterally (Figure 12B).

Despite its name, very little surface exposure of Obsidian Dome is actually *sensu stricto* obsidian but in fact, as pointed out in chapter 1, it is an extrusion consisting of multiple phases (Figure 8). During fieldwork, I observed five zones which constitute the Obsidian Dome: (1) a carapace of finely vesicular pumice which covers much of the top surficial exposure, (Figure 11), (2) dense black obsidian, where natural outcrops are largely limited to the dome margins, (3) coarsely vesicular pumice that form prominent crease

structures in the southern distal facies of the extrusion, (4) light to medium grey dense crystalline rhyolite which are largely present as mingled domains that deflect flow banding and (5) discontinuous lenses and zones of orange, highly altered autoclastic breccias. My observations listed above are in general agreement with previous mapping of the eruptive phases by Sampson (1987). However, the autoclastic breccia zones, compared to the other phases are volumetrically subordinate and do not crop out in scales that would be able to be mapped such as the scale of map produced by Sampson (1987) and reproduced in Figure 11A. Also, it can be difficult to distinguish finely vesicular pumice from the crystalline rhyolite in places where they are in close proximity perhaps due to the fact bubble densities sometimes change gradationally and, thus represent a continuum between pumice on the one hand and crystalline rhyolite on the other.

The margins of Obsidian Dome afford a particularly unique opportunity to illustrate the field relationships between the different eruptive phases of Obsidian Dome, since in several locations, in-situ outcrops are well exposed and display units which on the top surface of the dome are normally covered by a carapace of fine vesicular pumice. As a consequence, detailed work was largely done along the cliffs that represent the margin so as to maximize the observation of stratigraphic variability. After having done a reconnaissance circumnavigation around Obsidian Dome I selected three locations along the margins which appeared particularly well exposed, relatively free of talus blocks, and reasonably safe to climb. At each of the three locations, clustered on the eastern margin (10-OD-05, 10-OD-07 and 10-OD-10) and shown on Figure 10) I completed representative graphic logs, and documented in detail, the different zones and domains based on physical characteristics and the structures, if any contained in each of the zones. The resultant graphic logs and associated descriptions of these zones are illustrated in figures 13-15. On the western

margins of Obsidian Dome, (10-OD-08, 10-OD-09 and 10-OD-13) Figure 10, I simply documented the structures and phases on the cliff faces since the outcrop at these locations were not obviously layered. Additionally in October of 2010, I travelled to Salt Lake City, Utah, USA to measure and describe Continental Scientific Drilling Program core # 2A (hole #1 in Fig. 4) spudded under the supervision of Eichelberger and others (1985).

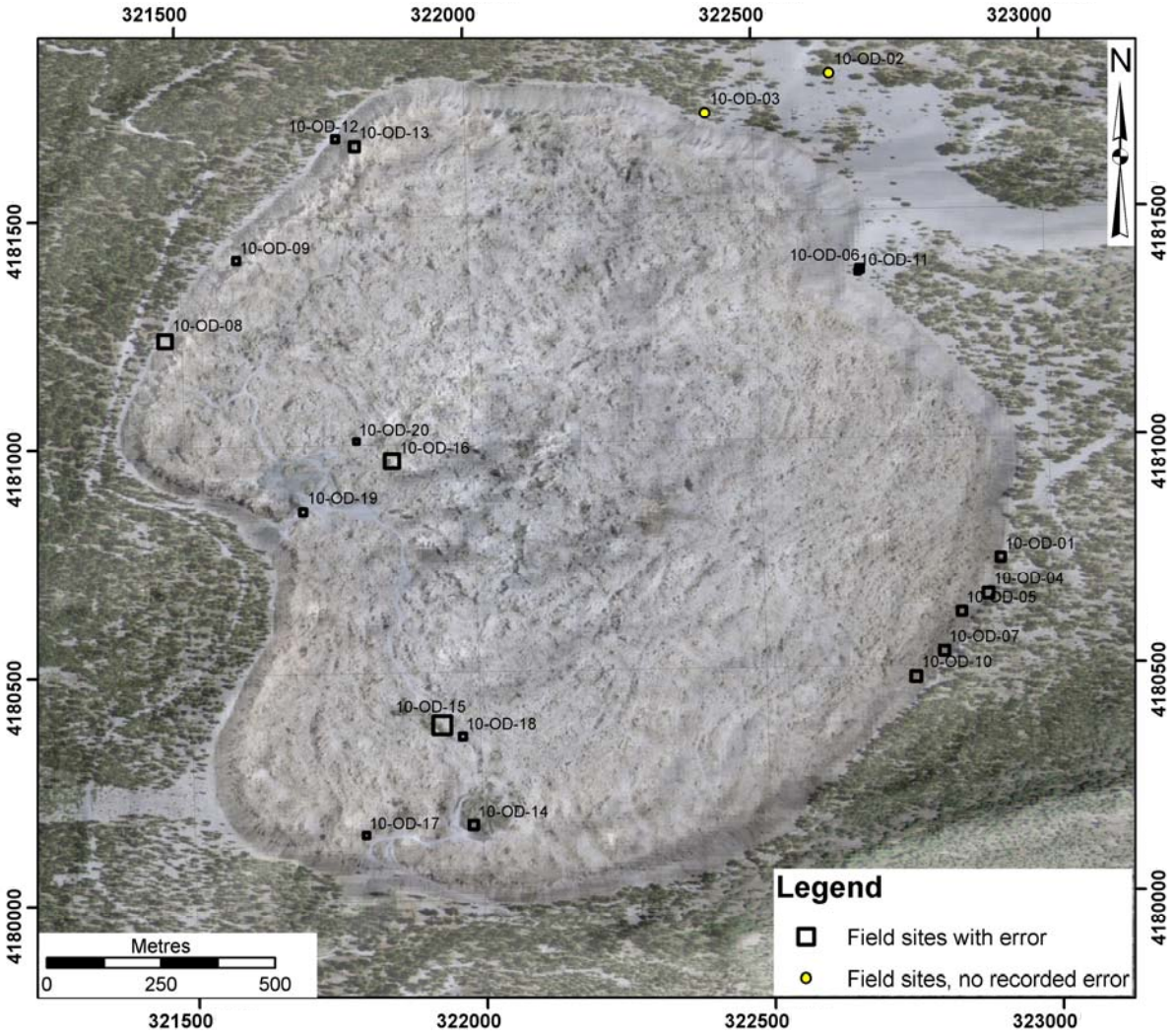

Figure 10: Image of Obsidian Dome showing the distribution of field sites. Black squares indicate positional error (accuracy) for each field site as derived from Global Positioning System data. UTM measurements are based on the World Geodetic System (WGS) of 1984, zone 11. True-colour orthoimagery is from the U.S. Department of Agriculture's National Agriculture Imagery Program, (NAIP) and has been draped over a hillshade derived from a 1/3 arc-second Digital Elevation Model from the National Elevation Dataset.

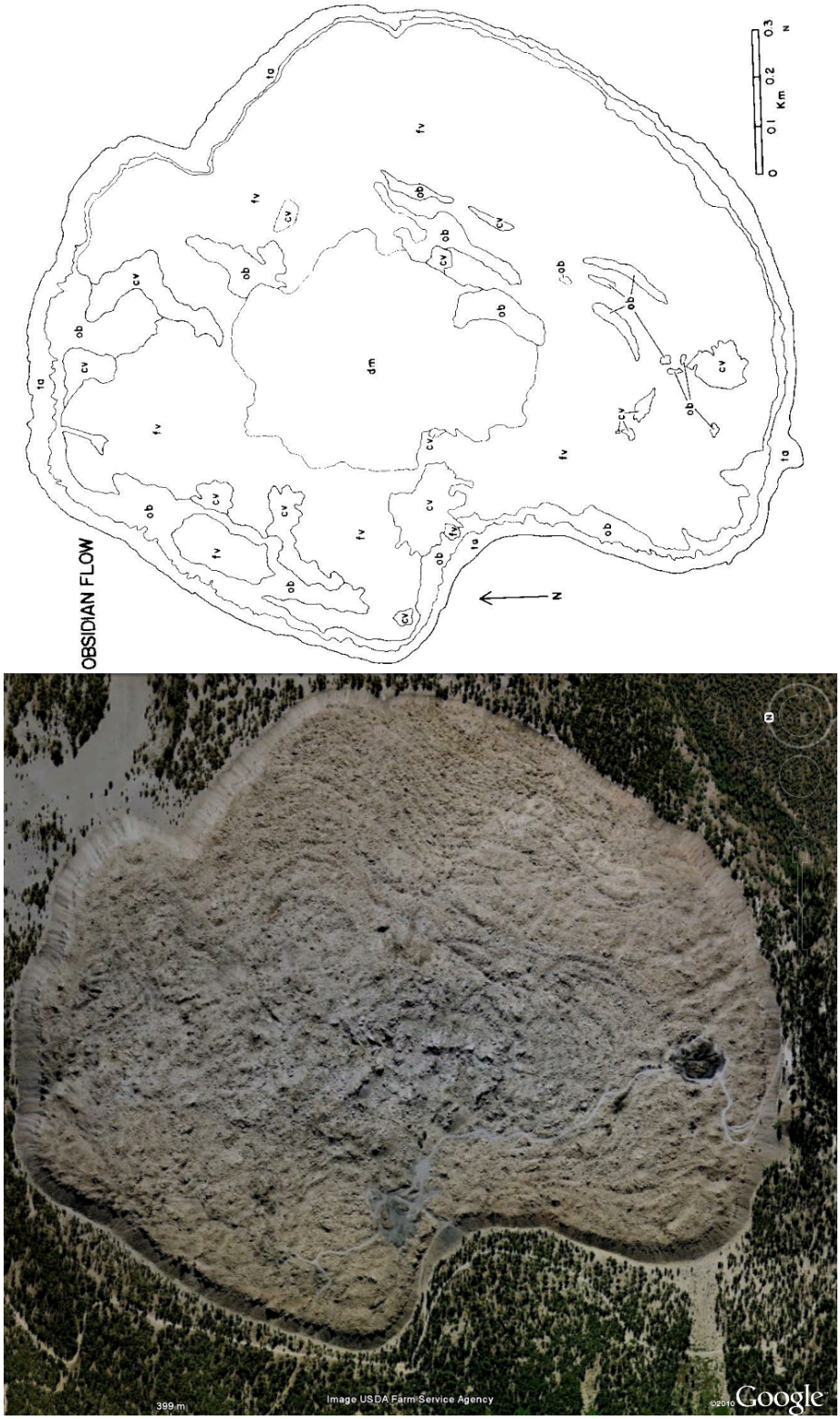

Figure 11: A: Textural map and B: Google Earth ® imagery of Obsidian Dome. Key to annotations as modified from Sampson (1987): fv = finely vesicular pumice; cv = coarsely vesicular pumice; ob = obsidian; dm = dense microcrystalline rhyolite and ta = talus. Note that much of the top carapace of Obsidian Dome is finely vesicular pumice while the obsidian is largely relegated to the dome margins. Note the lobate ridges that confocally disperse from the central core of the dome.

Figure 12A: Representative view of the western margin of Obsidian Dome looking east as seen from the access road. The black zone that crops about halfway up the slope is dense black obsidian while the tan coloured rocks are principally carapace, finely vesicular pumice.

Figure 12B: Photo showing the dark grey crease structure, centre. Dominantly composed of dark grey, coarsely vesicular pumice, the arrows show how tensile stress can tear apart a rising mass of relatively buoyant material after piercing the flow carapace. The surrounding rock is principally finely vesicular pumice.

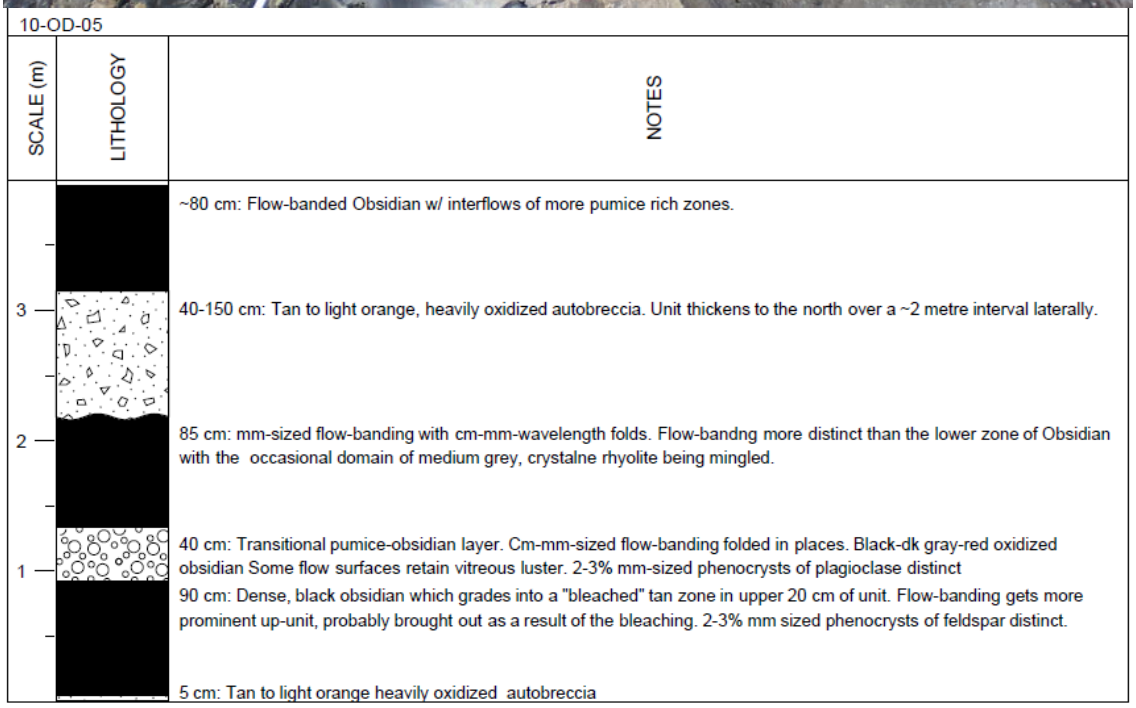

Figure 13: Photo (above) and graphic log (below) of section 10-OD-05. White measuring staff marks profile location. Measurements of units above wavy line in column could not be determined using measuring staff and were thus, approximated. Zones dip ~60 degrees into the dome. Note bleached (white) areas below the dark grey-brown central zone interpreted to have been caused by gas migration.

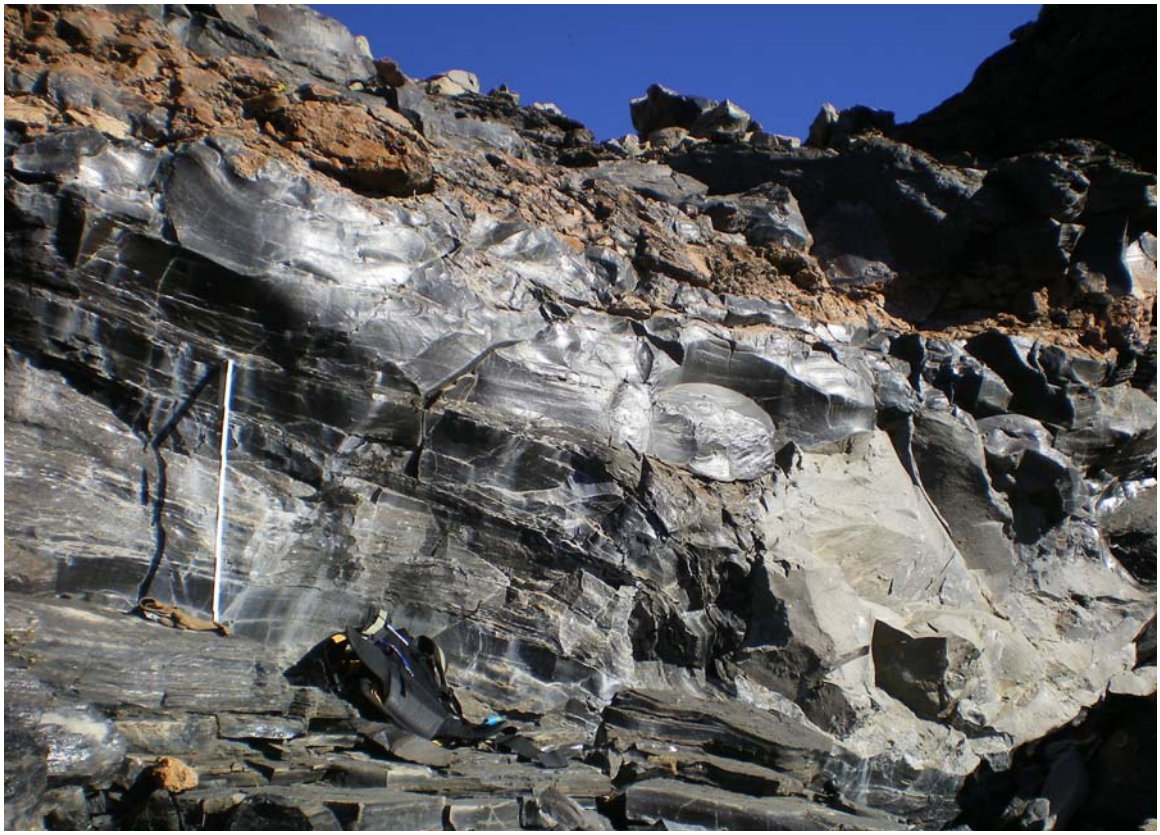

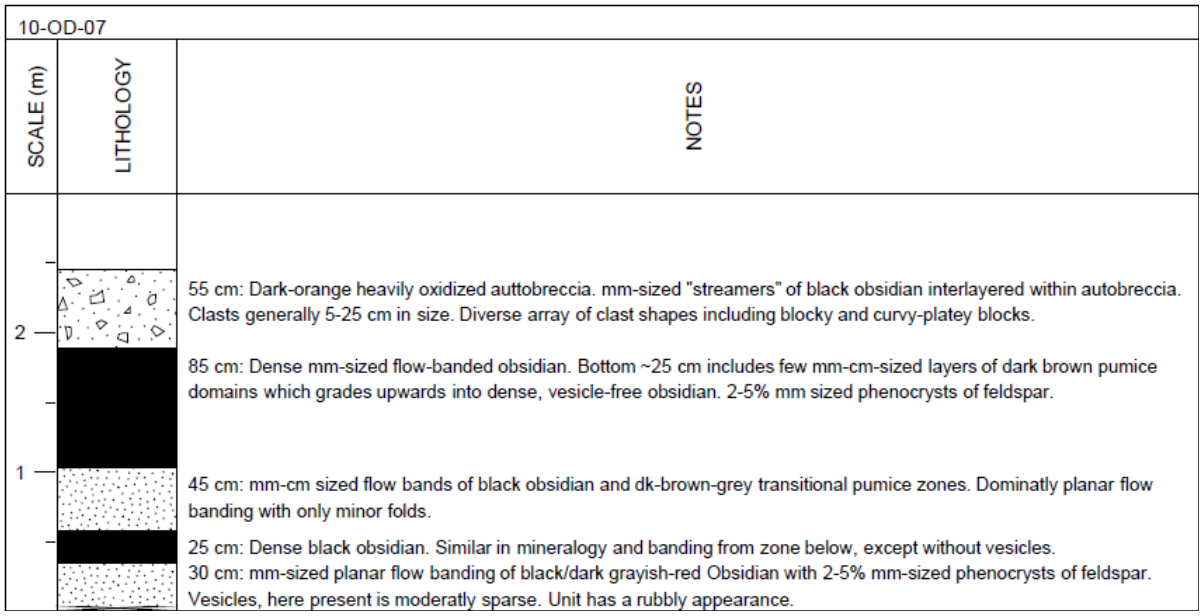

Figure 14: Photo (above) and graphic log (below) of section 10-OD-07. White measuring staff marks the location of where the measurements were taken. Note the large domain of medium grey rhyolite deflecting flow bands of obsidian and pumice. Approximate dip here is ~45 degrees away from the dome the dome.

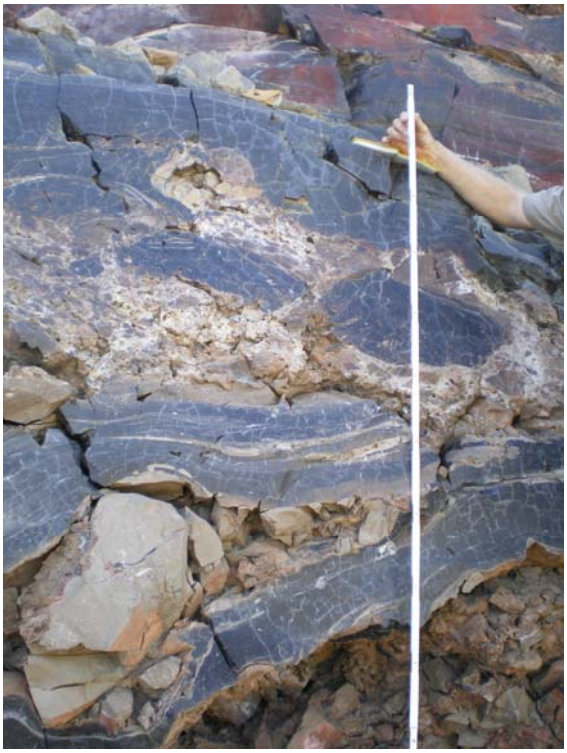

10-OD-10L

10-OD-10U

Figure 15: Caption next page.

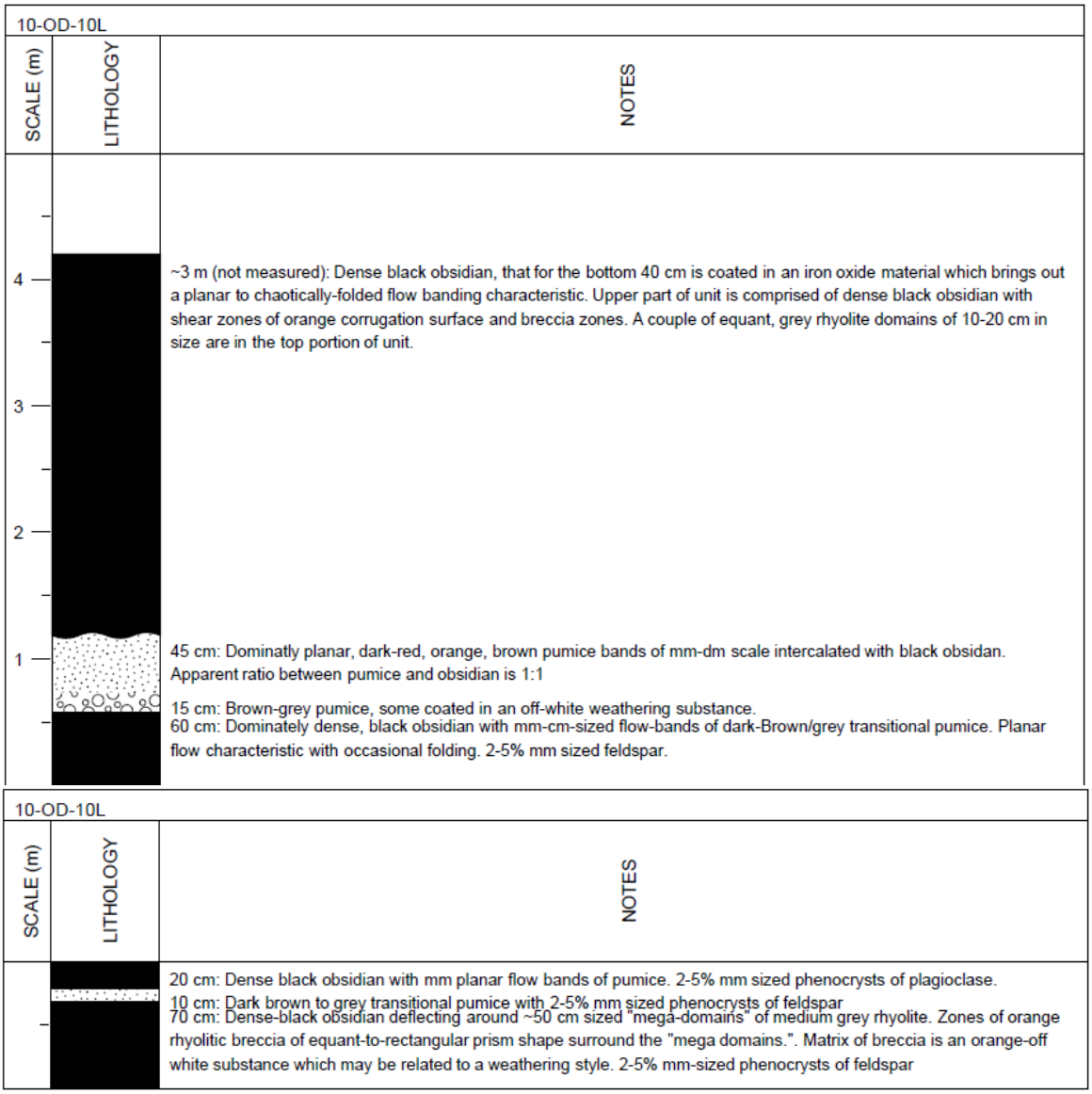

Figure 15: Photographs (previous page) and graphic logs of composite section 10-OD-10, which is divided into a lower sub-section (10L) and an upper sub-section, (10U). The top photograph on the previous page shows the relationship between the two sub-sections with the white measuring staff placed at 10L and the black walking stick placed at 10U. The two photos at the bottom of the previous page show more closely the characteristics of each subsection. Measurements of units above wavy line in column 10-OD-10U on this page could not be determined using measuring staff and were thus, approximated.

B. Brittle Deformation Structures

As previously stated in chapter 2, when the external rate of stress applied is greater than the rate to which molten rhyolite is able to structurally relax, brittle failure results (Dingwell and Webb, 1989). There are a myriad of different structures discovered on Obsidian Dome during the course of the logging which record brittle failure at a variety of scales. These structures may be grouped into four families: (1) dilatant en echelon fractures; (2) transverse fractures, (3) minor faulting and (4) basal breccia.

Dilatant en echelon fractures record rotation of the greatest principal stress with the fracture tip pointing in the direction normal to the greatest principal stress (Pollard et al., 1982), and thus are chiefly a result of translational deformation (Figure 16). Two stages of en echelon fracture patterns are shown in Figures 16. Figure 16A shows an ensemble of 5, cm-scale lens-shaped fractures that are inclined to one another. I interpret the evolution of this feature as being initiated by incipient fracturing oriented normal to the maximum principal-stress, followed by stress field-influenced translational rotation during the evolution of this ensemble. My observation is consistent with that offered by Pollard and others (1982) who have done theoretical modeling on en echelon splitting patterns in a wide array of geologic environments. En-echelon fracture ensembles such s those shown in figure 16A, that have evolved through continuous translational rotation and splitting, have fracture patterns similar to those shown in figure 16B.

Transverse fractures tend to form by tensional stresses on the outer surface of curvy-planar concave-downward surfaces, and are oriented normal to the direction of maximum curvature (Figure 17). They behave much in the same way as a hinge as a way to accommodate stress. Small-scale faulting can offset domains of finely vesicular pumice mingled with dense obsidian, (Figure 18) and possibly represent a later stage of syn-eruptive

deformation. Finally, brittle deformation may entirely break up otherwise coherent rhyolite, and form brecciated zones, often with an orange oxidized colour, signifying interaction with hot gas during active extrusion (Figure 19).

Figure 16A: Photo showing mid-stage en-echelon fracture deformation of finely vesicular pumice. Arrows show relative displacement on either side of the fracture set. The width of the ring-finger on the leather glove is about 2.5 cm.

Figure 16B: Photo showing a more advanced stage of en-echelon fracture deformation on a carapace of finely vesicular pumice. Arrows show relative displacement on either side of the fracture set. Note the sag in the transverse filaments.

Figure 17A: Small, mm-scale transverse fractures cutting a smooth curved surface of finely-vesicular pumice.

Figure 17B: Large, dm-scale transverse fractures cutting across both finely vesicular pumice (tan regions) and coarsely vesicular pumice (medium gray regions).

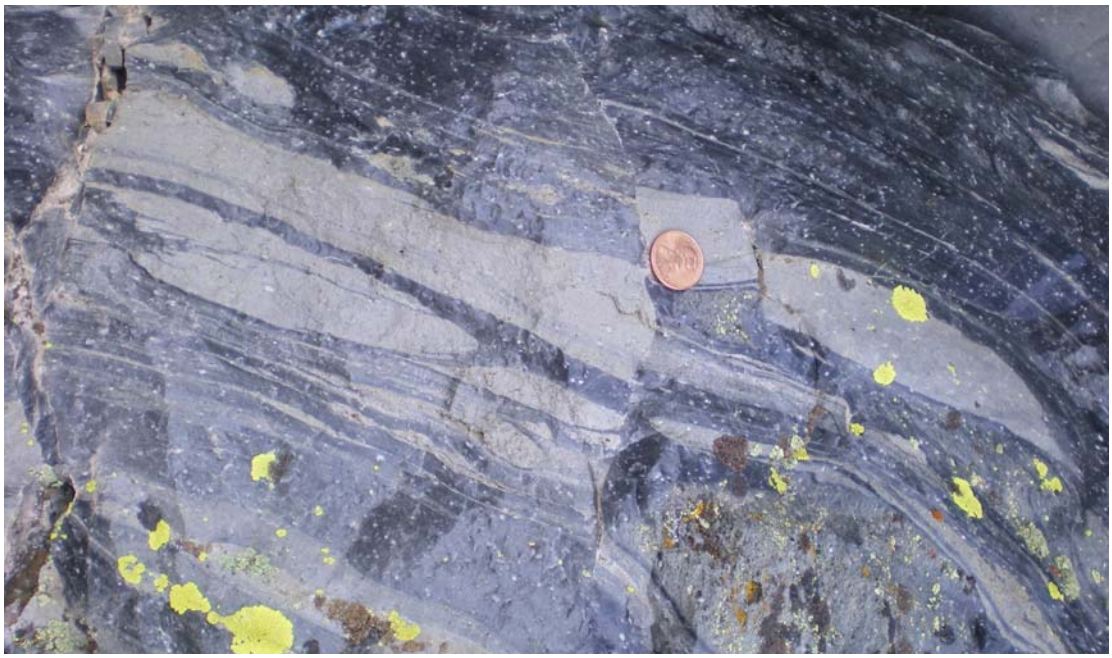

Figure 18A: Two small faults displacing by ~2 cm a finely vesicular pumice domain mingled with dense obsidian.

Figure 18B: Example of small-scale fault displacing a composite mm-sized flow bands of obsidian in a finely vesicular pumice on a block from the talus pile.

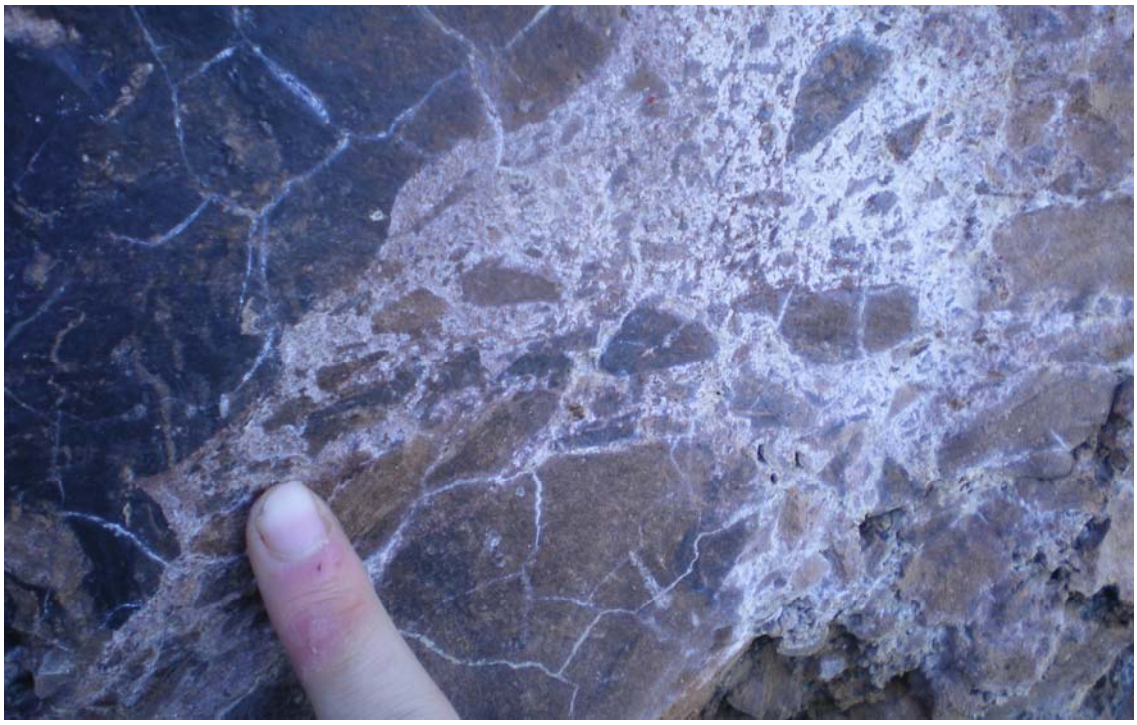

Figure 19A: Autobrecciation of slightly oxidized obsidian set in a highly oxidized matrix. Finger for scale

Figure 19B: A more typical exposure of autobrecciation. Note the bright orange colour signifying intense oxidation of the enclosing breccia clasts.

C. Ductile flow features

Above the glass transition, when the external rate of stress is less than the threshold for strain of a rhyolitic melt at a given temperature and timescale, it behaves as a viscous fluid, similar in concept to toothpaste at ambient temperature (Dingwell and Webb, 1989). Several flow features on Obsidian Dome testify to the ability of rhyolite to plastically deform at the surface despite its high viscosity. Chief among these features are (1) meso- to macro scale folding, (2) deflection of flow bands around both phenocrysts and domains of finely vesicular pumice, and (3) corrugation surfaces.

Folding is among the most common ductile regime flow feature on Obsidian dome and exists on numerous scales from the microscopic to the macroscopic and exhibit widely divergent degrees of complexity (Figure 20). When rhyolite encounters a domain which resists compression during active extrusion, (e.g. phenocrysts and other eruptive phases), flow bands commonly deflect around said domain and, in some cases may show evidence of rotation during the active extrusion (Figure 21).

In many regions of Obsidian Dome, though particularly abundant along the margins of the extrusion, are surface features which resemble “pahoehoe” flow texture common among basaltic flows. However, since the viscosity of rhyolite is several orders of magnitude higher than that of basalt, it almost certainly formed by a different process. For example, Fink and others (1992) in their Figure 5 show an outcropping of rhyolite that is remarkably similar in appearance to my Figure 22. In their discussion of the aforementioned figure, they propose a model that calls for differential expansion of flow bands in response to varying water content in the individual bands during active flow (Fink et al, 1992). Thus, a flow band that is comparatively water rich would expand into a bulbous form that protrudes outward from bands that are relatively water-poor. In order to separate this striking feature from the

similar-looking pahoehoe morphology that is abundant on young basalt flows, I herein apply appropriate term “corrugation surface” (Figure 20).

In the previous section regarding brittle features, I described that Figures 16A and 16B were dominantly the result of brittle deformation. In the case of Figure 16A, I observe that the fracture walls contain a series of interconnecting thin, ~2 mm wide ribbons of obsidian glass. In figure 16B, which is a more advanced stage of en-echelon splitting, the mm-scale ribbons are folded as a result of sagging, indicating ductile deformation across the fracture which resulted from brittle deformation.

Figure 20A: Chaotically folded flow bands within obsidian. Shoe, provided for scale is about 12 cm wide.

Figure 20B: Centimetre-scale disharmonic folding in coarsely vesicular pumice. Coin provided for scale is 2 cm in diameter.

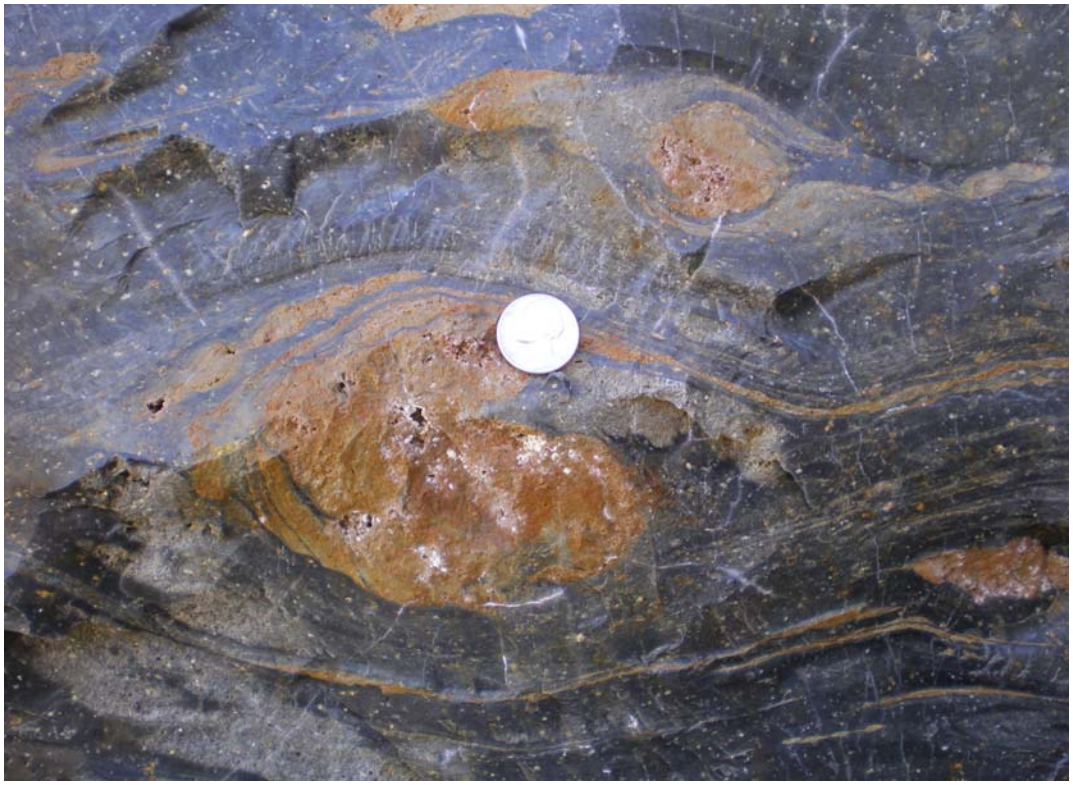

Figure21: Millimetre scale flow banding being deflected around domains of highly oxidized rhyolite. The large domain in the centre of the image shows evidence of rotating counter-clockwise during active flow. Coin in the centre (2 cm) is provided for scale.

Figure 22: Example of corrugation surface.

D. Flow-banding

Among the most striking characteristics of Obsidian Dome lavas are mm-cm thich planar bands of contrasting rhyolitic zones that are pervasive in the various eruptive products (e.g. obsidian, coarsely vesicular pumice). Termed “flow bands,” field observations at Obsidian Dome reveal that flow banding varies widely in manifestation and degree of structural complexity. For example, in some outcrops flow bands are quite planar, showing little apparent evidence of internal deformation. In other outcrops however, flow bands are chaotically folded, owing to the local compressional stress regimes at the time of flow in that particular location.

Flow bands are a pervasive feature in rhyolite lava domes and flows worldwide. Consenquently, qualitative and numerical modeling of the extrusion parameters of lava domes and flows have been immensely improved due to the presence of flow bands (e.g. Seaman et al., 1995; Smith, 2002; Perugini et al., 2004; Gonnermann and Manga, 2005; Castro et al., 2005). Flow banding on Obsidian Dome has historically been defined based on density of microlites (Figure 23A) (Figure 1C of Castro et al., 2005). However, field analysis in regions of coarsely vesicular pumice reveals that flow banding may also be defined by distinct planar zones of relatively thick bubble walls inter-banded with zones of relatively thin bubble walls (Figure 23B). As a point of comparison, obsidian collected by Gonnermann and Manga (2005) from Mayor Island in New Zealand contains flow banding which is defined principally by varying degrees of vesicularity. In outcrops of Obsidian Dome where obsidian lava deflected around crystalline rhyolite domains, part of the rhyolite domains have been sheared into flow bands, (Figure 21).

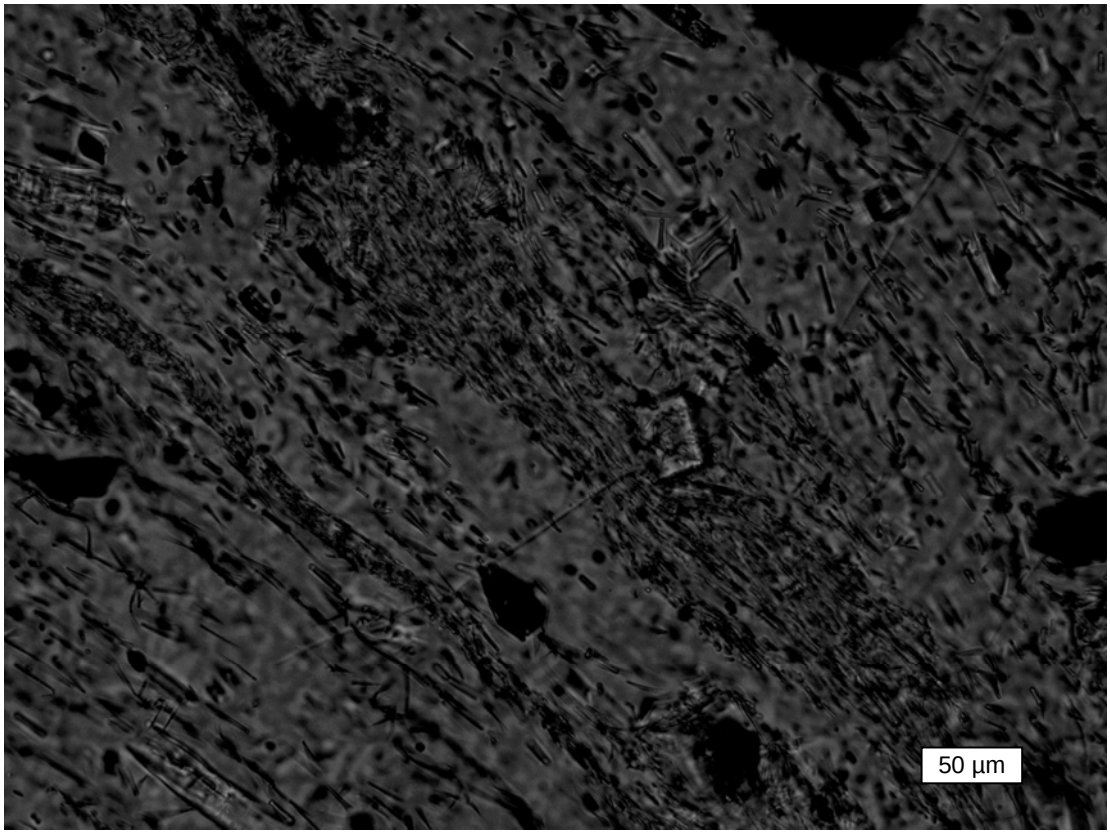

Figure 23A: Photomicrograph of slide 10-OD-13D showing contrasting densities of microlites between flow bands of obsidian, magnified 50x. Scale bar in lower-right of image.

Figure 23B: Flow banding defined by contrasting bubble wall thickness in coarsely vesicular pumice on Obsidian Dome. The darker bands constitute bubbles with thicker walls.

E. Spherulites:

Even though spherulite-bearing rhyolite does not comprise a significant part of the surficial exposure of Obsidian Dome, their presence in the dome interior – confirmed from research drilling – is significant enough to discuss here. In all field sites visited on Obsidian Dome, spherulite-bearing obsidian crops out only on the northwest margin of the extrusion (for 10s of m^2 surrounding sites 10-OD-12 and -13, Figure 10). Two families of spherulites exist: (1) lithophysal spherulites, and (2) non-lithophysal spherulites. Figure 24A shows an example of a lithophysal spherulite, whereas Figure 24B shows a non-lithophysal spherulite. The lithophysal spherulite in Figure 24A clearly demonstrates that a concentration of spherulites grew within an air bubble that subsequently expanded, separating individual spherulites during a time when the rhyolite was able to deform in a ductile manner. This observation supports previous work by McPhie and others (1993) who argue that lithophysal spherulites are an early-stage crystallization phenomenon.

Figure 24: Field examples of the two types of spherulites: A: Lithophysal spherulite and B. non-lithophysal spherulite. The Lithophysal spherulite shows evidence that some deformation occurred *after* spherulite crystallization, when the enclosing rhyolite was still hot enough to behave plastically.

In contrast to the lithophysal spherulites discussed above, non-lithophysal spherulites, may represent in general, a later-stage crystallization phenomenon. The non-lithophysal spherulite shown in Figure 24B lacks evidence it grew from within a bubble. Additionally, flow bands adjacent to the spherulite shown in Figure 25 are not deflected, and therefore can be concluded that in this example spherulite growth occurred after flow banding. The timing between non-lithophysal spherulite growth and flow banding however is not exactly universal, as Denis (2011) shows evidence that in some cases, non-lithophysal spherulites do deflect flow banding.

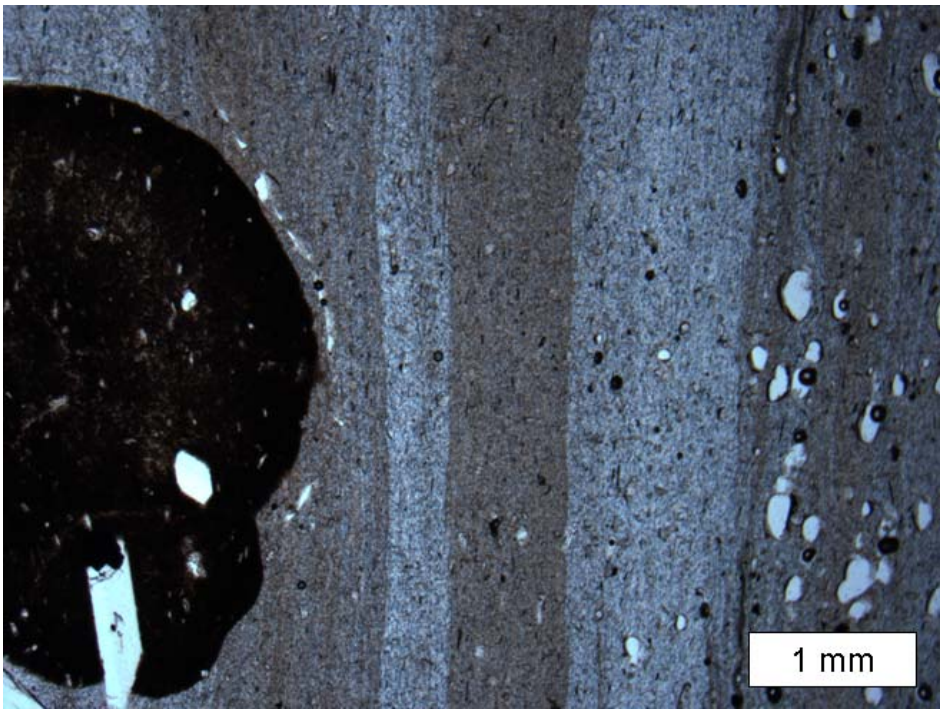

Figure 25: Thin section of 10-OD-3 showing the relationship between a non-lithophysal spherulite (black blob on the left) and microlite-defined flowbanding. Note the lack of deformation of flow banding immediately surrounding the spherulite.

F. Pyroclastic deposits

While the major thrust of this thesis centred on the characteristics of dome effusion, I surveyed pyroclastic material that is remarkably most abundant on the northeast margin of Obsidian dome. This observation is supported by data from Miller (1995) that documents an initial explosive event that was carried to the northeast by wind. From the base of the dome and extending out to ~200 m away from the talus pile margin, many dm-sized pyroclastic blocks and bombs are strewn over an area about 90,000 m^2 (Figure 26A). In many cases, these blocks and bombs remained in-situ since the pyroclastic event, as signified by (1) a network of radial fracturing shown in Figure 26B which indicate hot impact or (2) in the case of the block in Figure 26C, created a small, 40-60 cm wide impact pit within which it sits.

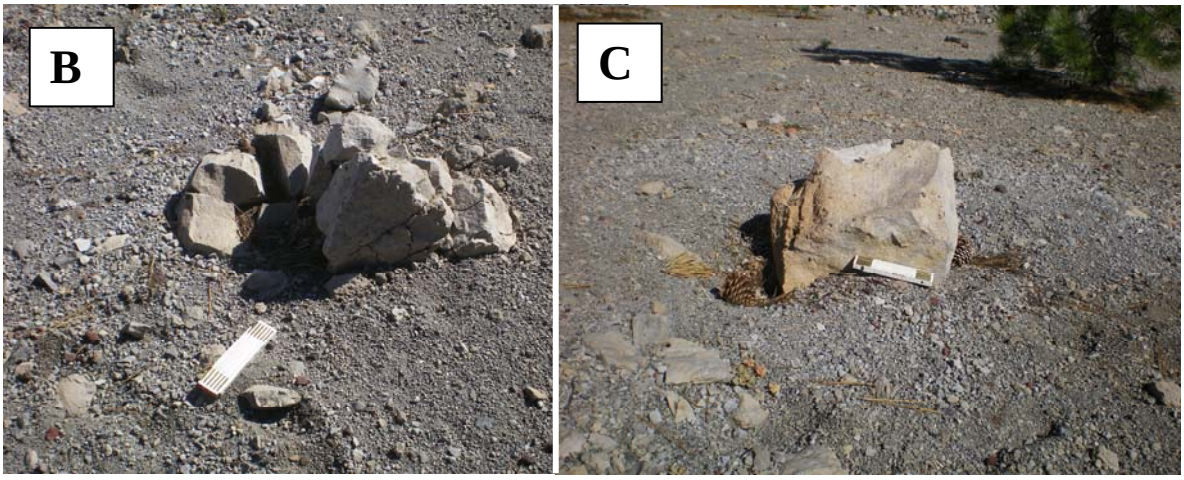

Figure 26: The pyroclastic phase of Obsidian Dome. A: photo showing much of the proximal pyroclastic field on the northwest margin of Obsidian Dome. The northeast margin of Obsidian Dome is shown in the upper-left quadrant. Circled block in the centre of the image is the same block shown in part C of this figure; B: Radially-fractured pyroclastic bomb; C: Pyroclastic block sited within a small ~40-60 cm, clearly defined impact pit; this block is the same circled block circled in the centre of part A in this figure (previous page). In B and C, the folded accordion-measuring staff is ~10 cm in length.

G. Evidence for repeat brittle-ductile deformation

In a simplistic extrusion model for a lava dome, ductile deformation generally is followed by brittle behaviour as the temperature of the extruding lava decreases over time and the glass transition is crossed. However, over the course of field work, I documented compelling instances where more than one generation of the ductile-brittle transition has taken place on Obsidian Dome. In one example, (Figure 27A) pumecious, flow-banded rhyolite was fractured and was then subsequently in-filled with another layer of flow-banded rhyolite which drooped into the fracture, signifying ductile flow *after* fracture. I interpret the layering in Figure 27A as representing one flow within which, different bubble densities impart slight rheological differences between layers. In a separate case, (Figure 27B) I observed flow banded rhyolite which was faulted and then subsequently took on a corrugation surface appearance by differential inflation (see section C for the discussion as well as Figure 22 for comparison) and, in the vicinity of the fault an inflated water-rich zone of the corrugation surface folded over the fault, annealing it similar in concept to a scab healing a wound. The fracture in Figure 27A and the faulting in Figure 27B resulted when the rate of perturbation was greater than the ability of the rhyolite to deform. The subsequent drooping of thin, cm-sized bands of obsidian show that, relative to the fracture it infills, the rate at which the rhyolite was perturbed had obviously decreased. In the same vein, because the ribbons in Figure 16B had to have been created first through the act of en echelon fracturing (a brittle failure phenomenon) as a prerequisite for said ribbons folding, brittle failure in this instance occurred immediately prior to folding and may in the advance stages, run concurrently.

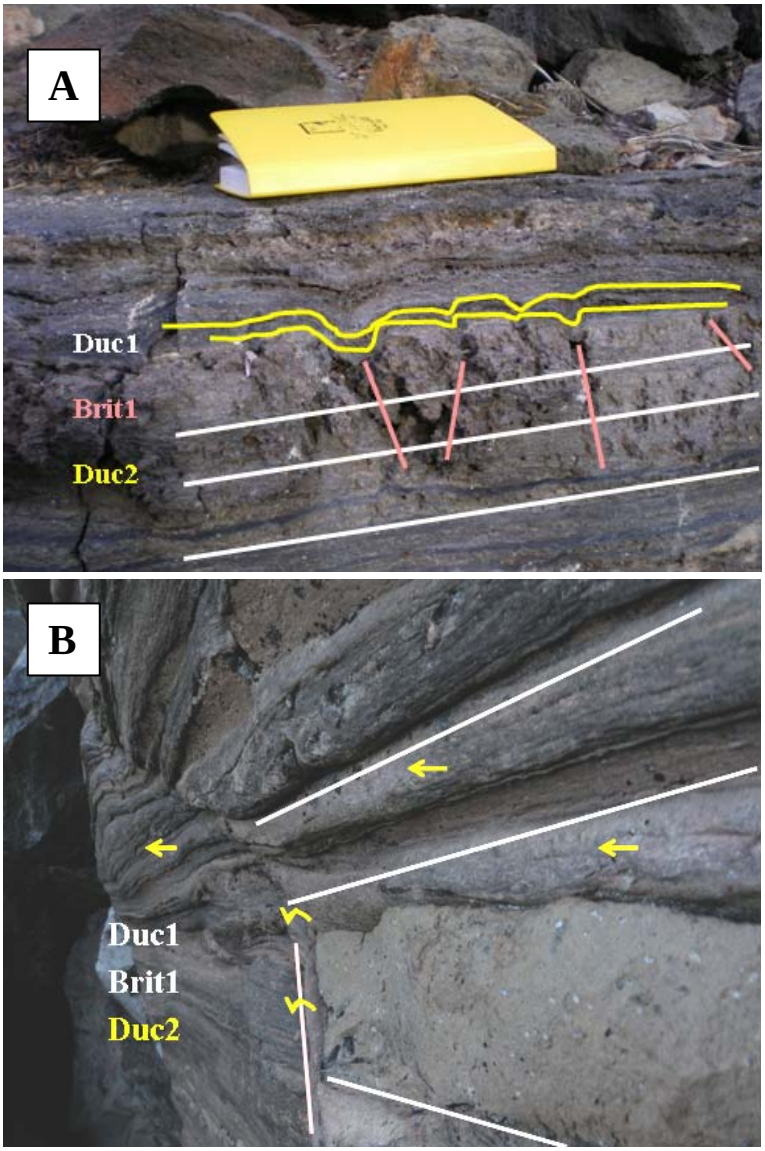

Figure 27: Outcrop-scale evidence of repeat ductile and brittle deformation generations. A: Annotated photograph showing the deformational history of this particular block from field site # 10-OD-01 at Obsidian Dome, Figure 10. Duc1 represent the first phase of ductile deformation, signified by flow bands of pumice. Brit1 represents the first phase of brittle deformation, here manifested by sub-vertical fractures which break up the pumice. Planar, more dense flow banded obsidian then partially fills the crack (note the droop folds), representing a second generation of ductile deformation, Duc2. This is ll one flow but has an inhomogeneous vesicle distribution. B: Annotated photograph showing the deformational history of this particular outcrop of Obsidian Dome. An initial phase of shear produced flow banded rhyolite, which was subsequently faulted and then subsequently took on a corrugation surface appearance by differential inflation of flow bands.

H. Summary

In Sections B and C of this chapter, I documented a myriad of structures and flow features on Obsidian Dome which developed as a direct result of brittle failure and relaxed flow during the course of emplacement upon the surface. In Figure 16B, I show the development of dominantly brittle, en echelon fractures which display evidence of ductile folding that occurred *after*, and in the more advanced stages of development, *concurrent to* the brittle regime. Conceptually, these en echelon splitting patterns, as well as other types of fractures, formed because the strain was locally concentrated such that the emplaced rhyolite responded to that strain in an unrelaxed fashion. In the case of Figure 16B which show folding after initial tear, that initial concentration of strain was released, allowing ductile folding to occur.

Due to its status as one of the youngest rhyolite extrusions in North America and its location in a semi-arid environment, Obsidian Dome affords a unique opportunity to observe many of the fine scale features and to infer the qualitative parameters of emplacement upon the surface. Examples of repeat brittle-ductile behaviour illustrated in the discussion and shown in the figures below serve as a window into the complex interplay between external stressors and the ability of high silica rhyolite to respond to these stresses. It is functionally certain that there are numerous other examples of repeat generations of flow and fracture throughout Obsidian Dome (and the adjacent Glass Creek and Deadman Domes to the South, among other extrusions in the Long Valley region). I therefore suggest that repeat brittle-ductile deformational regimes are a persistent process during active extrusion of Obsidian Dome and other similar structures worldwide. An open question that this work does not directly address and, potentially deserves further study, is how close in succession do these

brittle-ductile generations occur? Did they potentially happen on time scales of minutes to hours or is it a longer term phenomenon?

Chapter 4: Laboratory Analysis

A: Introduction

While the principal thrust of this study is to infer the extrusion dynamics through careful field investigation of the 550-650 year Obsidian Dome, laboratory analysis of the eruptive products were nonetheless undertaken in order to make sense of the textural, mineralogical and geochemical aspects of Obsidian Dome. Accordingly, I review and make interpretations of results arising from microscopic, Electron Microprobe (EMP) and X-Ray Diffraction (XRD) analysis.

B. Petrographic Analysis

B.1: Introduction

In the previous chapter, (Chapter 3) I documented the in-situ field distribution and characteristics of structures and flow features of Obsidian Dome. Further, I interpreted these structure and flow features to make inferences regarding the sequence of events that occurred during active dome extrusion. In order to get a more complete insight regarding the emplacement of Obsidian Dome, I analyzed several thin sections which represent the major products issued during effusive dome growth of Obsidian Dome (dark glassy obsidian, coarsely vesicular pumice, fine vesicular pumice, and crystalline rhyolite). After preliminary examination of the available suite of thin sections (20), I selected eight which, taken together provide a representative cross-section of Obsidian Dome. Of these eight, four were sectioned from rocks collected in the field for this study, two were from a previous study at the

University of Ottawa, (Proulx, 2007) and one (ODC-4) was sectioned from a Continental Research Drilling Program core. For reasons of brevity, only that part of the identification number in parentheses is used in subsequent discussions:

- 10-OD-(9B): Combination obsidian/finely-vesicular pumice, with a small fold
- 10-OD-(13C), 7OD-(53) and 7OD-(49): Coarsely-vesicular pumice
- 10-OD-(13D): Black, dense obsidian
- 10-OD-(16C-3): Finely-vesicular pumice
- 10-OD-(16C-2): Dense Microcrystalline rhyolite of Swanson, (1987)
- ODC4: "crystalline rhyolite" of Fink and Manley (1987)

B.2: Obsidian

The ideal obsidian would be one that is pure glass, containing no crystals of any kind. All natural obsidians deviate to various degrees from the ideal model with varying modal quantities of microlites, microphenocrysts, phenocrysts, vesicles and perhaps lythophysal and non-lithophysal spherulites. Obsidian from Obsidian Dome deviates markedly from the ideal obsidian. In thin section, black, glassy obsidian contain numerous 10-30 micron-sized microlites, ranging in abundance from 20 to 50 vol%. Microlites are typically rod or chain shaped, with the mineralogy of these likely being feldspars and pyroxenes, respectively, Figure 28 (Swanson et al., 1989). Because of the great disparity between the width and length of these microlites, they can be useful in characterizing the local flow field at the microscopic scale. The vast majority of microlites are aligned parallel to the local plane of flow banding when banding is well defined (Figure 23A). As documented, flow-bands have been deflected around metre-scale domains such as those elucidated in Chapter 3, (e.g.

Figure 21), similarly microlites are also commonly deflected around mm-sized euhedral phenocrysts (fig. 28).

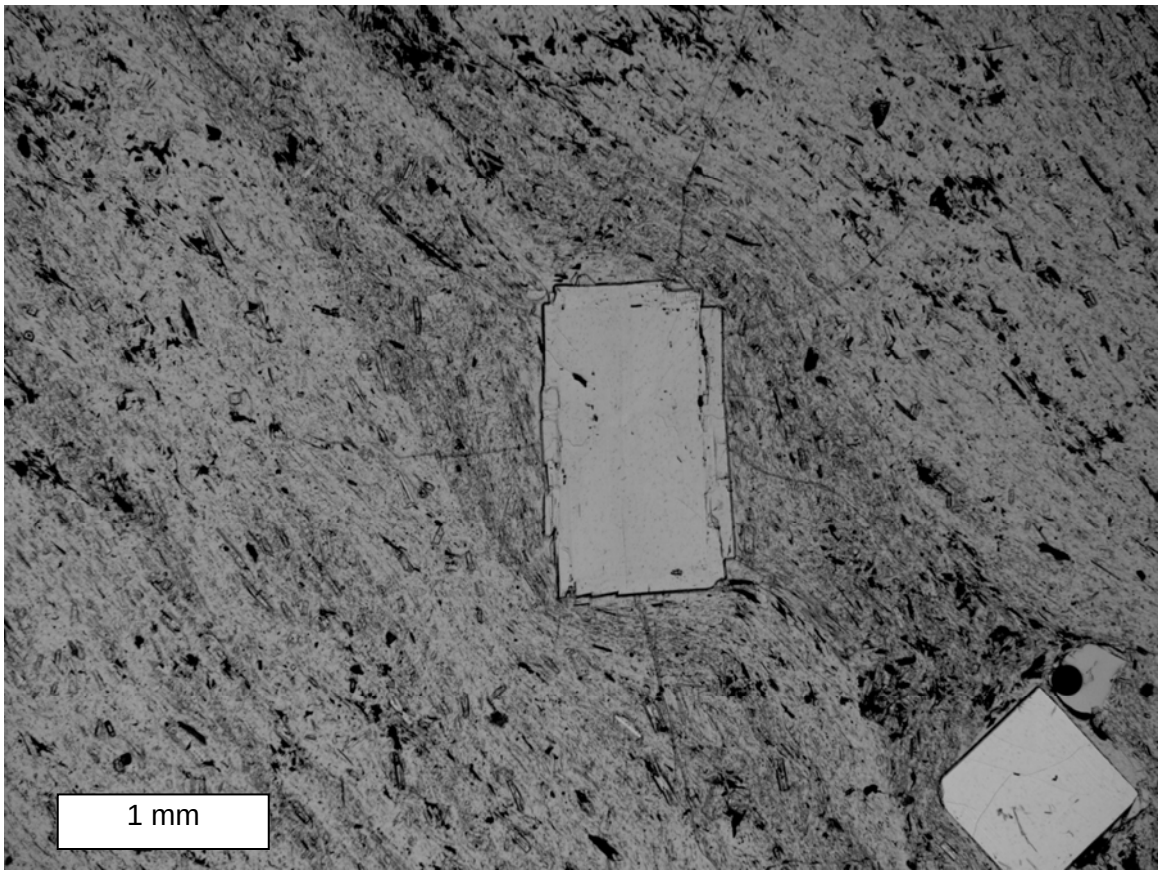

Figure 28: Plane-polar photomicrograph of thin section #13D showing microlite-defined flow banding being deflected around a plagioclase phenocryst. Note the characteristic rod- and chain-shaped microlites have been deflected around the phenocryst. Scale bar to show scale

While flow banding is a pervasive feature on Obsidian Dome, the clarity of flow banding within the obsidian component of Obsidian Dome can vary from glaringly obvious to apparently absent. Thin section 9B was made from a specimen which shows mingling between obsidian and finely-vesicular pumice, the former of which apparently has no flow banding at the macroscopic scale. However, petrographic analysis of thin section 9B, (Figure 29) reveals that even in samples of obsidian which appear homogeneous, at the macroscopic scale flow bands, defined by microlites, may be ubiquitous at the micro-scale.

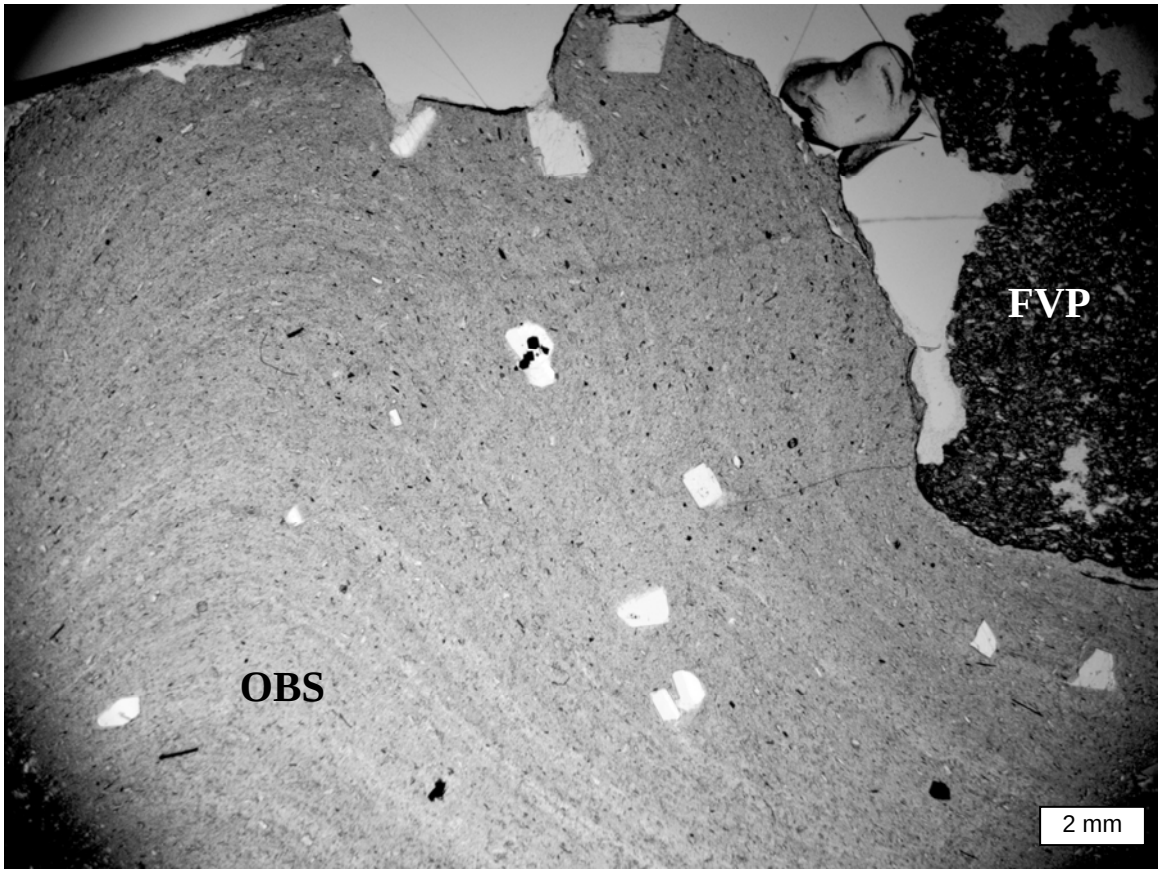

Figure 29: Plane-polar photomicrograph of thin-section #9B. OBS denotes obsidian while FVP identifies finely-vesicular pumice. Note the obvious folding in the obsidian.

B.3: Coarsely vesicular pumice

Hand samples collected during fieldwork reveal coarsely-vesicular pumice is characterized by a dense-webbing of large bubbles, imparting a frothy appearance. A chief goal in petrographically analyzing coarsely vesicular pumice is to approximate bubble size distribution and per cent void space, a task made easier using petrographic techniques. Thin section 13C was cut from a sample of coarsely vesicular pumice collected during fieldwork, while thin section #49 and 53 display the signature frothy appearance of coarsely vesicular pumice collected for a previous investigation (Proulx, 2007).

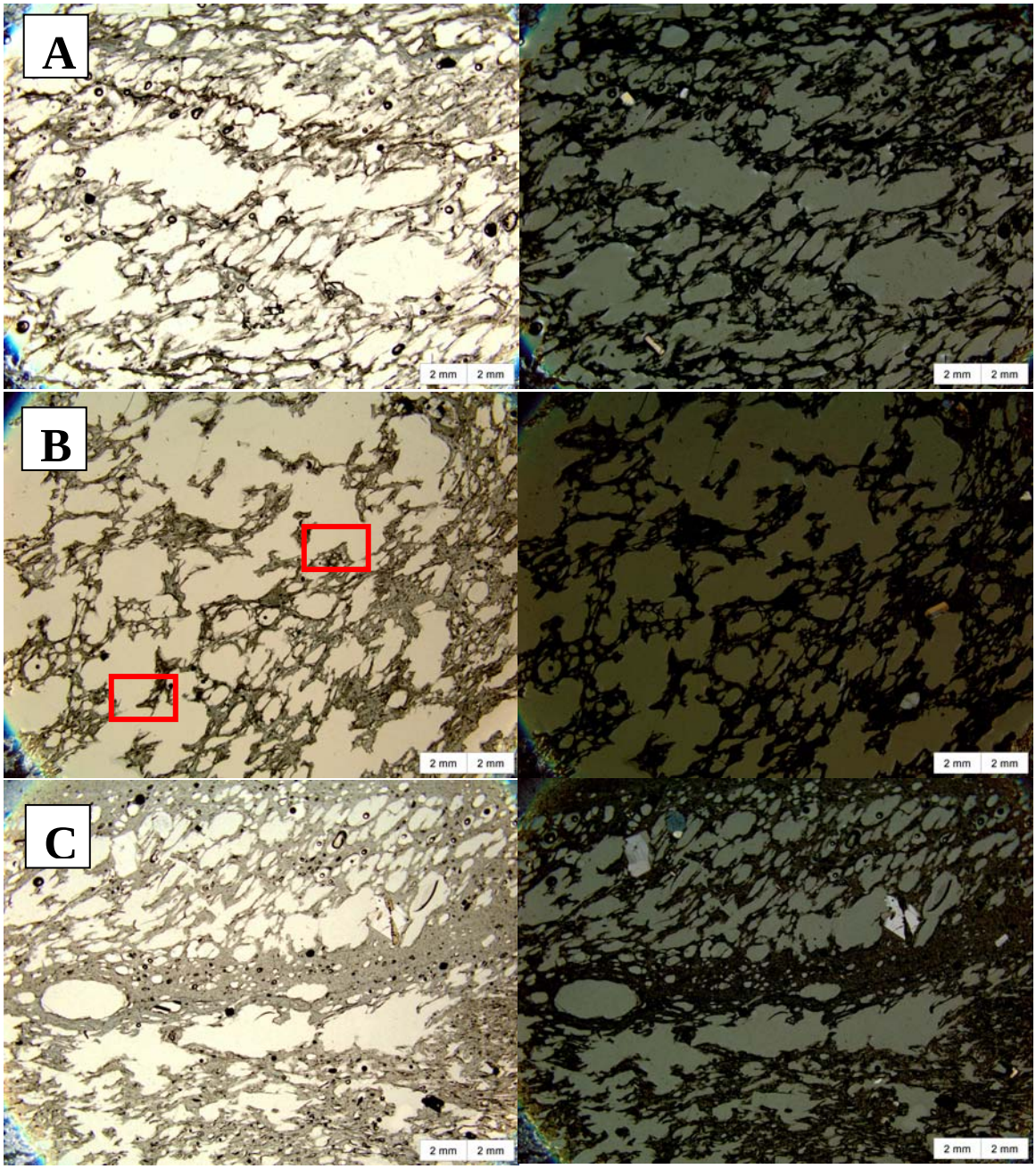

Figure 30: Photomicrographs of coarsely-vesicular pumice from three thin sections. Images on the left column were taken under plane-polar conditions while the right column are the same taken under cross-polars. Note the wide variety of bubble shapes and sizes. Key to slide identification: A, #53; B, #49 and C, #13C. The red boxes in B surround evidence of bubble-wall coalescence to be discussed briefly in the next page.

Petrographic analysis of coarsely-vesicular pumice reveal conspicuously that 40-65% of the total area is void, taken up by bubbles showing a wide range of shapes, sizes and orientations, (Fig 30). While a major constraint in analyzing patterns in thin section is the loss of depth information, since only a cross section of bubbles can be seen, I was nonetheless able to see a wide range of patterns which indicate pattern-heterogeneity in coarsely-vesicular pumice. Figure 30A, (slide #53) and the upper part of figure 30C, (slide #13C) show a series of imbricated, ovoid-shaped bubbles signifying ductile shearing during extrusion. Bubbles shown on figure 30B, (slide #49), however do not show an apparent orientation but preserve shapes that are evidence that some adjacent bubbles merged. In some cases, adjacent bubbles are cuspate, with concave-inward margins ending in a point, the geometry one expects from merged bubbles (red boxes in Fig. 30B and Fig. 31). The bottom half of figure 30C contain images of bubbles that appear to show apparent layer-parallel flattening, and exhibit irregular sharp edges, again a possible indicator of bubbles merging. Merging of the bubbles would arise during extrusion as pressure is relaxed and results in pumice inflation.

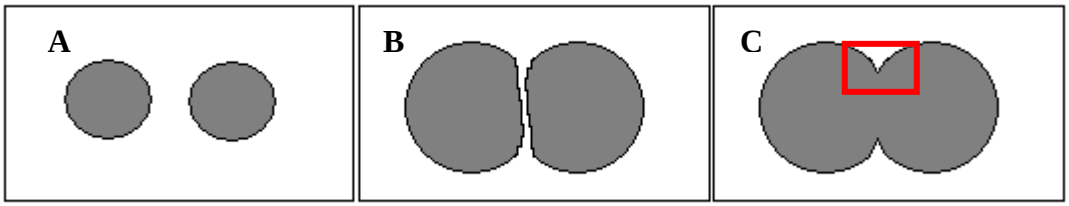

Figure 31: Schematic diagram showing the process of bubble coalescence. A: bubbles nucleate and grow adjacent to one another; B: growing adjacent bubbles impinge on one another; C: eventually merging to form one larger bubble with residual concave-inward margin points, (red box).

Bubble sizes in the coarsely vesicular pumice are quite varied. The maximum diameter of vesicles present in slides 53, 49 and 13C ranges in 2D from 1 mm through 10 mm, (Fig. 30). The majority of vesicles in the above mentioned slides, however range from 2-4 mm in size in 2D.

B.4. Finely vesicular pumice

The specimen for slide # 16C-3 was collected close to the contact between the "fine pumice" and "dense microcrystalline" regions described by Sampson (1987) at Obsidian Dome (Figures 10 and 11) and consists of a ~2 cm zone of finely vesicular pumice bounded on both sides by microcrystalline rhyolite. Slide # 16C-3, (Fig. 32) consists of a ~2 cm zone of finely vesicular pumice bounded on both sides by microcrystalline rhyolite. Excluding the bounding microcrystalline rhyolite, these vesicles comprise 40-50% of the slide area. In the course of conducting petrographic analysis of slide # 16C-3, I immediately recognized several differences between the finely vesicular pumice and the coarsely vesicular pumice described above. The first difference is, as the name suggests the size of the bubbles: rarely are the vesicles in slide 16C-3 larger than 1 mm in size, compared to the 2-4 mm sized vesicles typifying the coarsely vesicular pumice described above; secondly the size variations of the bubbles are more restricted. The third difference is in the morphology of the bubble-wall margins. Vesicles of the finely vesicular pumice are generally rounded with smooth margins (Figure 32), in stark contrast with the more jagged appearance of the bubble walls in the coarsely vesicular pumice (Figure 30). Finally, the finely vesicular pumice of slide # 16C-3 imparts, at most, a weak preferential fabric, unlike the coarsely vesicular pumice. The different morphological characteristics between the fine and coarse pumice are a reflection on the different processes which created and modified the bubbles during

extrusion. For example, the coarse pumice formed in the interior of Obsidian Dome, where heat transfer was lower, underwent shearing during advancement of the dome front.

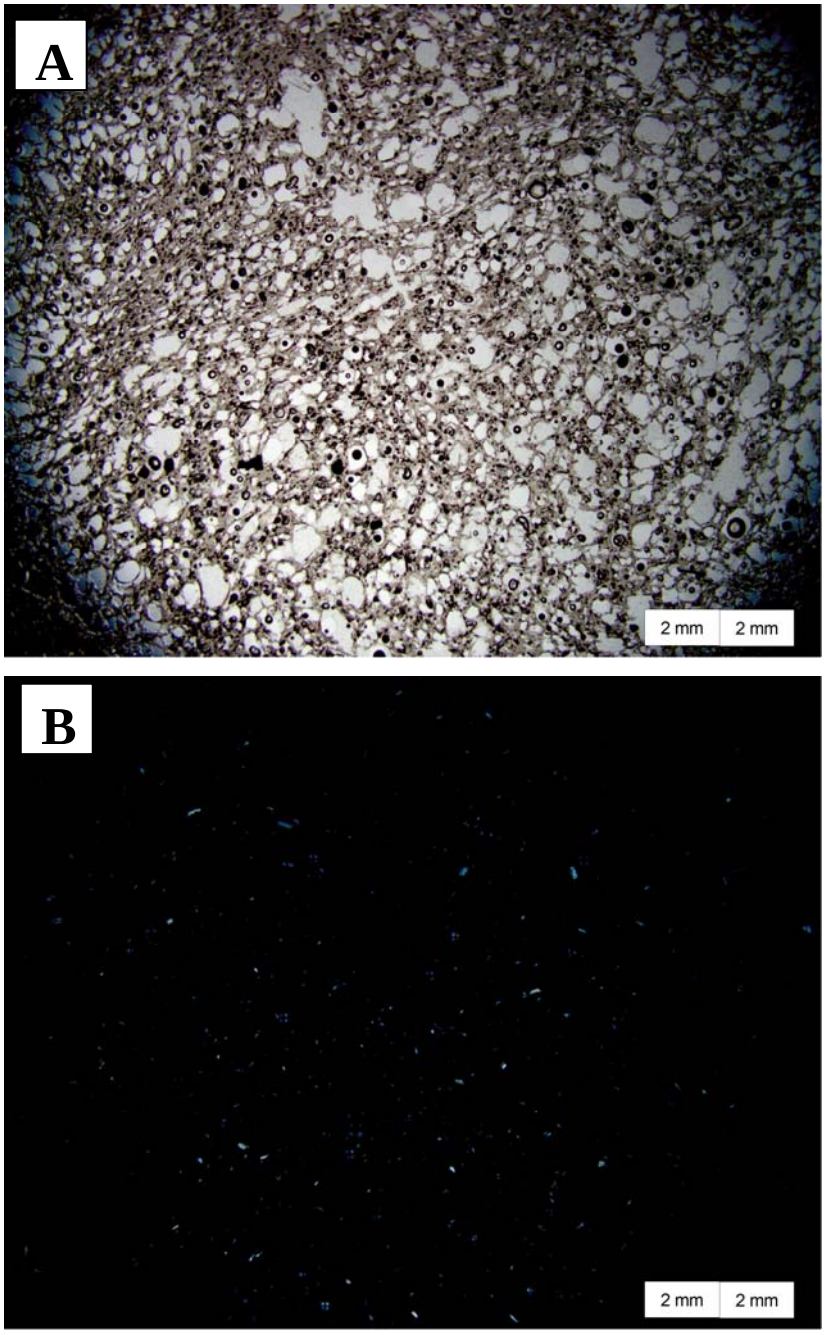

Figure 32: Photomicrographs of finely-vesicular pumice of slide #16C-3. Photomicrographs A and B are of the same area taken under plane-polar and cross-polar conditions, respectively. Note the relatively restricted size range of the bubbles and the comparatively weak structural fabric compared to some regions of the coarsely vesicular pumice shown in Figure 30. White specks in B are microphenocrysts of alkali feldspar.

B.5 Dense Microcrystalline rhyolite (of Sampson,1987)

Slide #16C-2, (Fig. 33) was sectioned from a completely microcrystalline rhyolite portion of the same rock from which slide #16C-3 was cut. 40 – 60% of the groundmass phase is composed of preferentially-aligned euhedral to subhedral microphenocryst laths of alkali feldspar. Interspersed with the alkali feldspar are highly-corroded, ferromagnesian microphenocrysts, likely fragments of corroded biotite (Fig. 33A, and discussion below).

One striking aspect of the dense-microcrystalline rhyolite as described by Sampson (1987) is the apparent lack of flow banding in thin section – this contrasts markedly from the obsidian zones of Obsidian Dome (see Fig. 29) where flow banding that is not apparent in hand sample can readily be picked out by cursory petrographic inspection. While flow banding in the obsidian is principally defined by contrasting concentrations of microlites in discrete bands, the lath-shaped microphenocrysts of alkali feldspar in the dense microcrystalline phase do not exist in such an arrangement and are fairly evenly distributed across the groundmass, though they do show preferential alignment.

Millimetre-sized, dominantly euhedral phenocrysts comprise ~10% of the total area of slide #16C-2. Like other eruptive zones on Obsidian Dome, alkali feldspars represents the dominant phenocrystic phase (Figures 33B and C). In addition to the dominant alkali feldspar, biotite and hornblende also are present in this phase. The intensity of biotite corrosion here is relatively consistent to that within the biotites of the crystalline rhyolite described by Fink and Manley (1987). Figure 33B shows a fresh, mm-sized biotite crystal that obviously escaped corrosion. Euhedral to subhedral mm-sized hornblende phenocrysts, in contrast to the biotite (Figure 33C), are generally fresh in appearance, showing no evidence of corrosion.

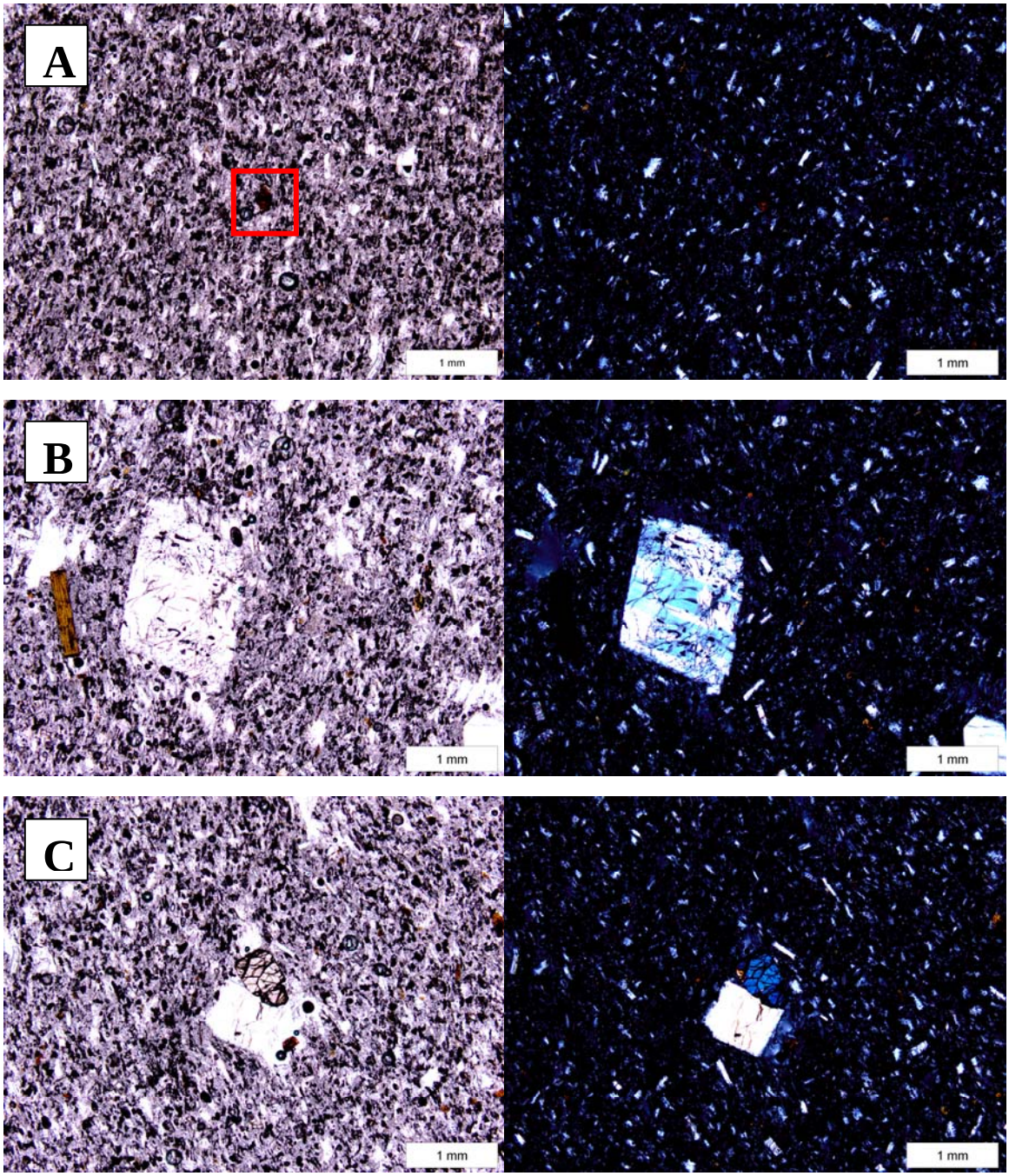

Figure 33: Photomicrographs of Dense Microcrystaline rhyolite of from slide #16-C2. Images on the left column were taken under plane-polar conditions while the right column are the same taken under cross-polars. Note that the groundmass microphenocryst laths of K-feldspar are preferentially oriented parallel to local flow. Red box in A surrounds a corroded ferromagnesian microphenocryst in. B shows phenocrysts of biotite and alkali feldspar. C show a phenocryst of hornblende impinging on a neighbouring phenocryst of alkali feldspar.

B.6. "Crystalline Rhyolite" (of Fink and Manley, 1987)

Slide # ODC-4 was taken from the 38.92 m -38.95 m interval of drill core RDO-2A from the University of Utah core library. This depth corresponds to the "crystalline rhyolite" zone of Fink and Manley (1987). Much like the obsidian zones of Obsidian Dome, the crystalline rhyolite zone is marked by well defined flow banding. In this case the flow bands consists of mm-sized, planar to weakly - undulating bands which alternate between light pinkish-brown and dark grey (Fig. 34). Light pinkish-brown bands contain 40-50% void space whereas darker grey bands contain no more than 10% void space (Fig.35). Void spaces tend to be circular in shape and show nil-to-weak bubble alignment in reference to the local direction of flow defined by the mm-scale flow banding.

Large, euhedral, mm-sized phenocrysts of dominantly alkali feldspar comprise 10-15% of the thin section whereas millimetre-sized phenocrysts of amphibole and biotite are sparse. One euhedral, mm sized phenocryst of slightly corroded biotite is present in thin section ODC4 (Figure 35C). Smaller, lath-shaped microphenocrysts, which align preferentially with local flow, account for 20-30%. Thinner bands in general are more contorted than thicker bands, having been deflected around void-spaces.

The fine textural details in the lighter pink-brown bands of slide #ODC4 displays strikingly similar characteristics to confirmed spherulites in thin section (Figure 35) in that the light pinkish-brown regions (those with more void space) tend to impart a grungy, beady characteristic. These are pinkish-coloured bands in hand sample (Figure 34). In this light, and to differentiate more conspicuously with the obviously different "dense microcrystalline rhyolite" unit of Sampson, (1987) I suggest "microspherulitic rhyolite" be thus employed.

Figure 34: Drill-core sample ODC4, of core RDO-2A, from which slide #ODC-4 was cut. Note the mm-scale flow banding between light pinkish-brown and dark grey bands and the greater abundance of void space in the lighter pinkish-brown bands.

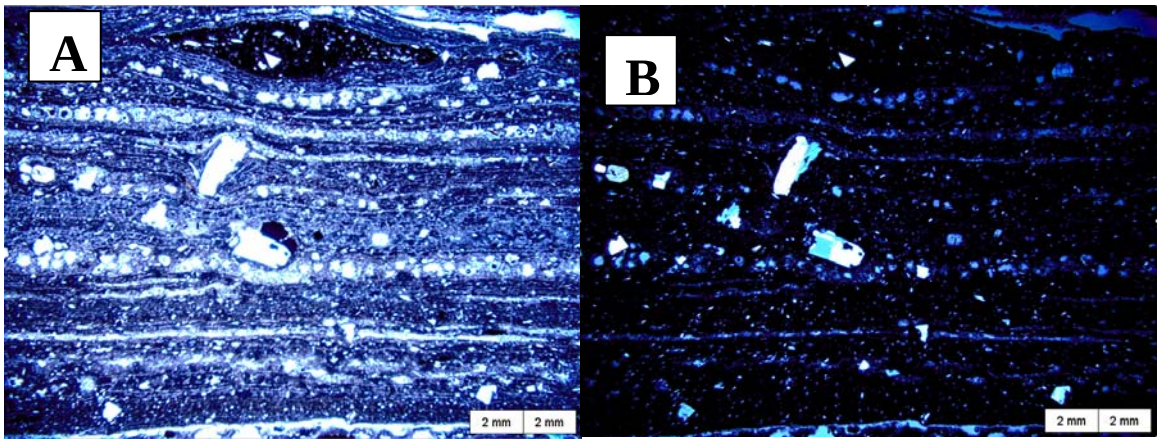

Figure 35: Full Caption next page.

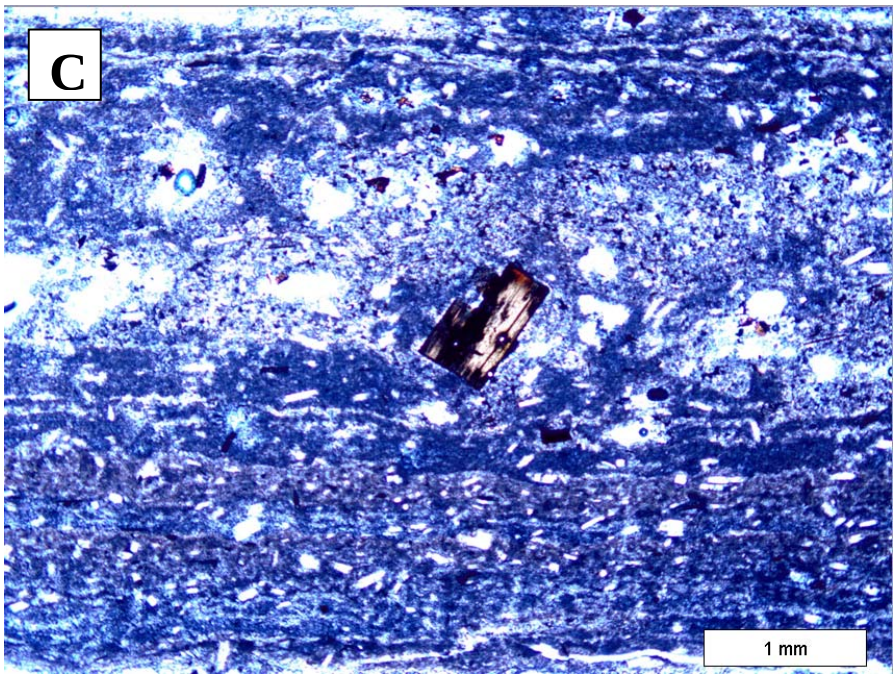

Figure 35: Photomicrographs of slide # ODC4. A (previous page): plane-polar image of a representative section showing otherwise planar flow-banding being deflected around two feldspar phenocrysts. B, (previous page): The same field of view in cross-polars. C: photomicrograph showing a corroded phenocryst of biotite. Note the overall grungy "beady" appearance in comparison to the dense-black obsidian in Figures 28 and 29.

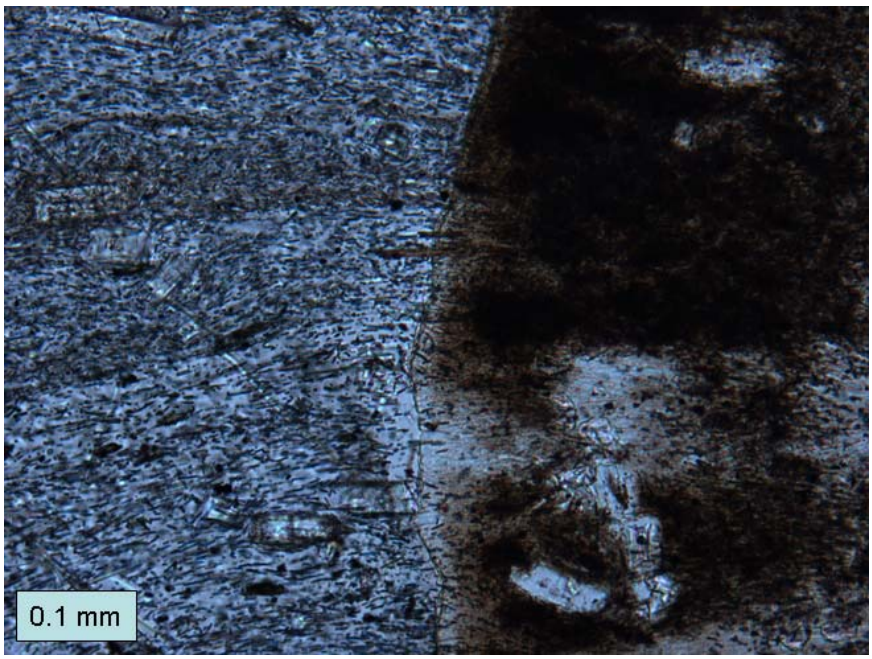

Figure 36: Example photomicrograph of a spherulite in thin section #10-OD-1A. The right side of the photograph is a spherulite while the left-hand side of the figure is the enclosing microlite-bearing glass.

C. Electron Microprobe Analysis

Quantatative geochemical analysis of Obsidian Dome rhyolites were made using a 4 spectrometer Cameca Cambax MBX microprobe at Carleton University using the wavelength dispersive x-ray method (WDX; Jones, P. written communication 2011). Operating conditions of the EMP consisted of 15 kv of accelerating potential and a beam current of 20 nA (Jones, P., written communication, 2011). Feldspar, glass and other minerals that are sensitive to the beam current were analysed using a rastered 10 x 10 – 15 x 15 micron-sized electron beam scan. Each peak analysis was computed in 15-30 seconds and accumulated ~40,000 x-ray counts. Background measurements were computed at 50% peak counting time on both sides of the peak. Once analysis was complete, raw x-ray data were converted to elemental weight per cents using the Cameca PAP matrix correction program. Natural and synthetic minerals and compounds served as calibration standard for each element analysed (provided in Appendix II; Jones, P. written communication, 2011).

EMP analyses of glasses (data in Appendix 3) from thin sections 1A and 13D place the eruptive products of Obsidian Dome firmly in the rhyolite field of LeBas and others (1986) (Figure 37). The silica values generated for this study are comparable to the data Swanson reports in his Figure 7, ranging from 73 to 76 wt% SiO2, though he reports a more restricted range from 73 – 74 wt% SiO2 (1987). If the geochemical signature gleaned from analyzing thin sections 1A and 13D are to be considered representative of the entire extrusion, then from the perspective of the Total Alkali-Silica analysis the eruption produced chemically homogeneous lavas. Although Sampson (1987) has shown that textural heterogeneity arises from magma mixing between fine and coarsely porphyritic lavas in the southern two domes (Glass Creek and Deadman Creek), detailed cm-dm scale isotopic analysis by Proloux (2007) from Obsidian Dome revealed that minor variations in Rb and Sr

are due chiefly to fractionation and that flow banding is not due to mingling of discrete lavas.

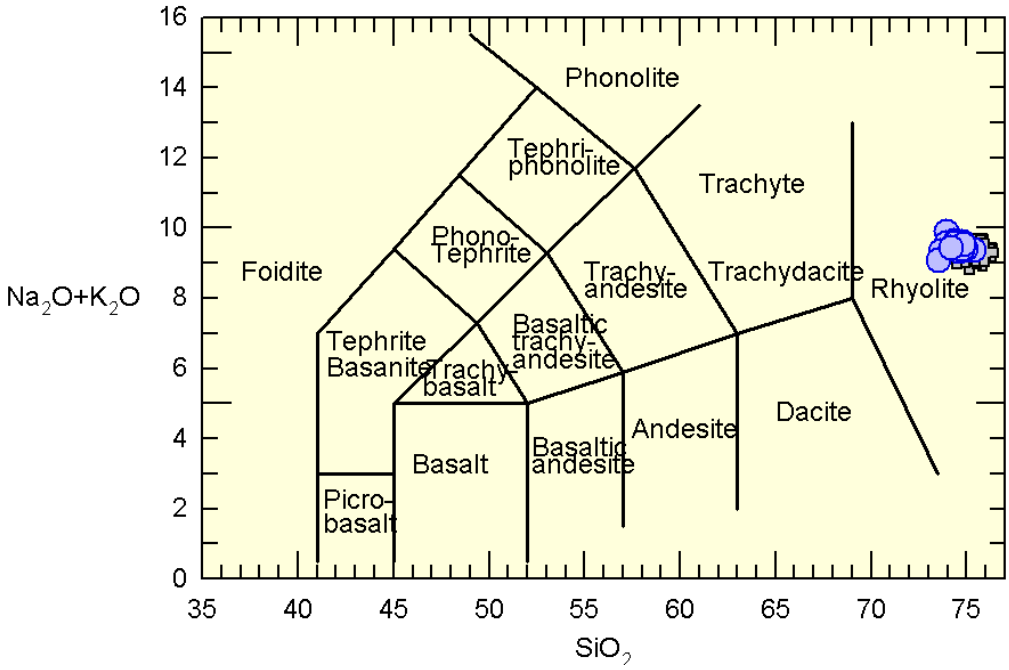

Figure 37: Total Alkali-Silica plot of 44 EMP analyses of glasses. Blue circles are data from slide 10-OD-1A while grey crosses denote thin section 10-OD-13E Name conventions and divisions from LeBas and others, (1986).

A major constituent of Obsidian Dome rhyolites are phenocrysts and microphenocrysts of alkalic feldspar. Although there is some plagioclase (An_{20}) more calcic than albite, the majority have less than 10% An and populate space between Or_{30} and Or_{60}, (Figure 38) therefore the term "alkali feldspar" is adopted for this thesis. Reconnaissance petrographic analysis show that in both of these populations, chemical zoning is weak to non-existent. Microprobe data obtained for this study appear to confirm the lack of a strongly zoned set of microphenocrysts shown in figure 38A. Figure 38B represents 8 chemical

analyses of 4 phenocrysts taken from slide #13E. While it is tenuous to extrapolate to an entire population based upon analysis of four phenocrysts, each phenocryst centre is K-depleted (Or_{10}) relative to the majority of analyzed microphenocrysts ($Or_{30} – Or_{60}$). Three of four phenocryst rims are also more albite rich than the bulk of the measured microphenocrysts. The one anomaly is in phenocryst 4 (Fig. 39D) where recalculations reveal a rim enriched in K.

Figure 40 shows a sample of five microphenocrysts from thin section #13E which were chemically analyzed by electron microprobe. This figure partially reproduces data from Figure 38A; however, here I show intra-microphenocryst compositional variations. Results from this suite of data show there are varying patterns between the composition of cores and rims of the target microphenocryst. In microphenocrysts 2, 4 and 5, the cores were significantly more K-rich relative to the rims. While the microprobe data for microphenocryst 1 appears to show little in terms of compositional variation, the associated BSE image clearly show zonation, with rims showing enrichment in K relative to the cores. Though the very "core" of microphenocryst 3 appears likely to be void space and taken up by rhyolite glass, much of microphenocryst 3 in BSE image look remarkably homogenous (with the exception of the bottom of the crystal which, due to the darker colour, would mean depletion of K).

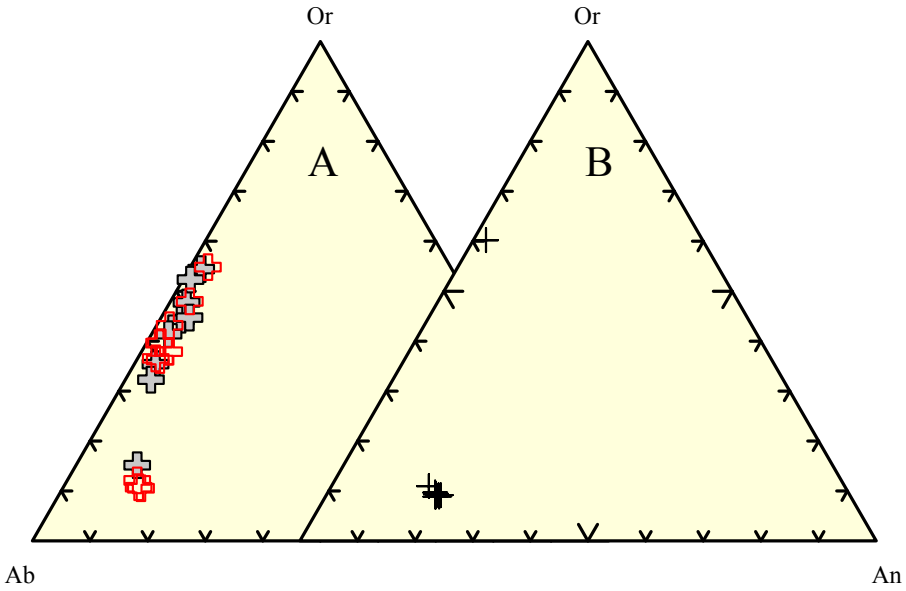

Figure 38: Stacked ternary plot of two distinct feldspar populations based on a recalculation of electron micro-probe geochemical data. A: 20 analyses of 10 microphenocryst feldspar crystals from thin sections 10-OD-1A and 10-OD-13E. Red, open crosses are recalculations of microphenocryst rims, whereas grey, filled crosses denote recalculations of microphenocryst cores. B: 8 analyses of 4 phenocrysts present in slide 10-OD-13E. Note that, in general, the microphenocrysts are more orthoclase-rich compared to he phenocrysts.

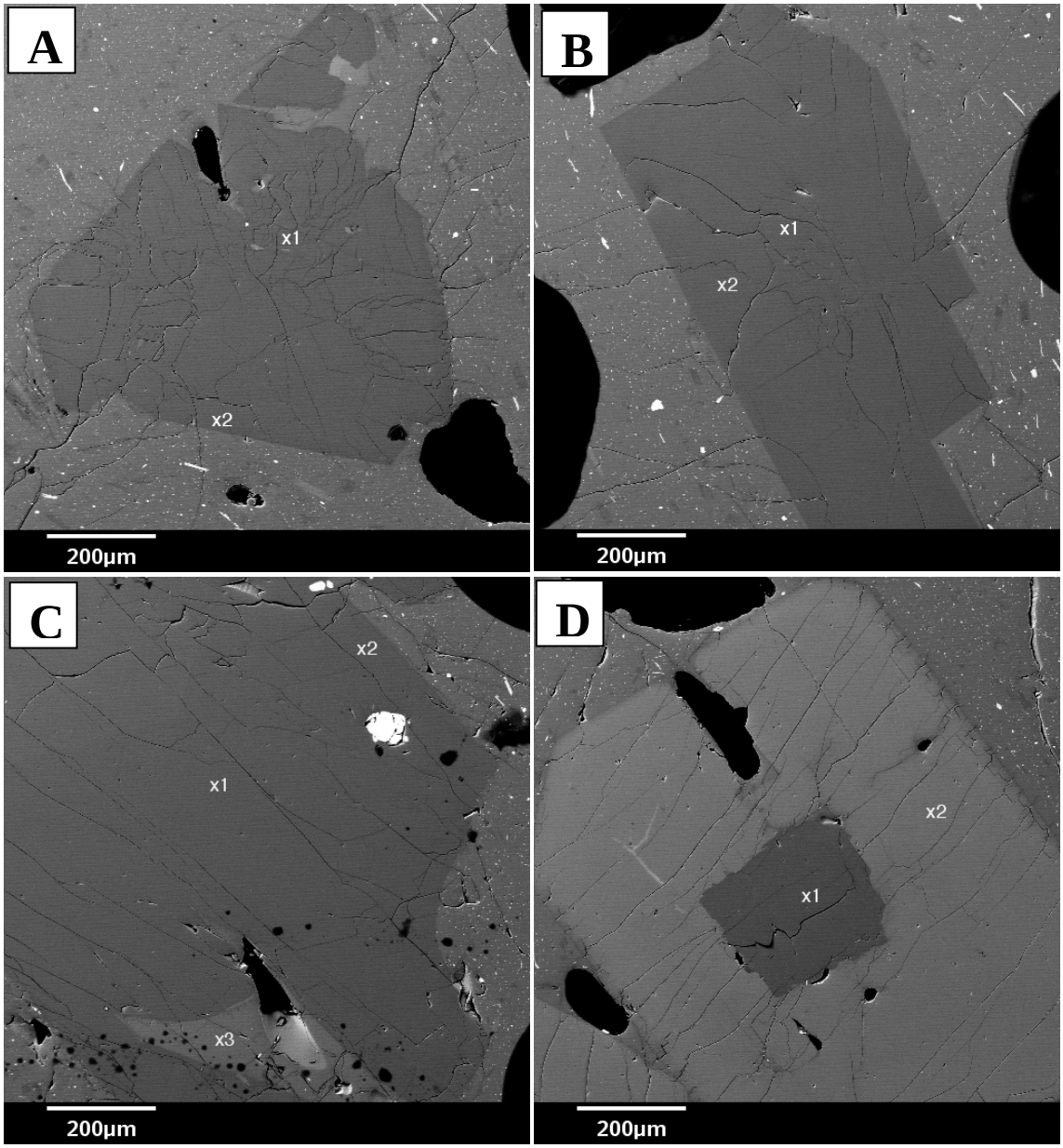

Figure 39: Scanning electron microphotographs of the four analysed phenocrysts of alkali feldspar. "x" represent the locations of chemical analysis used for this study. A, B, C, and D represent phenocrysts 1, 2, 3, and 4, respectively. Chemical analysis from the third point in the bottom of phenocryst 3 has been removed from the feldspar analysis since it is likely glass. Scale bar in lower left of each image to show scale.

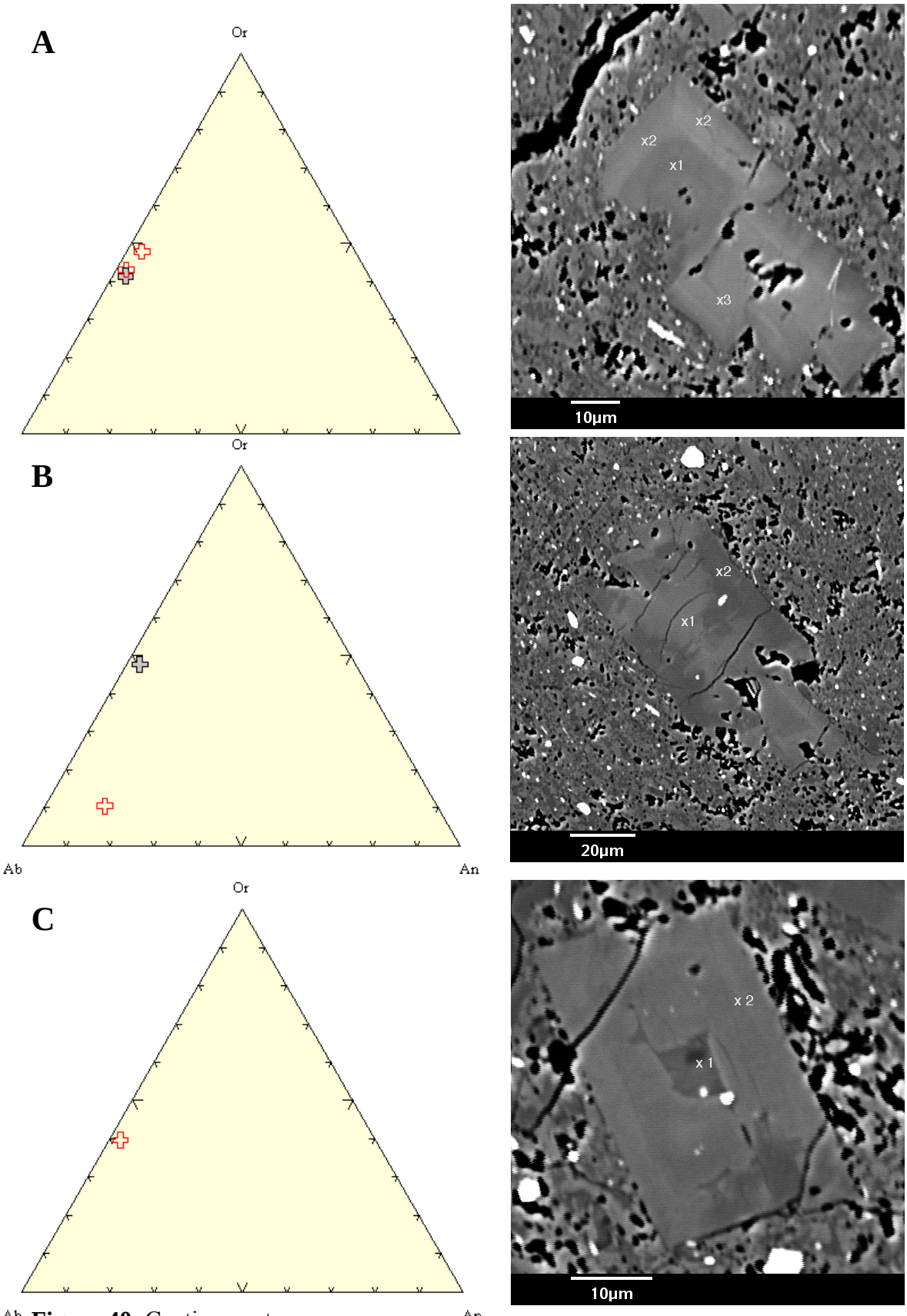

Figure 40: Caption next page

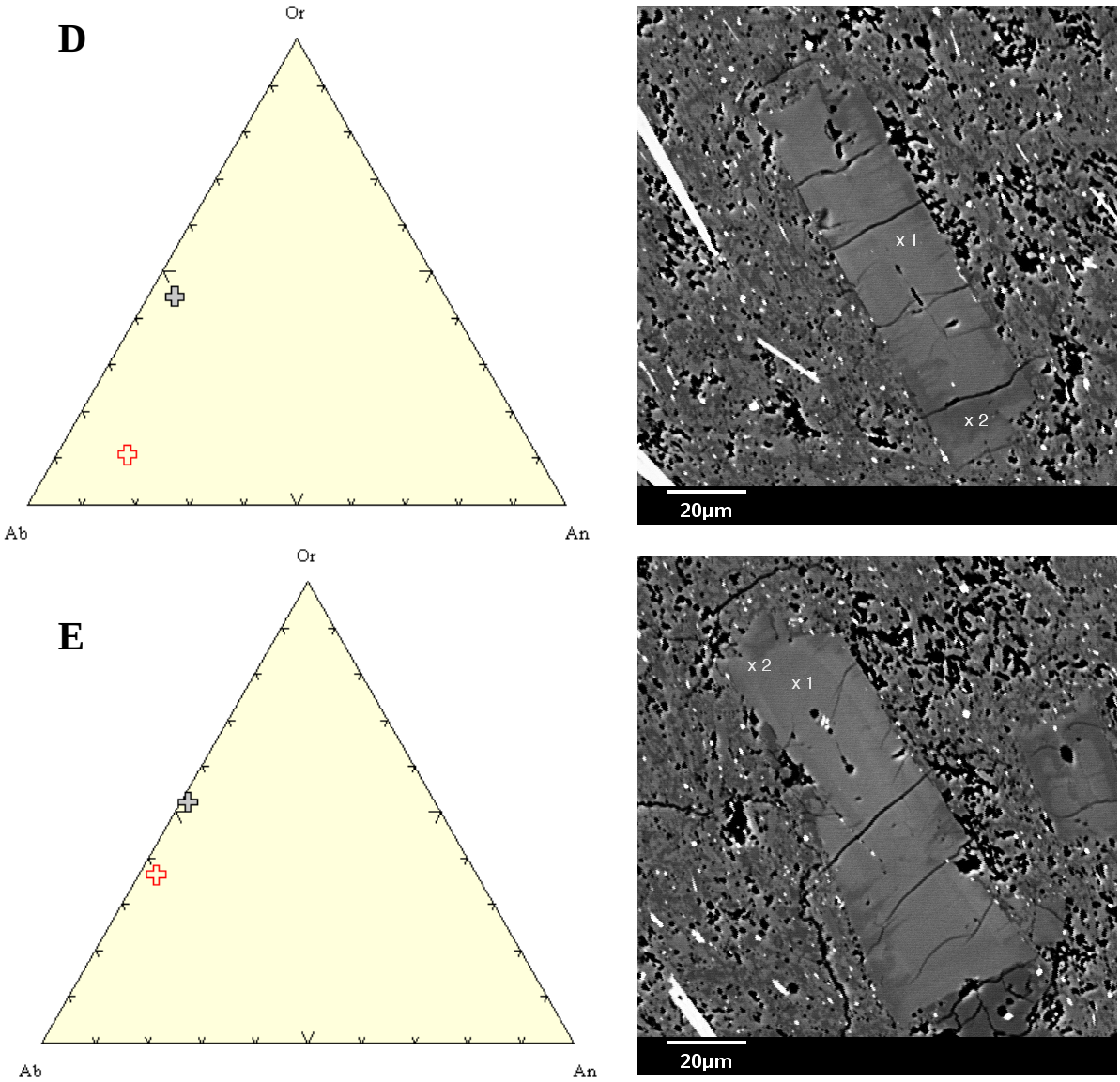

Figure 40: Microphenocryst compositional diagrams (left column) and the associated B.S.E. image of each microphenocryst alkali feldspar targeted for analysis (right column). The "x" marks locations selected for chemical analysis. A, B, C, D and E correspond to microphenocrysts 1, 2, 3, 4 and 5 respectively. Red, open crosses represent chemical recalculations of microphenocryst rims, whereas grey, filled crosses denote the same for microphenocryst cores. The "core" of microphenocryst 3 chemically was indistinguishable from glass, and not consistent with expected chemical norms for feldspar; thus point #1 was likely taken in a central void and is thus rejected and not reported in the associated ternary diagram. The two rim data points for microphenocryst 1 are from the duplicate point #2.

D. Spherulite Mineralogy X-Ray Diffraction

Because spherulites are so fine grained, I performed reconnaissance-level powder X-Ray Diffraction (PXRD) analysis to characterize them. Analysis was performed at the University of Ottawa using a Rigaku Ultima IV X-Ray Diffractometer. The analytical procedure used involved meticulous picking at a spherulite with an X-acto knife over a sample paper, ensuring that no stray rhyolitic glass or foreign substance would be included to contaminate analytical results. The volume of the broken-off sample I estimate was approximately 1-3 mm^3. With a thoroughly cleaned mortar and pestle, I proceeded to grind up the sample to a fine powder, and then placed the powder into the PXRD holder, ensuring the powdered-sample covers the entire detection surface area on the slide and the top surface was flat. Using the continuous scan mode, I scanned from 18 – 80 degrees at a scanning rate of 0.25 degrees per minute using the 2theta/theta scanning axis.

Previous work on spherulites (e.g Lofgren, 1971) has shown that the mineralogy thereof is principally feldspar (K-feldspar and plagioclase) as well as quartz (or a high-T polymorph) that may vary in proportion both within a single flow and between flows. My data for this study confirms these findings. Figure 41 displays XRD data from a spherulite taken from the 25.6 m level of drill core RDO-2A (sample ODC-2) placing it within the upper spherulite zone of Fink and Manley (1987). Comparing the peaks from this sample against peak data from the database to first order, I have determined that the peak set from high β crystobalite and a synthetic orthoclase most closely matches data gleaned from ODC-2.

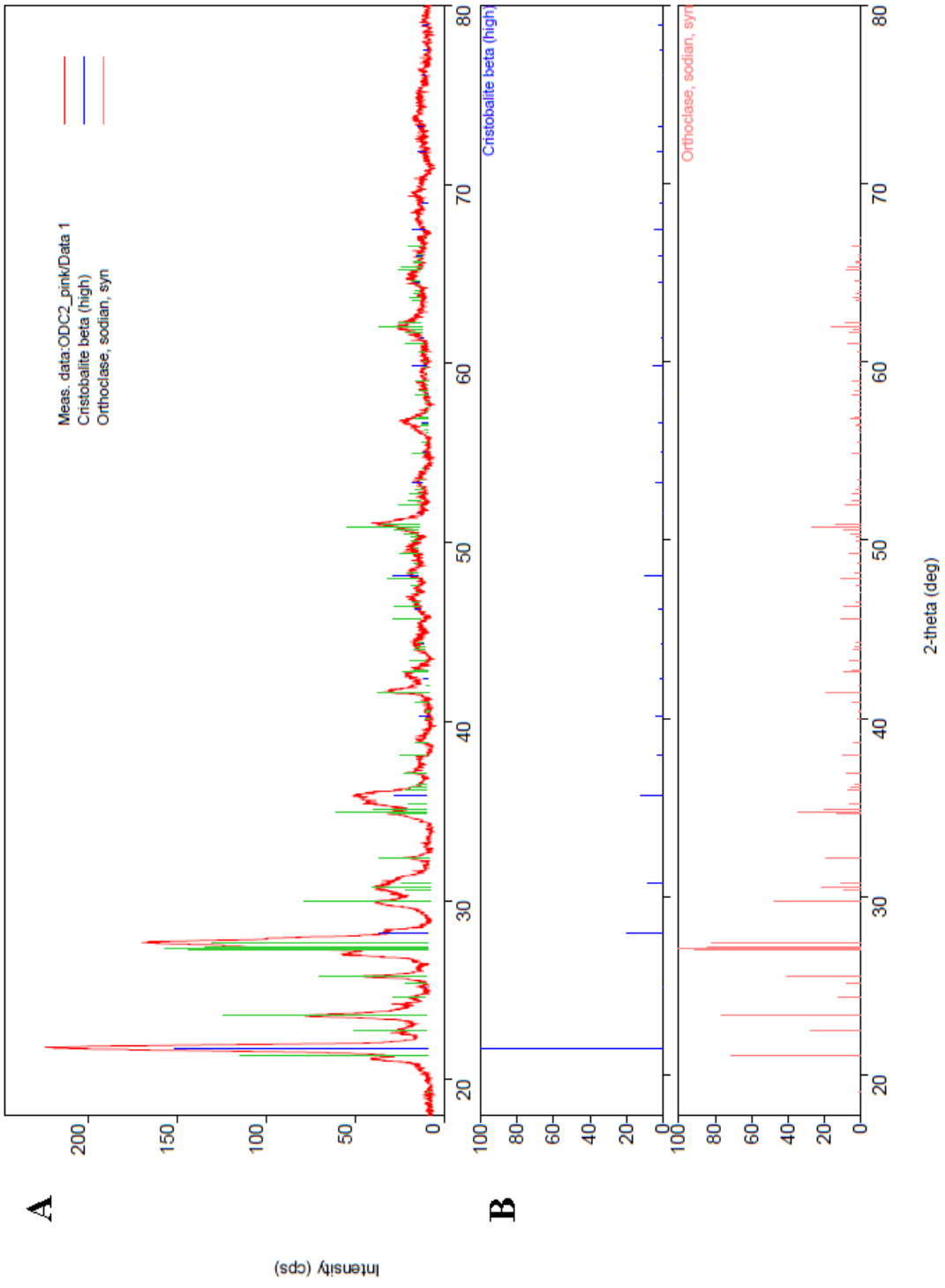

Figure 41: Powdered X-Ray Diffraction plot for spherulite in sample ODC-2. A: Intensity plot showing (in red) the measured peak intensity data against database-provided peak values for β-crystobalite (blue) and synthetic orthoclase (green). B: database-provided intensity values presented as individual plots with β-crystobalite in blue and synthetic orthoclase in orange.

E. Chapter Discussion and Summary

Petrographic analysis of thin sections cut from samples of Obsidian Dome reveal that the complexities of flow features viewed in the field extend downward into the microscopic realm. In the obsidian and the microspherulitic rhyolite (my terminology) phases of Obsidian Dome, flow banding manifests itself along a continuum from planar to folded, and deflection around phenocrystic obstacles (e.g. Fig. 28) are widespread manifestations of the complex micro-scale features that together comprise Obsidian Dome.

Based upon my review of the literature (e.g. Fink and Manley, 1987, Sampson, 1987) as well as my own observations, I surmise that "microspherulitic rhyolite" would be a better moniker to describe that zone to which Fink and Manley, (1987) call "crystalline rhyolite." As previously described in section B.5, Slide #ODC-4, was taken from a unit Fink and Manley (1987) classify as "crystalline rhyolite." Even though spherulites are *sensu stricto* a type of crystal, the unusual physical characteristics of this interior zone – bands defined by microspherulites -- when compared to the other eruptive phases that exist on Obsidian Dome, leads me to conclude that the name chosen by Fink and Manley (1987) doesn't fully represent this unit. Additionally, reclassification from "crystalline rhyolite" to "microspherulitic rhyolite" would reduce potential confusion with the similarly-sounding, but obviously different "dense microcrystalline rhyolite" of Sampson (1987).

In his Table 1, Sampson (1987) provides a comparison between the physical characteristics of the various eruptive units in the Inyo Craters array. In this table, he outlines the various differences between the finely vesicular pumice and the coarsely-vesicular pumice. While my own independent observations of both pumice units confirm broadly with Sampson's findings (1987), I observed that most bubble wall margins of the finely-vesicular

pumice unit are smooth and cuspate (Fig.32), while those of the vesicles of the coarsely vesicular phase were quite commonly jagged (Fig. 30). While it is hard to extrapolate and make global conclusions based upon one thin section of finely vesicular pumice, what I saw in thin section #16C-3 contradicts with what Sampson (1987) indicated in his table 1, considering that nowhere are photomicrographs included to verify his statement.

Chapter 5: Discussion and Conclusions:

A. Discussion

Obsidian Dome is among the youngest volcanic features in a region with a legacy of diverse volcanic activity that transcend space, time and geologic impact to the land during the last ~4 Ma. Just about every conceivable Quaternary and late Tertiary subaerial volcanic landform is represented in the Mono Basin-Long Valley Region except the large composite cones typical of volcanic arcs. Because Obsidian Dome erupted in a semi-arid environment where rates of soil development are much reduced, many structural and flow features that define the lava dome remain remarkably intact. The climate, coupled with the relative youth of Obsidian Dome, provided an ideal field laboratory from which to document many features which aid in providing insight into the overall manner in which Obsidian Dome – and by extension nearly all high-silica rhyolite lava domes – effuse onto the surface. Accordingly, a discussion on the model of emplacement of Obsidian Dome follows.

As discussed in Chapter 3, two broad families of structures exist on obsidian dome: ductile features which record relaxed flow above the glass transition, and brittle failure structures that record un-relaxed deformation. In a very simplistic sense, as an extrusion of lava cools throughout time, ductile flow features (e.g. folding, flow band deflection) give rise to structures which record brittle failure (e.g. faulting, various styles of fracturing). However, global geologic concepts (in this case ductile yields to brittle failure over time) sometimes break down at the local level as I have observed in the field. This aforementioned concept is clearly demonstrated in Figures 23A and 23B, where we see ductile drooping of dense

rhyolite over cracks in coarsely vesicular pumice, (Figure 23A) and inflationary, bulbous bands of rhyolite squeezing out from faulted rock (Figure 23B).

A central goal of this work is to arrive at a model as to how Obsidian Dome was extruded onto the surface based upon field and laboratory analysis of the eruptive products. The magma reservoir from which the lavas of Obsidian Dome were sourced contained two distinct magmas: a high-Ba, low silica magma and a low-Ba high silica end member (Vogel et al, 1989) (Figure 6). These end-members mingled in the magma chamber and could have provided the "spark" that allowed rhyolitic magma to begin its ascent to the surface (Vogel et. al., 1985) 550-650 years ago (Miller, 1985) (Figure 42A).

The subsequent dike propagation, upon reaching the surface initiated a series of magmatic and phreatic explosions that deposited ~0.2 km^3 of pyroclastic material over more than 140 km^2 (Miller, 1985) (Figure 42B-C). Miller (1985) hypothesized that Obsidian Dome, together with the domes of Glass Creek and Deadman Creek to the south, essentially erupted contemporaneously with one another. During this explosive phase, the dominant products deposited proximal to the dome were unconsolidated coarse ash- and lapilli-sized juvenile tephra intermixed with lithic fragments that were concentrated on the northeast side of the dome where much of the airfall was directed by the wind (Miller, 1985).

After the initial explosive phase of eruptive activity waned, that presumably evacuated volatile-charged rhyolite, a dome began to emerge from a conduit system likely through the repetition of fracture and subsequent annealing of comparatively degassed rhyolite (Figure 42D). During the ascent of the magma through the dike, temperatures remained between 910-950°C based upon the preponderance of Fe-Ti oxide thermometric measurements from Vogel and others (1989). Beginning in the vent area during initial emergence of the dome, much of the shear stress associated with emplacement was

dominated by pure shear flow regimes as a result of lateral spread from the vent area, (e.g. Castro, 2002). As the rhyolite lava flowed further from the dome, lateral spread gave way to gravity driven flow and the result thereof is a gradual increase in the amount of simple shear overprinting, similar to what Iezzi and Ventura (2005) observed on Porri volcano in Italy.

During active flow, two distinct types of pumice were formed: on the top of the dome carapace, finely vesicular pumice was formed due to the effervescence of volatiles whereas coarsely vesicular pumice was created above the microspherulitic rhyolite (my terminology) as volatiles were removed and subsequently migrated upward through fractures in obsidian during crystallization of the microspherulitic rhyolite (e.g. Fink and Manley, 1987) (Figure 42E).

Despite the, local ubiquitous presence of spherulites in the interior of Obsidian Dome (and similar extrusions in the intermountain west) very little work has been done to elucidate their contribution to the overall eruptive dynamics. Research completed to date has focused on the conditions required to produce different shapes of spherulites (e.g. Lofgren, 1971a; Lofgren, 1971b) as well as spherulite growth during 'devitrification' (Swanson et al., 1989). Spherulites display a wide array of shapes and sizes that reflect the conditions of formation (Lofgren, 1971a; Lofgren 1971b Swanson et al., 1989). Lofgren (1971b) experimented with alkali solution-enhanced natural rhyolite glass, and from it, produced circular-shaped spherulites in runs as low as 400°C, bow-tie-shaped spherulites between 400°C and 600°C, and above 600°C spherulite fibres tended to be lath shaped.

Swanson and others (1989) classify Obsidian Dome spherulites as devitrification textures yet in their discussion on lithophysal spherulites they indicate that deformation of the surrounding host material is a prerequisite for producing lithophysae. If this is the case, then in order to crystallize lithophysal spherulites, the host material must be able to deform

plastically – i.e. it must be above the glass transition as I have documented. Thus, lithophysal spherulites cannot be the result of devitrification due to the fact they crystallize above the glass transition (e.g. Lofgren, 1971; McPhie et al., 1993). Indeed, during my investigation of spherulites both in the field and in core samples, I find no compelling field evidence that leads me to conclude that spherulite crystallization occured below the glass transition.

While Obsidian Dome is not entirely composed of rhyolite glass (as the geographic moniker might so imply), rhyolite glass is still quite ubiquitous along its margins as well as its interior as evident from coring (Figure 8A). A major objective of this thesis is to address why glass exists in such large volumes in comparison to what thermodynamics might imply. As elucidated in Chapter 2, section F, two hypotheses have been advanced in order to explain the large quantities of rhyolitic glass at Obsidian dome and other similar structures: that glass results in collapse of a "permeable foam" (Eichelberger et al., 1986; Eichelberger, 1989) or that the glass is a primary feature in a "volatile stratified" system, (Fink and Manley, 1987; Fink et al., 1992). Essentially both models rely upon loss of gas to increase the viscosity, thereby decreasing diffusivities impeding crystal nucleation and growth and stiffening the melt.

Based upon the available field evidence (pyroclasts, extensive flow banding, autoclastic breccia), coupled with laboratory analysis of thin sections (no relict bubble walls), I find it unlikely that a large batch of rhyolite melt rose to the surface *exclusively* as a "permeable foam," regions of which collapsed by gas loss, to form obsidian as invoked by Eichelberger and others (1986). The viscosity of rhyolite and the observed metre-scale exposures of homogeneous obsidian on the dome margins (Figures 12A, 13-15) and interior (Figure 8A) precludes such large-scale bubble-wall collapse. Furthermore, because the autoclastic breccia is heavily oxidized, likely due to gas escape and mixing with atmosphere

at high temperature, one would expect that if the entire dome was initially a foam that it would show significantly more evidence of oxidation. In localized areas of the coarsely vesicular pumice, intense shearing during active flow would have promoted complete bubble-flattening (i.e. if the shearing had continued deforming the imbricate bubbles in Figure 30A and the top half of Figure 30C). However, this process would likely leave vestigial bubble traces perceptible in thin section of glass, (cf. Figures 28 and 29). Furthermore, if Obsidian Dome extruded initially as a "soufflé", then one would expect the erupting lava dome to have been structurally unstable at the vent as it would have to have attained a height significantly higher than the present day central high in order to create enough pressure to collapse the purported foam. It is difficult to imagine that the elevated foam would collapse back onto itself rather than "spill over" to make a more irregular dome margin. Moreover, the folds and fractures I have observed could not have first formed in foam.

Fink and others (1992) provide a more logical explanation as to the presence of large volumes of glass at Obsidian Dome and other rhyolite extrusions in the intermountain west. Their "volatile stratification" model holds that much of the volatiles involved in the eruptive sequence were expelled early during the explosive phase of activity and that obsidian is a *primary* product of largely degassed dome effusion, (Fink et al., 1992). Evidence to the primary origin of obsidian glass include the vesiculation of glass during extrusion (e.g. the coarsely vesicular pumice forming as a result of upward migration of expelled volatiles during crystallization of the microspherulitic rhyolite) and the presence of obsidian on extremely small domes, (Fink and Manley, 1987; Fink et al., 1992). My work shows that there have been several factors that promoted gas loss: (1) formation of pumice by

vesiculation, repeated fracturing of the “melt” and (3) there were more than one episode of explosive activity, (e.g. Figure 26).

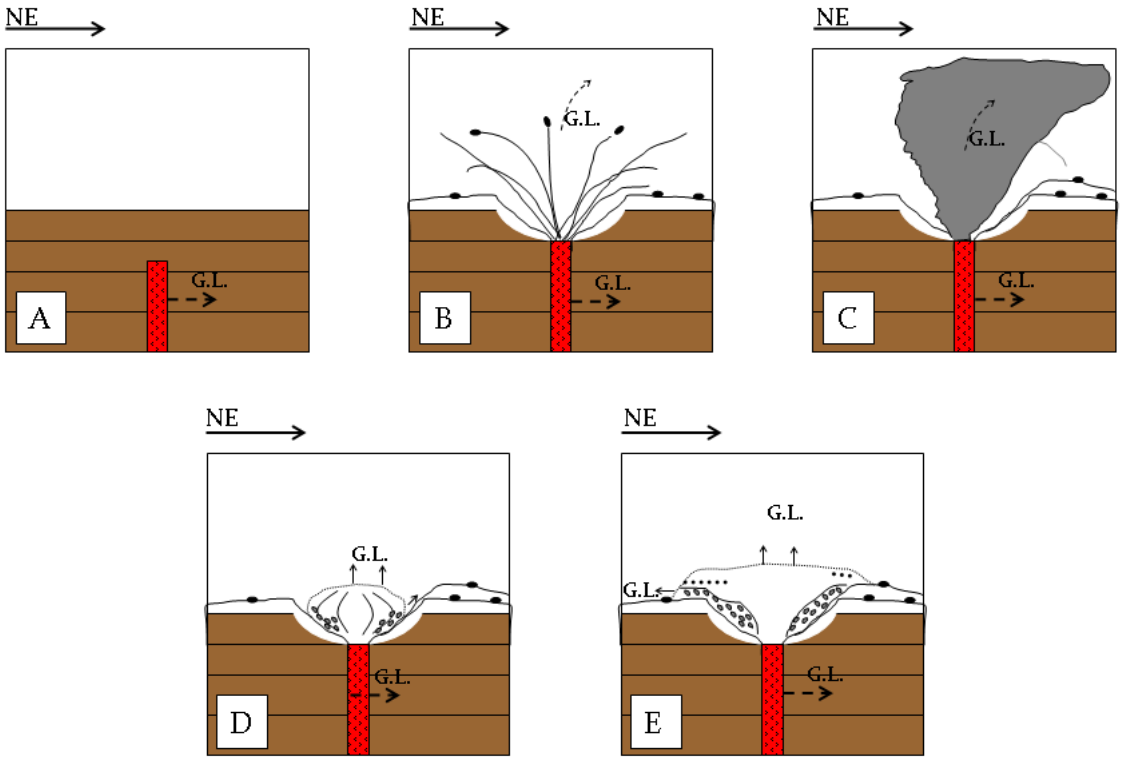

Figure 42: Cartoon diagram showing the emplacement history of Obsidian Dome based upon my model of dome growth. A: Initial propagation of rhyolite dike with initial gas loss (GL) to the country rock through fractures. B: Major gas loss event through initial phreatic explosions upon the dike ascending the surface. C: Explosions continue, with the addition of juvenile pyroclasts and bombs. D: Initial emergence of Obsidian Dome from the vent area. The dome carapace, shown here as a stippled line, represents finely vesicular pumice. The irregularly shaped blocks at the base of the dome represent autoclastic breccia E: Continued growth of Obsidian Dome overflows the explosion pit. Coarsely vesicular pumice, shown as aligned dots in the distal reaches of Obsidian Dome, form as a result of upward migration of gasses expelled from the crystallizing microspherulitic rhyolite interior (e.g. Fink et al., 1992) (not shown due to space constraints).

B. Conclusion

The principal motivation in embarking on this thesis project was to interpret the eruptive history of Obsidian Dome based on the physical properties of highly polymerized rhyolite melt and detailed documentation of the eruptive features. In conjunction with elucidating eruptive history and physical properties, I also compared two widely divergent models for the extrusion of Obsidian Dome – and by extension the Inyo Chain array –based on an independent analysis of structural and flow features of Obsidian Dome. On the one hand, Taylor and others (1983) contend that, based on isotopic analysis, Obsidian Dome extruded onto the surface as a "permeable foam" that subsequently collapsed during supra-surface degassing.

An alternative model for the extrusion of Obsidian Dome, dubbed the "volatile stratification" model holds that most of the gasses escaped during the initial explosive phase of eruption leaving comparatively gas-poor, late-stage rhyolite to extrude onto the surface (Friedman, 1989; Fink et al., 1992). Based upon my field observations, I can reasonably conclude that:

1. While the overall deformation progression during effusion is ductile, followed by brittle regimes, I have documented evidence that in localized areas, owing to the way coupling of stress with the glass transition effects deformation styles at varying timescales and temperatures, of repeated generations of ductile and brittle deformation regimes during flow.
2. In line with the work of others elsewhere (e.g. Tuffen and Dingwell, 2005 in Iceland) this work shows that brittle failure of the "melt" may have been annealed. Such fractures may have provided pathways for significant gas loss, thus increasing glass formation over pumice.

3. Volatiles were lost during the pyroclastic phase during effusion of pumice and through autoclastic brecciation. Moreover, field evidence show that there was more than one explosive event.
4. There is no evidence that the entire edifice formed as a "soufflé" and then collapsed. Clearly features of the dome (e.g. autoclastic breccia, flow-banding, pyroclasts) show it was extruded *sensu stricto* as a foam.
5. Thick amounts of obsidian form unlike, (for example) basalt because rhyolite is very viscous meaning that diffusion and crystal growth are sluggish. This combined with the stiffening affect of volatile loss accounts for the large volumes of glass at Obsidian Dome.
6. No spherulites that I document here show evidence of being devitrification features.

"And this is why Obsidian Dome (e.g. 'my baby') Rocks!"

References

Anderson, S.W. and Fink, J.H.,1992. Crease structures: Indicators of emplacement rates and surface stress regimes of lava flows. Geological Society of America Bulletin 104(5): 615-625.

Andrews, G.D.M. and Branney, M.J., 2011. Emplacement and rheomorphic deformation of a large, lava-like rhyolitic ignimbrite: Grey's Landing, southern Idaho. Geological Society of America Bulleitn. 123(3-4): 725-743.

Bailey, R.A., 1989. Geologic map of Long Valley caldera, Mono-Inyo Craters Volcanic Chain, and Vicinity, Eastern California. US Geol. Survey Map I-1933.

Bailey, R.A., 2004. Eruptive history and chemical evolution of the precaldera and postcaldera basalt-dacite sequences, Long Valley, California; implications for magma sources, current seismic unrest, and future volcanism: U.S. Geological Survey Professional Paper 1692, 75 p. [http://pubs.usgs.gov/pp/pp1692/].

Bindeman, I. N. and Valley, J.W., 2002. Oxygen isotope study of the Long Valley magma system, California; isotope thermometry and convection in large silicic magma bodies. Contributions to Mineralogy and Petrology 144(2): 185-205.

Bursik, M., 2009. A general model for tectonic control of magmatism: Examples from Long Valley Caldera (USA) and El Chichon (México). Geofisica Internacional 48(1): 171-183.

Bursik, M., Renshaw, C., McCalpin, J. and Berry, M., 2003. A Volcanotectonic cascade: Activation of range front faulting and eruptions by dike intrusion, Mono Basin-Long Valley Caldera, California. Journal of Geophysical Research 108(B8): 2393.

Castro, J.M., Dingwell, D.B., Nichols, A.R.L.and Gardner, J.E., 2005. New insights on the origin of flow bands in obsidian, *in* Manga, M. and Ventura, G., eds., Kinematics and dynamics of lava flows Geological Society of America Special Paper 396, p. 55-65.

Castro, J., Manga, M. and Cashman, K., 2002. Dynamics of obsidian flows inferred from microstructures: insights from microlite preferred orientations. Earth and Planetary Science Letters 199(1-2): 211-226.

Denis, D., 2011. Spherulite growth in high silica volcanic rocks. B.Sc (Honours) thesis; University of Ottawa, 70 pp.

Dingwell, D. B., Hess, K.-U. and Romano, C., 1998. Viscosity data for hydrous peraluminous granitic melts; comparison with a metaluminous model. American Mineralogist 83(3-4): 236-239.

Dingwell, D.B. and Webb, S.L., 1989. Structural relaxation in silicate melts and non-newtonian melt rheology in geologic processes. Physics and Chemistry of Minerals. 16: 508-516.

Dingwell, D.B. and Webb, S.L., 1990. Relaxation in silicate melts. European Journal of Mineralogy 2: 427-449

Eichelberger, J C., Lysne, P.C., Miller, C.D. and Younker, L.W. (1985). Research drilling at inyo domes, California: 1984 results. Eos. 66: 186-187.

Eichelberger, J.C., Carrigan, C.R., Westrich, H.R. and Price, R. H.,1986. Non-explosive silicic volcanism. Nature 323(6089): 598-602.

Eichelberger, J.C., 1989. Are extrusive rhyolites produced from permeable foam eruptions? Bulletin of Volcanology. 51: 72-75.

Fink, J. H., 1985. Geometry of Silicic Dikes Beneath the Inyo Domes, California. Journal of Geophysical Research 90(B13): 11127-11133.

Fink, J. H., and Manley, C.R.,1987. Origin of pumice and glassy textures in rhyolite flows and domes *in* Fink, J.H., ed., The emplacement of silicic domes and lava flows: Geological Society of America Special Paper 212: 77-88.

Fink, J. H., Anderson, S. W. and Manly, C.R., 1992. Textural constraints on effusive, silicic volcanism: beyond the permiable foam model. J. Geophys. Res. 97(B6): 9073-9083.

Friedman, I., 1989. Are extrusive rhyolites produced from permeable foam eruptions? Bulletin of Volcanology. 51: 69-71.

Gonnermann, H. M. and Manga, M., 2005. Flow banding in obsidian: A record of evolving textural heterogeneity during magma deformation. Earth and Planetary Science Letters 236(1-2): 135-147.

Gottsmann, J., Giordano, D. and Dingwell, D.B., 2002. Predicting shear viscosity during volcanic processes at the glass transition: a calorimetric calibration. Earth and Planetary Science Letters. 198: 417-427

Halliday, A.N., Mahood, G.A., Holden, P., Metz, J.M.,Dempster, T.J. amd Davidson, J.P.,1989. Evidence for long residence times of rhyolitic magma in the Long Valley magmatic system: the isotopic record in precaldera lavas of Glass Mountain. Earth and Planetary Science Letters 94(3-4): 274-290.

Hess, K.-U. and Dingwell, D.B.,1996. Viscosities of hydrous leucogranitic melts: An non-Arrhenian model. American Mineralogist 81(9-10): 1297-1300.

Hess, K.-U., Dingwell, D.B. and Webb, S.L., 1995. The influence of excess alkalis on the viscosity of a haplogranitic melt. American Mineralogist 80(3-4): 297-304.

Hiltreth, W. and Mahood, G.A., 1986. Ring-fracture eruption of the Bishop Tuff. Geological Society of America Bulletin 97(4): 396-403.

Hildreth, W., 2004. Volcanological perspectives on Long Valley, Mammoth Mountain, and Mono Craters: several contiguous but discrete systems. Journal of Volcanology and Geothermal Research 136: 169-198.

Iezzi, G. and Ventura, G., 2005. The kinematics of lava flows inferred from the structural analysis of enclaves: A review, *in* Manga, M. and Ventura, G., eds., Kinematics and dynamics of lava flows: Geological Society of America Special Paper 396, p. 15-28.

LeBas, M.J., LeMaitre, R.W., Streckeisen, A. and Zanettin, B., 1986. A chemical classification of volcanic rocks based on the Total Alkali-Silica Diagram. Journal of Petrology 27(3) 745-750.

Lofgren, G., 1971a. Spherulitic textures in glassy and crystalline rocks. Journal of Geophysical Research 76(23): 5635-5648.

Lofgren, G., 1971b. Experimentally produced devitrification textures in natural rhyolitic glass. Geological Society of America Bulletin 82: 111-124.

Manga, M., 2005. Deformation of flow bands by bubbles and crystals, *in* Manga, M. and Ventura, G., eds., Kinematics and dynamics of lava flows. Geological Society of America Special Paper 396: 47-53.

Mankinen, E., Grommé, C., Dalrymple, G., Lanphere, M. and Bailey, R, 1986. Paleomagnetism and K-Ar Ages of Volcanic Rocks From Long Valley Caldera, California. Journal of Geophysical Research. 91(B1), 633-652.

McPhie, J., Doyle, M. and Allen, R., 1993. Volcanic Textures: A guide to the interpretation of textures in volcanic rocks. Hobart, CODES Key Centre, University of Tasmania, 196p.

Miller, C.D., 1985. Holocene eruptions at the Inyo volcanic chain, California: Implications for possible eruptions in Long Valley Caldera. Geology, 13: 14-17

Mysen, B.O.,1983, The Structure of Silicate Melts. Annual Review of Earth and Planetary Science. 11(1): 75-97.

Mysen, B.O., Virgo, D., Harrison, W.J., Scarfe, C.M., 1980. Solubility mechanisms of H_2O in silicate melts at high pressures and temperatures: a Raman spectroscopic study. American Mineralogist., 65: 900-914.

Perugini, D., Ventura, G., Petrelli, M. and Poli, G., 2004. Kinematic significance of morphological structures generated by mixing of magmas: a case study from Salina Island (southern Italy). Earth and Planetary Science Letters 222(3-4): 1051-1066.

Pollard, D.D., Segal, P. and Delaney, P.T., 1982. Formation and interpretation of dilatant echelon cracks. Geological Society of America Bulletin 93: 1291-1303.

Proulx, N., 2008. Development of textural and chemical heterogeneities in high-silica rhyolites, Mono-Inyo chain, eastern California. B.Sc (Honours) thesis; Univarsity of Ottawa, 67 pp.

Rust, A. and Cashman, K.V., 2007. Multiple origins of obsidian pyroclasts and implications for changes in the dynamics of the 1300 B.P. eruption of Newberry Volcano, USA. Bulletin of Volcanology 69(8): 825-845.

Sackett, P.C., McConnell, V.S., Roach, A.L., Priest, S.S. and Sass, J.H., 1999. Long Valley Coring Project, 1998-Preliminary Stratigraphy and images of recovered core. U.S. Geological Survey Open File Report OF 99-158.

Sampson, D.E., 1987. Textural heterogeneities and vent area structures in the 600-year-old lavas of the Inyo volcanic chain, eastern California, *in* Fink, J.H., ed., The emplacement of silicic domes and lava flows: Geological Society of America Special Paper 212: 89-101.

Seaman, S.J., Scherer, E.E. and Standish, J.J.,1995. Multistage magma mingling and the origin of flow banding in the Aliso lava dome, Tumacacori Mountains, southern Arizona. Journal of Geophysical Research. 100(B5): 8381-8398.

Shand, S.J., 1927. The Eruptive Rocks. John Wiley. New York.

Smith, J.V., 2002. Structural analysis of flow-related textures in lavas. Earth-Science Reviews 57(3-4): 279-297.

Stevenson, R.J., Dingwell, D.B., Webb, S.L., and Bagdassarov, N.S., 1995. The equivalence of enthalpy and shear stress relaxation in rhyolitic obsidians and quantification of the liquid-glass transition in volcanic processes. Journal of Volcanology and Geothermal Research. 68: 297-306.

Swanson, S. E., Naney, M.T., Westrich, H.R. and Eichelberger, J.C.,1989. Crystallization history of Obsidian Dome, Inyo Domes, California. Bulletin of Volcanology 51(3): 161-176.

Taylor, B. E., Eichelberger, J.C. and Westrich, H. R., 1983. Hydrogen isotopic evidence of rhyolitic magma degassing during shallow intrusion and eruption. Nature 306(5943): 541-545.

Tuffen, H. and Dingwell, D., 2005. Fault textures in volcanic conduits: evidence for seismic trigger mechanisms during silicic eruptions. Bulletin of Volcanology 67: 370-387.

U.S. Geological Survey and California Geological Survey, 2006. Quaternary fault and fold database for the United States, accessed Nov 11, 2010, from USGS web site: http//earthquake.usgs.gov/regional/qfaults/.

Vogel, T.A., Eichelberger, J.C., Younker, L.W., Schuraytz, B.C., Horkowitz, J.P., Stockman, H.W. and Westritch, H.R., 1989. Petrology and emplacement dynamics if intrusive and extrusive rhyolites of Obsidian Dome, Inyo Craters volcanic chain, eastern California. Journal of Geophysical Research. 94(B12): 17,937-17,956.

Wallace P., and Anderson, A.J., 2000. Volatiles in magmas. *In*: Sigurdsson H. et al. (eds) The Encyclopedia of Volcanoes. Academic Press, London, 149-170

Wilson, C.J.N. and Hildreth, W., 1997. The Bishop Tuff: New Insights from Eruptive Stratigraphy. The Journal of Geology 105(4): 407-439.

Winter, J.D., 2001. An Introduction to Igneous and Metamorphic Petrology, Prentice Hall, New Jersey.

Appendicies

List of Appendicies

Appendix I: Field Notes

Date	Loc. ID	UTM mE	UTM mN	Accuracy	Description
15 July					Reconniasance tour of OD: OD contains three facies (1) Dense, black obsidan, DBO; (2) black-dk grey pumice, BGP; and (3) Tan-lght orange rhyolite, TLOR.
					TLOR far exceeds DBO in vol. lineations of zones of re-melted BDP
16 July	10-OD-01	322911	4180733	9	Finely Laminated BGP "filling in" Frax in massive BGP.
	10-OD-02	322635	4181799		NE side of dome ~100 m away on N.Side of "Dry ravine" collected (1) representative sample of airfall tuff & phreatic(?), and (2) large-clast bias of exceptional quality
	10-OD-03	322418	4181716		Boundary of NE-side of OD in pit ~4 m wide.
			GV		On NE-Side, a few 2-4 m wide, 0.5 - 2 m deep conical pits (small explosion pit?)
17-July	10-OD-04	322888	4180654	11	Sitting on stump bearing 230degrees to section on E. Side of dome (~75 m away) Next control point will be a "strat" section. OBS: variably-dipping (~10-50deg at distance). Alternating bands of orange-breccia 35-40%, and DBO (~60-65%)
	10-OD-05	322841	4180616	9	Dipping suite of DBO, BGP, TLOR and Orange breccia. "strat" section measured (see "strat column" tab). Sample taken OD-05 to show banding.
	10-OD-06	322679	4181370	8	S. Side of ravine on NE side of OD. Several Pyroclastic bombs strewn over xxx m2 with small, m-sized impact pits. Some show radial-jointing frax indicative of transport when hot. Blocks mostly TLOR (origin deeper in Dike?). A few DBOs also were ejected. Sample OD-06 taken to show rhyolite texture and example of pyroclastic/phreatic ejecta
					Photos: Ruler stick/green pen showin location of Section OD-05. Photos showing Phretic Field and OD margins above said field
			GV		Orange breccia on E-side of dome can be traced several tens of meters and in places are folded intensely

19 July	10-OD-07	322809	4180530	10	Section completed on E. Side of OD ~2 m left of chaotcally flow-banded med-grey rhyolite. 2-5% phenos dominatly plag, but with sparse hbl phenos. Attitude 190/45. On right side of 2-3 m rhyolite inclusion exist a double-generational anticlinal fold (see drawing in book). Less oxidation/brecciation on limb than on synclinal fold to the right of anticline
			GV		Samples taken from OD-7: 7A: Typical DBO; 7B: Alternate banding of DBO and GBP; 7C interplay between DBO and breccia; 7D: Orange breccia; 7E: DBO w/ med-grey inclusion; 7F: Dk brown-grey obsid specimen
	10-OD-08	321471	4181235	15	West side of OD: 8-10 m tall cliff by OD pkng lot. Attitude: 40/15. Dominantly black obsidian. Significantly less flow-banding comapred to the E. side of OD. Some planar mm-cm-sized flowbanding. 2-5% phenos. Orange domain is not brecciated, appearing gneissic. "augens" of cm-dm-sized pumecious and micro-vesicualr rhyolite. If Eich is correct in that OD originated as a permeable foam, then the augens are fiamme. Oxidized shear-zone w/ evidence of both ductile and brittle deformation. 2-generational folds are present. Slickensurfaces are oxydized but some are lightly oxidized. Sparse <1 cm-sized spherulites.
			GV		Photos taken at OD-08 show relationships between different domains. FDR showing pumice DBO, Thomas Jefferson showing micro-vesicular rhyolite. Ruler-stck showing location of section OD-08. Green pen showin MVR "fiamme"

20-July	10-OD-09	321598	4181409	7	On W.-side of OD ~100 m N of Point OD-08. Obs: Sub-vertical dip on apparent outcrop(likely not in-situ). Intensely folded/boudenaged ductile sheared domains of med.-gray rhyolite which dominate the inclusion-phase. Domains of pumice are also intensely folded but are in the distinct minority of clasts. There is a well-defined contact between gray-rhyolite and dark-brown pumice. 2-5% phenos on obsidian. Aproximatly-equant rhyolite domains 50-75 cm large.

				GV	~halfway down-talus-slope of 10-OD-09, large (~2 m) block displaying interplay between ductile and brittle deformation with the ductile deformation that, in part, has been folded which resemble "taffy." One spot on block shows ductile deformation folding out in the shape of a "clip" Interp: Rock fractured when above stiffening pont and relaxed which produced flow features RESEMBLNG pahoehoe texture, though here it lkely oozed out of the inter-layers. [Flow:flow-banding --> Fracture: pink oxidation --> Flow: from interlayers --> Fracture: en echelon fracture.] Collected OD-09A to show what appears to be every phase and behaviour of OD in a hand-sample
	10-OD-10	322759	4180475	11	Double-composite strat section taken E. Side of OD ~100 m S. of section OD-08. Attitude 255/25. Photos taken of section.
	10-OD-11	322676	4181363	5	Revisiting phretic field on NE sidde of OD to take photos of phretic ejecta-impact pits. A. Fowler paced of the size of field and extends 200 m away from base of dome, and 450 m alongside dome. If we approximate the area as a rectangle, we have 90,000 m2

21-July	10-OD-12	321775	4181672	7	NW side of OD at bottom of talus slope. Observ: Blocs of flow-banded obsidian w/ varying amts of pumicious bands. Distinguishing feature is the relative copious amnts of spherulits up to 20 cm in diameter. A couple of oblate-spheroid-shaped spherultes w/ semimajor axis about 20 cm. Colour is black for obsidian and dk-grey-brown for the pumice. Dominatly planar flow-bandng with a few tightly-folded domains. 2-5% mm-sized phenos. **27 July addendum: i**n talus block: highly flattened spherulite-train in en-echelon formation in DBO between 2 pumice bands. Photos are in 2010-07-27 after peace sign

	10-OD-13	321808	4181655	10	Outcrop up-talus-slope from OD-12. A ~10 m high cliff with the bottom half displaying planar to chaotically flow-banded black obsidian and dk-med-grey-brown pumecious bands with 10-30% <2 cm sized spherulites both dispersed and in "trains." Spherulites only appear to exist in the obsidian to transitional phases. Spherulite shapes range from sphericle to oblat-spheroid with the direction of flattening perpendicualr to flow banding. Spherulites display varying degrees of "hollowing out." Pheno abunance ~2-3%. Sparse apparent well-defined equant med-gray rhyolite in this outcrop. Top half of outcrop is predominatly dense black obsidian w/ minor bands of dk gray-brown pumice--in proportions much less than in the bottom half. Spherulites appear to be absent. Phenos content is significantly higher (perhaps ~10% based on a few blocks on the talus slope which presumably shed from the upper part of outcrop.
				Int	RE: OD13: Bottom part of outcrop where spherulites are abundant, mm-sized phenos are significantly less abundant (2-3%) than the top part of the outcrop, where phenos are much more abundant Perhaps ~10-15%. This is not a perfect relationship though. HYPOTHESIS: If spherulites form above the glass-transition, we can expect not to find sperulites in highly-pumiceous domains.
				Photos	RE: OD13: FDR photo of various habits of spherulites/lithophysae. T-Rex showing trains of spherulites: Picture of spherulite-absent, pheno-rich rock(which we took for as sample) against spherulite-rich, pheno-poor outcrop. GW showing spherulite expansion within transitional pumice unit.
				Samples	RE: OD13 13A: Transitional, whole spherulite; 13B: pumice; 13C: disaggregated spherulite + glass+ pummice; 13D: 10-15% phenos sans spherultes (A fowler pic 164-166); 13E: Spherulites in glass between two transitional domans; 13F: Transtional pumice w/ spherulites

26-July	10-OD-14	321984	4180164	9	On top of S. Side of dome at place LVO labels the "squeeze-up structure" Dk-brown-grey to rarely black pumice. Cm-dm-sized flow-banding of highly vesicular to somewhat denser (less vesicular) transitional domain. Dips range from sub-vertical to sub-horizontal. Flow banding planar to locally intensly folded with cm-dm-lambda and dm-sized amplitude within a larger fabric of large(10s of meter lambda-scale folds. 2-5% mm-sized phenos. Sparse domains of orange-brecciated unit, which takes up 30-40% of surface area of one horizon (the remainder being dk-grey/brown pumice). Wood stake on high-point is 1.3 m from base, 90 cm from the bottom of exposed part
	10-OD-15	321934	4180384	20	Crease-structure trending N-S. GPS taken in centre. 20-30 m long, 2 m at the base, ~10 m at the top. Planar to broadly-folded cm-mm-sized flow-banding of pumice which is principally dk.-gray to brown in colour. cm-sized bands of slightly more massive (less bubble-density). Sparse 2-3% mm-sized phenos. Broad-scale (m-sized folding on one surface of crease is largely mirrored on other side, suggesting a common "genetic flow-regime prior to splitting.
				GV	In a broad sense for OD-15, elongation of vesicles appear to be within 10 degrees of being perpendicular to the surface of the crease. Lack of orange-brecciated domains coupled with flow-banding and the broad-scale concave-outward bending/folding of the crease structure suggests that deformation was largely ductile and above the glass transition for the stress being applied
				Samples	15A, 15B taken to show relationship between the smooth surface of the crease and bubble orientation. Arrow showing original, up-orientation and Sfc=crease surface.

27 July	10-OD-16	321859	4180965	16	On W. Side above probable vent area (marked by summit). Obs: Med-grey massive micro-vesicular rhyolite w/ sub-vertical, largely planar, mm-sized flow banding which appears to deflect in m-sized open folds around stretched (~1m smaj axis, ~50 cm smin axis) inclusions of med-grey-tan rhyolite. Non-oxidized, med.-dk grey corrugated deformational surface which n places fracture indicating breakage below glass transition which in one place formed highly-jumbled brecciated domains. mm-sized phenos abundance 2-3% accross all visable phases. INCLUSIONS: 2-3 elongated light-med-grey tan variably flow-banded rhyolite. Outcrop weathers to orane along some fractures
				Samples	16A: showing pummiceous transition; 16B: showing mm-sized flow-banding surrounding inclusion; 16C: showing relationship between med-gray to tan rhyolite inclusion and surrounding flow-banded regime.

28-July	10-OD-17	321797	4180145	6	FpBs (mod. from Higins, 2009): About 15-20 m W. of top of S. ramp. Collecting Rocks for FpBs on outcrop of rhyolite. Obs: White-off-white weakly flow-banded rhyolite which weathers to tan, lgt orange. 2-3% mm-size phenos of hbl+rare bi in an apparent crystallne matrix of feldspar and quartz.
	10-OD-18	321969	4180359	7	FpA (from Higgins, 2009): E. side of road opposite the crease-structure (~25-30 m from main trail) in outcrop. Obs: 1-2% mm-sized mafic phenos set in mm-cm-sized flowbanded groundmass of med-grey to off-white. mm-sized fsp phenos not readly discernable by eye.
	10-OD-19	321702	4180856	7	FpBn (mod from Higgins, 2009): N. Sde of path between top of W. ramp and the "black patch" Obs: dark-lght grey mm-cm-sized flow-banding of microvesicular rhyolite. 2-5% mm-sized fsp phenos. 1-2% mm-szed mafic phenos Direct sunlight imparts a shiny luster, which, on smooth surfaces look "phyllitc"
	10-OD-20	321798	4181009	5	FpCn (mod from Hggins, 2009): About 20 m NE from NE loop of "black patch." Obs: Largely Planar mm-cm-scale flowbanding of dark brown-burnt red bands in light-med grey micro-vesicular rhyolite which weathers to tan to lht orange. Direct sunlight imparts a variably "phylitic" and shiny luster. 2-3% mm-sized fsp phenos, some phenos are up to 0.5 mm large. 1-3 % mm-sized hbl (lath shaped)+bi

Appendix II: Electron Microprobe Standards

Silicate standards used in acquiring chemical data by the electron microprobe are listed below, (Jones, P. writt. commun.):

Element	**Line**	**Mineral Standard**
Si	Ka	Olivine
Al	Ka	Spinel syn.
Mg	Ka	Olivine
Na	Ka	Jadeite
K	Ka	Microcline (USNM)
Ca	Ka	Wollastonite
Ti	Ka	$MnTiO_3$ syn.
Cr	Ka	Cr_2O_3 syn
Mn	Ka	$MnTiO_3$ syn.
Fe	Ka	Fayalite syn.
Ni	Ka	NiO syn.
Ba	La	Barite
Cl	Ka	Tugtupite
S	Ka	Barite
P	Ka	$NaBePO_4$
F	Ka	Lithium fluoride syn.

Appendix III: Electron Microprobe Data for Glasses

Table A: Glass transect data for thin section 10-OD-1A

Point#	1	2	3	4	5	6	7	8	9	10	11	12	13
Species													
SiO2	74.22	75.17	74.63	75.15	75.34	75.79	75.82	75.57	75.86	75.56	75.49	74.52	75.70
Na2O	3.85	3.57	3.49	3.48	3.58	3.66	3.79	3.63	3.46	3.56	3.71	3.76	3.73
CaO	0.49	0.48	0.48	0.64	0.44	0.56	0.53	0.48	0.48	0.47	0.56	0.52	0.56
K2O	5.85	5.67	5.76	5.60	5.71	5.66	5.55	5.60	5.70	5.67	5.59	5.47	5.58
FeO	0.82	1.06	0.75	1.46	0.80	0.84	1.00	0.81	0.82	0.67	0.90	0.82	0.95
Al2O3	13.63	13.63	13.70	13.52	13.56	13.67	13.71	13.63	13.50	13.53	13.58	13.67	13.49
Cl	0.02	0.05	0.04	0.02	0.02	0.02	0.04	0.01	0.04	0.01	0.03	0.03	0.01
P2O5	0.06	0.05	0.03	0.07	0.08	0.04	0.07	0.04	0.04	0.02	0.04	0.05	0.05
MnO	0.05	0.02	0.06	0.08	0.03	0.08	0.09	0.06	0.03	0.05	0.08	0.05	0.06
BaO	0.03				0.03	0.02	0.01					0.03	
SO3	0.03	0.01	0.02	0.02	0.03	0.01	0.02		0.03				0.01
MgO	0.01	0.02	0.01	0.07	0.00	0.03	0.02	0.03	0.02	0.01	0.03	0.02	0.05
TiO2	0.15	0.11	0.12	0.10	0.08	0.13	0.10	0.16	0.11	0.11	0.14	0.10	0.11
Total	**99.21**	**99.84**	**99.08**	**100.20**	**99.72**	**100.51**	**100.74**	**100.01**	**100.10**	**99.67**	**100.14**	**99.05**	**100.31**

Table continues below

Point#	14	15	16	17	18	19	20	21
Species								
SiO2	75.49	75.50	74.93	75.92	75.77	74.96	75.94	74.40
Na2O	3.54	3.61	3.70	3.69	3.72	3.64	3.56	5.81
CaO	0.49	0.49	0.54	0.44	0.48	0.47	0.41	0.58
K2O	5.74	5.83	5.71	5.76	5.70	5.62	5.74	3.18
FeO	0.73	0.87	0.87	0.87	0.85	0.79	0.81	0.48
Al2O3	13.57	13.56	13.48	13.73	13.60	13.58	13.61	13.74
Cl	0.01	0.04	0.02	0.04	0.04	0.03	0.02	0.02
P2O5	0.04	0.06	0.05	0.04	0.03	0.06	0.04	0.01
MnO	0.05	0.05	0.06	0.09	0.08	0.06	0.07	0.05
BaO						0.01	0.02	0.02
SO3	0.01		0.01		0.03			
MgO	0.02	0.01	0.03		0.03	0.01	0.03	0.02
TiO2	0.08	0.12	0.14	0.11	0.13	0.09	0.14	0.02
Total	**99.78**	**100.13**	**99.54**	**100.69**	**100.45**	**99.32**	**100.38**	**98.33**

Table B: Glass transect data for thin section 10-OD-13E

Point# Species	1	2	3	4	5	6	7	8	9	10	11	12	13
SiO2	73.99	75.13	74.97	74.72	75.42	74.78	74.63	74.45	74.03	74.99	67.40	74.14	74.44
Na2O	4.26	4.05	3.92	4.17	4.09	4.29	4.07	4.33	4.20	4.13	5.99	3.99	4.18
CaO	0.46	0.63	0.59	0.59	0.53	0.67	0.52	0.64	0.58	0.55	0.33	0.54	0.56
K2O	5.64	5.32	5.53	5.34	5.29	5.31	5.28	5.09	5.19	5.26	6.67	5.49	5.43
FeO	1.02	1.06	1.04	0.92	0.92	0.91	0.97	1.09	0.85	0.87	0.40	0.96	0.84
Al2O3	13.73	13.20	13.13	13.36	13.13	13.22	13.34	13.50	13.41	13.45	17.30	13.34	13.23
Cl			0.26	0.15	0.01	0.01	0.06	0.01	0.06	0.04	0.02	0.09	0.13
P2O5	0.04			0.01	0.01	0.00	0.01	0.01	0.02				0.04
MnO	0.00	0.02	0.06	0.03	0.01	0.06	0.05	0.07	0.03	0.05	0.02	0.05	0.01
BaO													
SO3	0.01	0.03			0.03					0.01		0.04	0.01
MgO	0.01	0.04	0.05	0.04	0.01	0.02	0.02	0.02	0.02	0.04		0.05	0.01
TiO2	0.22	0.18	0.07	0.16	0.13	0.06	0.11	0.07	0.10	0.08	0.01	0.13	0.08
Total	**99.38**	**99.66**	**99.63**	**99.49**	**99.59**	**99.33**	**99.07**	**99.27**	**98.50**	**99.48**	**98.15**	**98.85**	**98.98**

Table continues below

Point# Species	14	15	16	17	18	19	20	21	22	23	24	25
SiO2	74.62	74.74	74.39	73.96	74.88	74.79	74.39	74.79	73.68	74.88	73.55	74.21
Na2O	4.03	4.14	4.33	4.02	4.10	3.89	4.25	4.04	4.13	4.32	3.87	4.38
CaO	0.49	0.55	0.65	0.45	0.69	0.54	0.48	0.64	0.75	0.58	0.63	0.65
K2O	5.43	5.43	5.29	5.55	5.40	5.47	5.30	5.36	5.22	5.20	5.20	5.04
FeO	0.97	0.94	0.91	1.68	1.15	1.27	0.88	1.21	1.33	0.87	1.31	1.11
Al2O3	13.28	13.44	13.43	13.10	13.19	13.12	13.52	13.24	13.36	13.42	13.07	13.90
Cl	0.01	0.11	0.07	0.08		0.18	0.15	0.03	0.07	0.11	0.05	0.06
P2O5		0.03	0.04			0.02			0.03	0.03		
MnO	0.02	0.04	0.03	0.02	0.01	0.08	0.03	0.04	0.06	0.03	0.05	0.06
BaO												
SO3	0.02					0.01				0.01		0.02
MgO	0.02	0.03	0.04	0.01	0.05	0.04		0.04	0.08	0.03	0.06	0.06
TiO2	0.16	0.06	0.11	0.15	0.12	0.10	0.13	0.10	0.14	0.13	0.14	0.04
Total	**99.07**	**99.51**	**99.32**	**99.02**	**99.57**	**99.53**	**99.13**	**99.49**	**98.90**	**99.64**	**97.91**	**99.53**

Appendix IV: Electron Microprobe Data for Feldspars

Table A: Chemical data and feldspar recalculations for microphenocryst rims

Point#	1M1	1M2	1M3	1M4	1M5	2M1-2	2M1-2	2M2-2	2M3-2	2M4-2	2M5-2
Slide	10-OD-1A	10-OD-1A	10-OD-1A	10-OD-1A	10-OD-1A	10-OD-13E	10-OD-13E	10-OD-13E	10-OD-13E	10-OD-13E	10-OD-13E
Species											
SiO2	65.01	66.96	66.47	65.91	65.53	64.37	65.46	64.95	66.82	65.40	66.11
Na2O	4.58	6.51	6.77	6.53	8.90	5.28	6.03	8.72	6.46	8.75	6.73
CaO	0.61	0.45	0.83	0.99	2.58	0.66	0.45	2.83	0.51	2.72	0.64
K2O	9.06	6.73	6.23	6.56	2.16	7.90	7.24	1.84	6.73	1.88	6.19
FeO	0.21	0.20	0.19	0.24	0.14	0.26	0.29	0.32	0.26	0.20	0.23
Al2O3	19.31	18.80	19.39	19.45	20.97	18.93	18.49	21.17	18.71	21.28	18.93
BaO	1.03	0.43	1.08	0.74							
Total	**99.81**	**100.08**	**100.95**	**100.41**	**100.29**	**97.40**	**97.95**	**99.82**	**99.50**	**100.22**	**98.83**
An	3.09	2.22	4.03	4.79	12.15	3.36	2.25	13.61	2.52	13.07	3.17
Ab	42.1	58.2	59.77	57.33	75.77	48.69	54.59	75.87	57.81	76.18	60.32
Or	54.81	39.59	36.19	37.88	12.08	47.95	43.16	10.51	39.67	10.75	36.51

Table B: Chemical data and feldspar recalculations for microphenocryst cores

Point#	1M1	1M3	1M4	1M5n	1M5s	2M1	2M2	2M4	2M5
Slide	10-OD-1A	10-OD-1A	10-OD-1A	10-OD-1A	10-OD-1A	10-OD-13E	10-OD-13E	10-OD-13E	10-OD-13E
Species									
SiO2	65.36	66.96	66.64	65.96	69.59	66.09	66.04	65.81	66.20
Na2O	4.83	8.39	6.92	6.04	6.81	6.32	5.49	5.73	5.19
CaO	0.42	2.18	0.76	0.77	0.87	0.61	0.59	1.01	0.27
K2O	9.20	2.60	6.11	7.81	5.27	7.14	8.07	7.72	8.89
FeO	0.24	0.28	0.16	0.18	0.29	0.16	0.20	0.11	0.17
Al2O3	18.80	20.02	19.43	19.20	18.11	18.81	19.18	19.39	18.81
BaO	0.51	0.68	1.13	0.70	0.64				
Total	**99.37**	**101.12**	**101.16**	**100.66**	**101.59**	**99.12**	**99.56**	**99.77**	**99.54**
An	2.11	10.66	3.69	3.67	4.47	2.96	2.91	4.91	1.32
Ab	43.47	74.23	60.92	52.05	63.27	55.65	49.35	50.38	46.39
Or	54.42	15.11	35.39	44.28	32.26	41.38	47.74	44.71	52.29

Table C: Chemical data and feldspar recalculations for phenocrysts
The first number in "point#" corresponds to phenocryst ID in figure 39. The second number represents the measurement number within each phenocryst

Point#	P1-1	P1-2	P2-1	P2-2	P3-1	P3-2	P4-1	P4-2
Slide	10-OD-13E	10-OD-13E	10-OD-13E	10-OD-13E	10-OD-13E	10-OD-13E	10-OD-13E	10-OD-13E
Species								
SiO2	62.50	63.51	63.95	62.46	63.22	62.80	63.47	65.20
Na2O	8.25	8.27	8.33	8.34	8.44	8.22	8.38	4.22
CaO	3.96	3.95	3.54	4.12	4.22	4.17	3.95	0.45
K2O	1.53	1.65	1.92	1.62	1.59	1.60	1.72	10.28
FeO	0.17	0.23	0.16	0.13	0.13	0.17	0.15	0.13
Al2O3	22.11	22.03	21.76	22.59	22.64	22.33	22.13	19.08
SiO2	62.50	63.51	63.95	62.46	63.22	62.80	63.47	65.20
BaO								
Total	**98.52**	**99.63**	**99.67**	**99.25**	**100.25**	**99.28**	**99.80**	**99.36**
An	19.13	18.93	16.92	19.51	19.73	19.89	18.67	2.20
Ab	72.07	71.67	72.12	71.38	71.40	70.99	71.67	37.61
Or	8.80	9.39	10.96	9.10	8.87	9.12	9.65	60.19